STRESS CORROSION CRACKING IN A HIGH STRENGTH STEEL

T.M. WONG

UNIVERSITY OF CANTERBURY

CHRISTCHURCH, NEW ZEALAND.

STRESS CORROSION CRACKING IN A HIGH STRENGTH STEEL

A thesis presented for the degree of

Master of Engineering

at the

University of Canterbury,

Christchurch, New Zealand.

by

T.M. WONG

May, 1986

To my wife

Siew Lay

ACKNOWLEDGEMENTS

I wish to express my sincere thanks to Dr. J. M. Cowling for his enthusiasm and providing a good deal of valuable discussions throughout the project. His assistance and encouragement is gratefully acknowledged.

I would also like to thank Professor L. A. Erasmus, Professor E. Ehrensperger, Professor S. Pálffy, Mr. F. W. Fahy, Dr. J. S. Smail and Dr. G. J. Parker for their encouragement.

My sincere thanks also is due to the technical staff of the Department of Mechanical Engineering who have provided assistance during the execution of this project; in particular, thanks are due to Mr. H. J. Bright, Mr. H. K. Anink and the workshop staff directed by Mr. O. Bolt.

The author also wishes to thank the department technicians who helped to assemble the equipment, in particular, Mr. P. D. O'Hagan and Mr. O. Bolt who provided assistance throughout the project, and Mr. M. Flaws for execution of the electron microscopy.

The assistance of Miss J. M. Shelton for her photography and skilful tracing of the diagrams for this project is very much appreciated.

My greatest debt is again to Dr. Cowling and Dr. Smail who, throughout the project, have been asked to do photocopying, mailing, and other miscellaneous tasks —— with great patience.

Finally, this project could not have been successfully completed without the continual encouragement and support from my wife Ong Siew Lay. Together with our family, she showed enduring patience and understanding during my study leave.

ABSTRACT

This thesis falls into four fields of study.

The first is a survey of relevant literature concerning the many theories of stress corrosion cracking and hydrogen embrittlement. This includes descriptions of the mechanisms of stress corrosion cracking (SCC) and outlines electromechanical processes and stress - sorption theory. Four widely accepted mechanisms for environment assisted cracking are also outlined. They are, 1) Embrittlement resulting from accumulated hydrogen at embrittlement sites, 2) Lowering of surface energy by adsorption of hydrogen, 3) Hydrogen interaction with dislocations, and 4) Lowering of the binding energy by interaction of hydrogen.

The literature survey is a significant part of this thesis. The overall objective of the survey is to review a series of current SCC tests on high strength steels. The principal findings from these previous studies are summarized, they provide concrete evidence for the conclusion that SCC of high strength steels is due to hydrogen embrittlement.

The second part of the project deals with the development of a stress corrosion loading clevis suitable for testing compact tension specimens. Three existing constant load rigs were developed, and equipment was designed for the successful operation of the rigs.

Corrosive environment was applied to the standard compact tension specimen using a novel circulation system based on a magnetic plate - stirrer. Corrosive solution (3.5% NaCl) was stirred by the magnetic plate, and the vortex created by the magnetic stirrer was used to create a pumping head.

The third area of work dealt with the testing of compact tension specimens of ULTIMO 200 steel using the developed

apparatus. The experimental procedures used are based on the application of linear elastic fracture mechanics to stress corrosion cracking.

The fourth area of work carried out was to perform slot length calibration experiments on CT specimens by using strain gauges.

The results indicated that the specimens pre-cracked in air with a higher dynamic load gave higher threshold stress intensities (K_{Iscc}) than those pre-cracked in air with a lower dynamic load. An electron microscope study indicated evidence of a largely intergranular fatigue crack having occurred in the specimens pre-cracked with a high dynamic load.

CONTENTS

1. INTRODUCTION AND LITERATURE SURVEY

1.1 Introduction

1.1.1 Scope And Objectives

This thesis starts with a review of linear elastic fracture mechanics. The current understanding of the mechanisms of stress corrosion cracking (SCC) of metals in various environment systems is then discussed, with emphasis placed on hydrogen-induced cracking in high strength steels. The application of this mechanistic knowledge has led to an appreciation of the interrelationships between the mechanisms of stress corrosion and hydrogen embrittlement, and, finally, a logical criterion for assessing environment-sensitive fracture susceptibility.

The term stress corrosion cracking is used to denote fractures occuring under static tensile stress after the passage of some time under constant conditions of loading and relatively low corrodent temperature (e.g., room temperature). The relatively common phenomena of creep and fatigue will be excluded from the discussion although these are, of course, a type of delayed fracture in a broad sense.

In reviewing the current state of mechanistic understanding of stress corrosion cracking in metals in various corrosive environment systems some characteristics of stress corrosion cracking are defined. Three currently favoured theories are briefly described, they are the electrochemical, stress-sorption, and electrochemical-mechanical theories. In addition, the behaviour of various types of alloy and conformity with SCC models are discussed.

Several recent papers have been written on SCC tests of similar materials/environment systems to that studied in the present thesis. The principal findings from these previous studies have been reviewed, the results have led to a quantitative understanding of the overall characteristics of, and mechanisms for, environment assisted cracking. Moreover,

these previous studies have provided more empirical data for the conclusion that SCC of high strength steels is due to hydrogen embrittlement.

The four widely accepted micromechanisms for hydrogen induced cracking are the following:- 1) Embrittlement resulting from accumulated hydrogen at embrittlement sites, 2) Lowering of surface energy by adsorption of hydrogen, 3) Hydrogen interaction with dislocations, and 4) Lowering of the binding energy by interaction of hydrogen. These micromechanisms are briefly outlined. The interrelationships between the hydrogen attack and hydrogen embrittlement are discussed.

One of the objectives of this project was to develop test equipment designed to measure K_{Iscc} in a high strength steel subjected to static loading in corrosive environment. Compact tension (CT) specimens were used,and these were fatigue pre-cracked before testing. The laboratory tests were undertaken to gain more understanding of the nature of the fatigue pre-cracking process and its influence on subsequent stress corrosion cracking behaviour.

1.1.2 Linear Elastic Fracture Mechanics

The measurement procedures were based on linear elastic fracture mechanics (LEFM) and used pre-cracked specimens. The advent of linear elastic fracture mechanics and its application to fracture toughness testing is described. Fracture mechanics was originally developed to cover the rapid fracture of relatively brittle materials. However, in relation to environment-sensitive fracture, it has been proved possible to apply fracture mechanics to sub-critical crack growth processes such as stress corrosion, corrosion fatigue, and hydrogen embrittlement.

Traditionally, application of fracture mechanics to stress corrosion requires the use of specimens containing a

crack of known geometry induced by fatigue. The use of such specimens removes the uncertainties connected with crack initiation and enables the stress state at the crack tip to be accurately specified.

1.1.3 Stress Corrosion Tests

SCC tests were conducted on ULTIMO 200 steel (heat treated to a 0.2% proof stress of 1518 MPa) in 3.5% NaCl solution using compact tension (CT) specimens. The specimens were pre-cracked by fatigue loading prior to stress corrosion testing. The effects of the corrosive environment and stress intensity used for pre-cracking on the stress corrosion properties were investigated. Measurements of the threshold stress intensity for hydrogen-induced fracture, K_{Iscc}, at room temperature were made on statically-load CT specimens.

The results include six values of the threshold stress intensities for stress corrosion cracking (K_{Iscc}) based on 500-h tests of CT specimens. Values of 0.2% proof stress from round tensile specimens were measured and a fracture toughness test was used for estimating the sustained load to be applied to CT specimens in the SCC tests. The calibration of testing rigs involved loading the designed test piece on the three existing stress corrosion testing rigs.

Finally, fracture surfaces were examined mainly by scanning electron microscopy (SEM). Detailed fractographs were made for specimens pre-cracked in a) air with dynamic load, b) in 3.5% NaCl solution with static load, and c) in 3.5% NaCl solution with dynamic load. Also, fractographic features of fracture surfaces from tensile test pieces were examined.

1.1.4 Slot Length Calibration Experiments

The slot length calibration experiments were performed on a 10 mm thick compact tension (CT) specimen of ULTIMO 200 steel. The calibrated strain on the back face [i.e., compressive back face strain (BFS)] of CT specimen provides a simple and reliable method for measuring slot length when load is known or for measuring load when slot length is known. The use of BFS method has good potential for developing into a more sensitive crack monitoring technique and is ideal for sub-critical crack growth study.

1.1.5 Testing Rig Calibration

The testing rig calibration was evaluated using a designed calibration test piece of a low carbon steel En 3. The purpose of calibration is to verify the lever ratio of the testing rig No. 3 through the comparison of the compliance functions (rate of change of displacement with load) with testing rigs Nos 1 and 2 having a defined lever ratio of 10:1.

1.2 A Review Of Linear Elastic Fracture Mechanics (LEFM)

Fracture mechanics has become one of the pre-eminent disciplines applied to assess the safety of engineering structures containing crack-like defects.

The following paragraphs review two important approaches to linear elastic fracture mechanics. The first approach is based on an energy balance argument, and the second is based on the singular nature of the stress distribution near a crack tip.

The stress intensity factor K provides a parameter characterisation of the stress field ahead of a sharp crack and the energy available to propagate the crack.

1.2.1 The Griffith Approach

LEFM has developed from a concept proposed by Griffith in 1920.[1] The well-known Griffith equation was derived by considering an ellipsoidal crack in an elastic material. The criterion for its extension was that the energy required for separating the fracture surfaces was just less than the decrease in elastic energy when the crack propagated. Griffith showed that unstable crack growth under plane stress conditions will occur if:-

$$\frac{d}{da}\left[\frac{-\sigma^2 \cdot \pi \cdot a^2}{E} + 4a\gamma\right] = 0 \qquad 1)$$

Where a is the half-length of a through-thickness crack, σ is the stress for fracture, γ is the surface energy of the crack and E is the Young's Modulus.

In the above equation, the first term in the bracket represents the elastic energy loss in a plate of unit thickness, and the second term represents the energy gain of the plate as a result of the creation of the crack surfaces which have a surface energy of γ per unit area.

Griffith[1] indicated that the strain energy release rate at the point of instability should be:-

$$\frac{\sigma^2 \cdot \pi \cdot a}{E} = 2 \cdot \gamma$$

hence, $\sigma \cdot \sqrt{a} = \left(\frac{2 \cdot E \cdot \gamma}{\pi}\right)^{\frac{1}{2}}$ which leads to the well-known Griffith equation:-

$$\sigma_c = \left(\frac{2 \cdot E \cdot \gamma}{\pi \cdot a_c}\right)^{\frac{1}{2}} \qquad 2)$$

The subscript c denotes the critical values of stress and crack size.

Apparently, the tip root radius does not appear in the above equation, and the crack length (2a) emerges as a parameter of prime importance. However, the above equation defines the conditions for the spontaneous propagation of an elastic crack in a completely brittle solid, one which does not deform plastically at the crack tip.

It is important to note that the above equation would need to be extended before it could be applied to polycrystalline or ductile materials. Indeed, in polycrystalline materials, fracture can propagate along either cleavage planes or along grain boundaries, and this gives some resistance to crack propagation by blunting at the crack front and hence relaxing the strength of the stress concentration.

Transgranular cleavage fracture is often observed in pure polycrystalline materials that fail in a brittle manner.

Because the orientation of cleavage planes changes across grain boundaries, the propagation of a crack across such a boundary is difficult. Therefore, a crack in pure polycrystalline materials may spread from one grain to another by nucleating a new crack in an adjoining grain, the two cracks in different grains then join by a tearing action which produces steps in the fracture surface near the grain boundary.

In common polycrystalline materials containing grain boundary segregates, fracture usually proceeds along a grain boundary path instead of along cleavage planes. The branching of intergranular fractures between the grains may result in crack blunting and affect crack growth characteristics.

Although intergranular failure can sometimes be associated with fast fracture it is most commonly a result of environmental attack and/or sustained loads. Fast fracture is most usually transgranular by either ductile shear or cleavage in both pure materials and alloys.

Based on the above considerations, it is therefore important to note that an intergranular or a transgranular crack in a polycrystalline materials does not conform to the geometry required for linear elastic fracture mechanics theory namely a single sharp crack of root diameter smaller than 4b, where b is the lattice parameter.[2] Moreover, when fracture in such materials is preceded by plastic deformation at the crack region, and the crack tip blunts to a semicircular configuration, thereby, the stress concentration effect of the tip of the crack is lessened.

In 1948 (approximately 28 years later), Irwin and Orowan[3, 4,] independently analysed the way in which the work of plastic deformation can be incorporated in the formula for crack propagation. Their results can simply be written in the form:-

$$\sigma = \left[(\gamma + \gamma_p) \cdot \frac{2 \cdot E}{\pi \cdot a} \right]^{\frac{1}{2}} \qquad 3)$$

In the above equation, the work done γ_p in plastic deformation per unit area of crack extension can greatly exceed the true surface energy γ of unit area of separated surface, so that equation (3) can be written[4]:-

$$\sigma = \left[\frac{2 \cdot \gamma_p \cdot E}{\pi \cdot a} \right]^{\frac{1}{2}} \qquad 4)$$

Recent terminology has defined another parameter which can be closely identified with equation (3). The parameter denoted by G is termed the crack extension force per unit length of crack. At the point of instability, G is denoted by G_c, which is called the critical elastic strain energy release rate[5], its value is analogous to the term $2\gamma_p$ in the equation (4).

It is now appropriate to restate the equation (4) in the following form:-

$$\sigma_c = \left[\frac{E \cdot G_c}{\pi \cdot a_c} \right]^{\frac{1}{2}} \qquad 5)$$

Where σ_c is the fracture stress at the point of instability.

For fractures under plane strain condition it would be appropriate to substitute $E/(1 - \nu^2)$ for E[4] in the above equation, where ν is Poisson's ratio, hence equation (5) becomes:-

$$\sigma_c = \left(\frac{E \cdot G_c}{\pi \cdot (1-\nu^2) \cdot a_c} \right)^{\frac{1}{2}} \qquad 6)$$

Since G_c is dependent on the material and the specimen geometry, this parameter can be determined experimentally by measuring the compliance changes of a specimen containing a crack, and this gives G_c for the specimen concerned only.

More specifically, if Hooke's Law with the value of Young's modulus E is assumed to hold up to fracture, the value of G_c for the plane strain condition can be found by rearranging equation (6):-

$$G_c = \frac{\pi \cdot (1-\nu^2)}{E} \cdot (\sigma_c^2 \cdot a_c) \qquad 7)$$

where σ_c and a_c can be determined by measuring the loading force of a standard test piece containing a sharp crack of known length.

1.2.2 Irwin's Stress Intensity Approach

The next major advance in the fracture mechanics approach occurred in 1957. Assuming a crack having a border defined by a simple curve or straight line, and crack extension in the crack plane, Irwin[6] suggested a series of solutions for the linear-elastic theory crack openings associated with various stress conditions. These solutions are based on the mathematical procedures of Westergaard[6].

Irwin has pointed out that the stress field at the tip of a crack is dominated by a singularity of stress which decreases in proportion to the inverse square root of the distance from the crack tip.

In 1958, Irwin[7] suggested three different stress patterns which included load, dimensions and shape factors in the solutions. The three suggested stress patterns (see Fig. 1a) are the opening mode(Mode I) with crack surface displacements normal to the crack plane, the shear mode(Mode II) with crack surface displacements in the crack plane and normal to the crack border, and the parallel or anti-plane(Mode III) with crack surface displacements in the crack plane and parallel to the crack border.

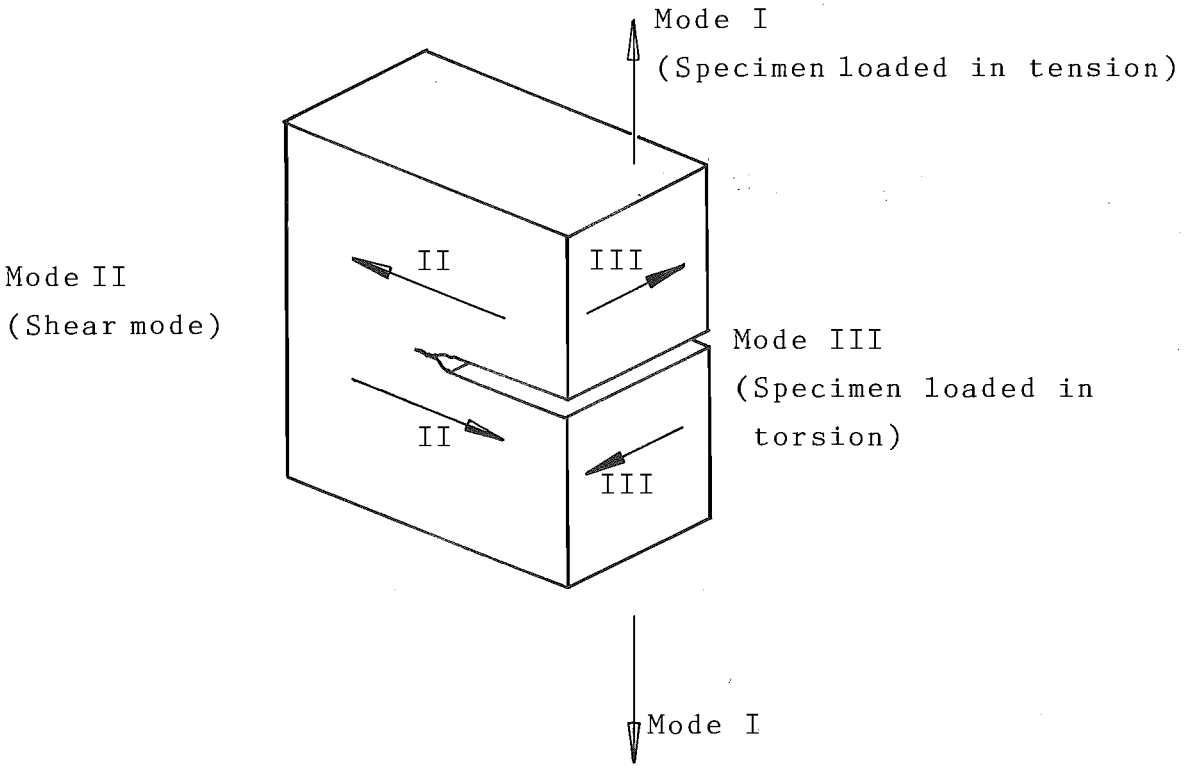

Fig. 1a : The three suggested stress patterns:-
Modes I, II, and III.

To visualize the pattern for the opening mode(Mode I) in a two-dimensional plane sheet, Fig. 1b) illustrates the notation and co-ordinate system for the stress field.

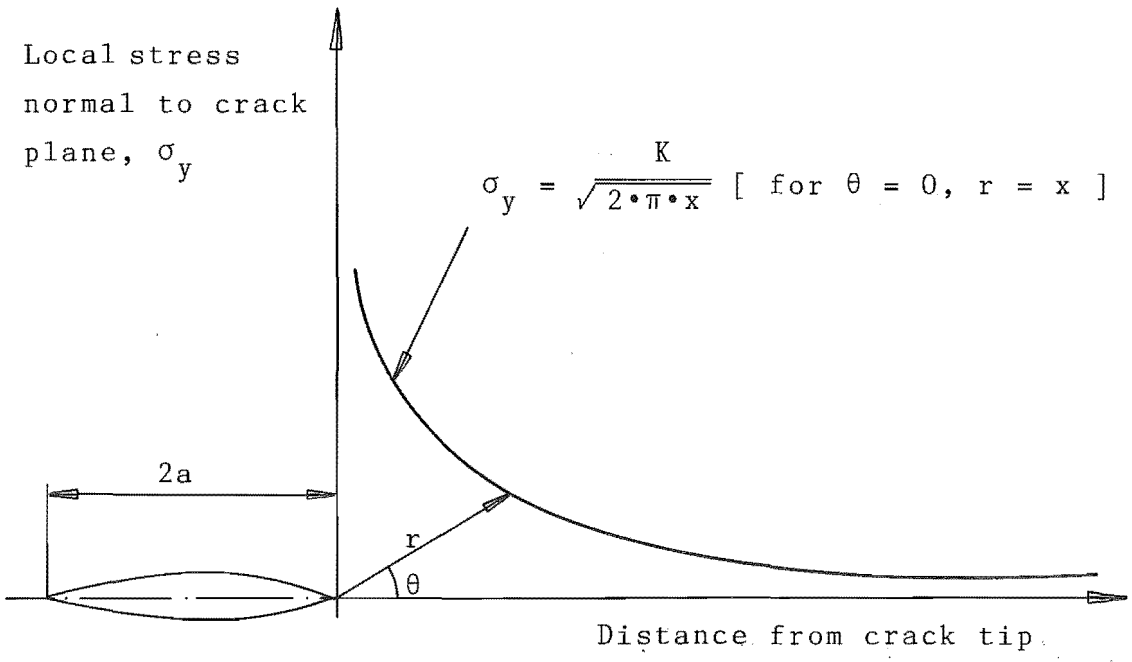

Fig. 1b : Crack plane elastic stress field

The singular stress fields and associated displacements for the opening mode in the plane sheet are shown in equations (8), (9) and (10).

$$\sigma_x = \frac{K}{\sqrt{2\pi r}} \cdot \mathrm{Cos}\frac{\theta}{2} \cdot \left(1 - \mathrm{Sin}\frac{\theta}{2} \cdot \mathrm{Sin}\frac{3\theta}{2}\right) \qquad 8)$$

$$\sigma_y = \frac{K}{\sqrt{2\pi r}} \cdot \mathrm{Cos}\frac{\theta}{2} \cdot \left(1 + \mathrm{Sin}\frac{\theta}{2} \cdot \mathrm{Sin}\frac{3\theta}{2}\right) \qquad 9)$$

$$\tau_{xy} = \frac{K}{\sqrt{2\pi r}} \cdot \mathrm{Sin}\frac{\theta}{2} \cdot \left(\mathrm{Cos}\frac{\theta}{2} \cdot \mathrm{Cos}\frac{3\theta}{2}\right) \qquad 10)$$

Also for plane strain condition

$$\sigma_z = \nu \cdot (\sigma_x + \sigma_y) \qquad 11)$$

The y-direction displacements, v, at the crack plane from which crack opening size would be estimated are given by :-

$$Ev = \frac{2K}{\pi} \cdot (1 - \nu^2) \cdot \sqrt{2\pi r} \qquad 12)$$

Where E is the Young's Modulus, and K is the "stress intensity factor" and may be described as the amplitude or strength of the inverse square root stress singularity at the crack tip. It follows that the stress intensity factors are independent of r and θ.

Since it is generally accepted that the intensity of the stress field determines whether the crack will propagate or not, the 'stress intensity factor' acquires great importance. It is closely related to the Griffith crack theory, in which cracking is controlled by the rate at which the stored strain energy can be supplied to the propagating crack.

According to ASTM standard-E399[8], the stress intensity factor for the tensile mode of crack opening is defined as:

$$K_I = \lim_{r \to 0} \sigma_y \cdot (2\pi r)^{\frac{1}{2}} \qquad 13)$$

Where r equals a distance directly forward from the crack tip to a location where the significant stress is calculated (Fig. 1b). σ_y is the principal stress normal to the crack plane. We should also note that, K_I is the limiting value on y=0 of the product $\sigma_y \cdot (2\pi r)^{\frac{1}{2}}$ as r approaches zero and the subscript I is characteristic of Mode I crack. In addition, for the tensile mode of crack opening (Mode I), we may assume that r/a is very small as r approaches zero.

Looking at a valid stress analysis solution for σ_y, even if it is not expressed in terms of the ratio r/a, the preceding limiting process can be used to obtain the value of K_I[9]. For example, if a small flank angle notch of root radius ρ is subjected to the nominal stress σ_N and the stress concentration factor K_{TH} is available as a function of ρ then:

$$K_I = \lim_{\rho \to 0} (\tfrac{1}{2}) \cdot \sigma_N \cdot K_{TH} \cdot (\pi\rho)^{\frac{1}{2}} \qquad 14)$$

The same basic principles are applied to determining K_I for a laboratory specimen with a crack of controlled size and shape inserted as are used for finding K for a crack in a service component.

In the case of cracks in an infinite plate subjected to an in-plane uniform stress σ_c perpendicular to a crack of length $2a(=2a_c)$, the condition for spontaneous propagation of the crack is given by:-

$$K_c = \sqrt{\pi} \cdot \sigma_c \cdot \sqrt{a_c} \qquad 15)$$

and for the general case:

$$K_c = Y \cdot \sigma_c \cdot \sqrt{a_c} \qquad 16)$$

Where Y is a dimensionless parameter which takes account of different loading systems (tension, bending, etc.) and different crack configuration.

It is important to note that the stress intensity factor (K) has dimensions $MN/m^{3/2}$, and G has units MN/m.

From the dimensional considerations of the above equations it can be seen that the stress intensity must contain the magnitude of the loading forces and must also depend on the crack size. Since the stress intensity dominates the magnitude of the forces acting in the crack tip region it must play an important role in the prediction of the brittle strength of a body containing cracks.

Equation (17) is derived from equation (16) to suit the compact tension (CT) specimen used in this work:

$$K_c = \frac{P \cdot Y(a/W)}{B \cdot W^{\frac{1}{2}}} \qquad 17)$$

Where P is the applied tensile load, and a, B and W are the crack length, specimen thickness and width of the CT specimen. The dimensionless parameter Y(a/W) is detailed later (see section 2.7).

K_c, is intended to define the critical combination of applied stress and crack length required to cause fracture under linear elastic, monotonic loading conditions.[10] K_{IC} is considered to be a material constant, independent of the specimen size, and is called the 'plane-strain stress intensity factor' or the 'plane-strain fracture toughness'.

The plane-strain fracture toughness(K_{IC}) of metallic materials is an important factor, which indicates the crack extension resistance under conditions of crack-tip plane strain. The method for the determination of the value of K_{IC} is detailed as follows:-

The K_{IC} value is calculated from a given principal load by equations that have been established on the basis of elastic stress analysis of specimens of the types described in ASTM standard-E399.[8] The validity of determination of the K_{IC} value depends on the establishment of a sharp-crack condition at the tip of the crack(e.g. a fatigue crack), in a specimen of adequate size. In order for a result to considered valid according to the requirements, it is required that both the specimen thickness, B, and the crack length, a, exceed $2.5 \cdot (K_{IC}/\sigma_{YS})^2$, where σ_{YS} is the 0.2% offset yield strength of the material.

It is noted that the above relationships refer to the crack opening mode, i.e. crack surface displacements normal to the crack plane.

1.2.3 Test Techniques For Fracture Toughness Determinations

The compact tension (CT) specimen is a chevron-notched and fatigue pre-cracked plate loaded in tension. Fig. 35 of chap. 2 shows the configuration of CT specimen for the testing.

In order to find whether the size of the plastic zone is small enough so that the linear elastic stress intensity factor (K) can be applied, it is important to note that, according to ASTM standard, E399[8], both the specimen thickness, B, and the crack length, a, exceed $2.5\cdot(K_{IC}/\sigma_{YS})^2$ where σ_{YS} is the 0.2% offset yield strength of the material.

In order to confirm that the initial selection of a size of specimen produced a valid value of K_{IC}, a carefully controlled laboratory experiment should be made on the CT specimen. In addition to the above test, it is thought that at least two (in order to get a mean value) tensile test specimens shall be tested in tension at room temperature in estimating the value of 0.2% offset yield strength.

For a given material and given laboratory conditions, the effect of specimen thickness on load displacement curves is illustrated in figures 2a - c. It is noted that when a specimen is sufficiently thick that the conditions of strain at the crack tip approach those of idealised plane strain then the test record has the form of Fig. 2a. In this case the load displacement curve shows an abrupt fracture at maximum load (P_{max}). It is thought that the energy increase due to the initial instability exceeded the critical strain energy release rate G_c so that the specimen fractured completely without further increase in load.

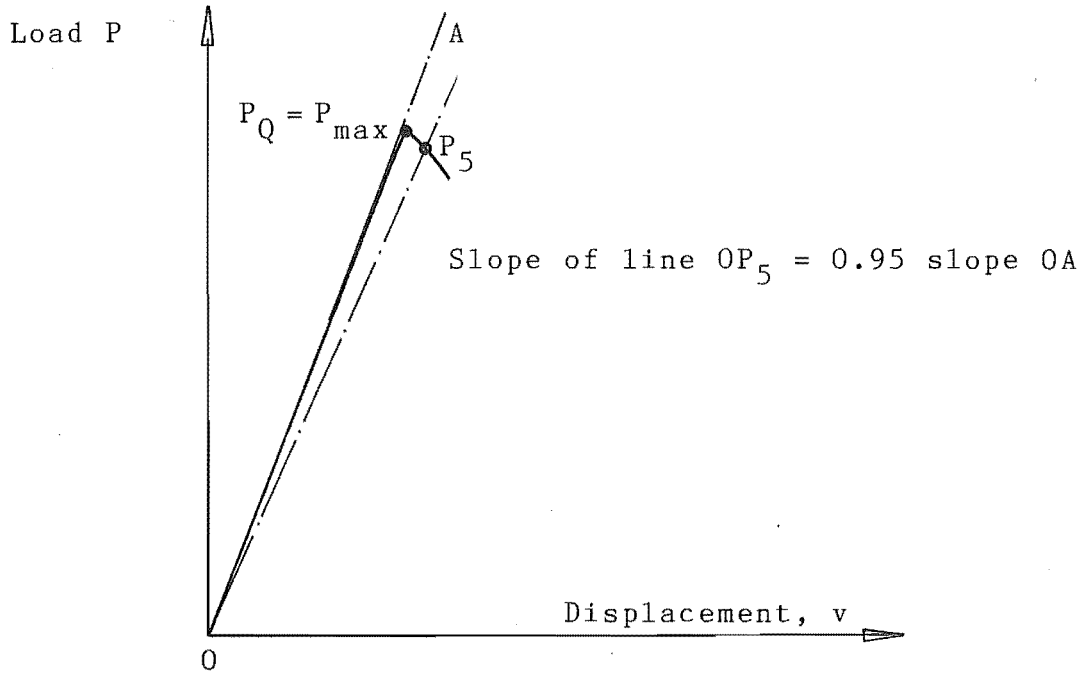

Fig. 2a : A thick specimen

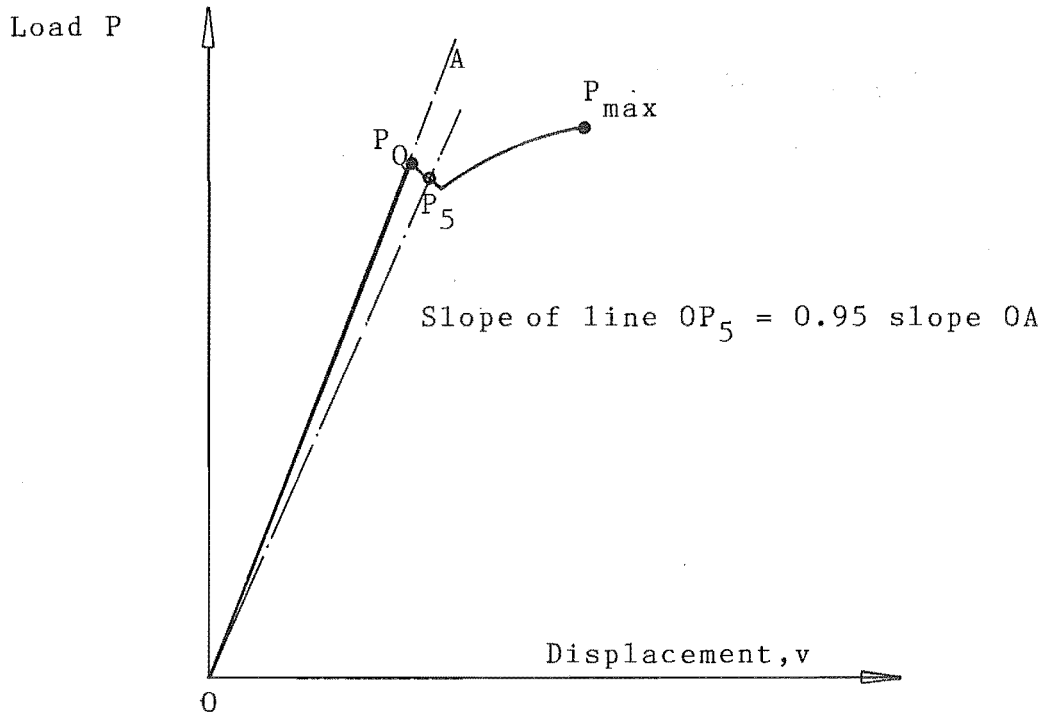

Fig. 2b : A relatively thin specimen.

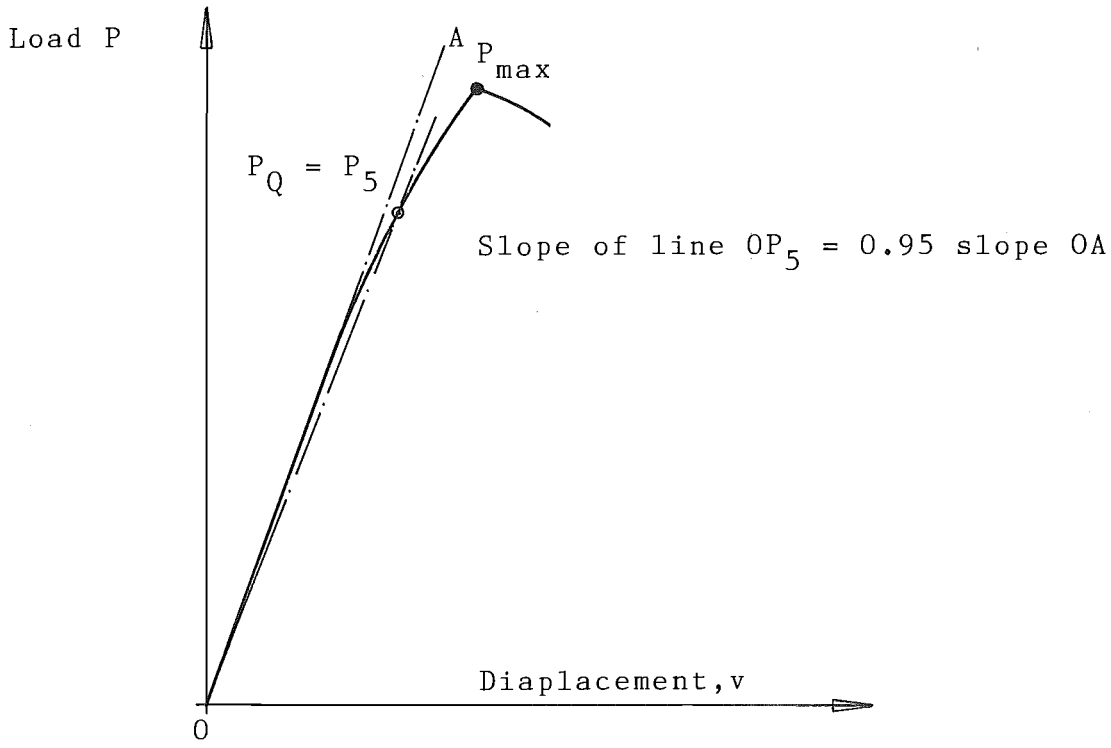

Fig. 2c): A sufficiently thin specimen.

Fig. 2)[8]: Principal types of load-displacement records for compact tension LEFM tests.

For the thinner specimen, the initial instability is arrested (due to relatively thin specimen). The initial burst of crack growth, known as pop-in, originates in the triaxial stress region at mid-thickness. Near the free surfaces, where the triaxial stress state is relaxed the crack growth trails behind that at the mid-thickness. The arrest is dominated by the work required for shear fracture and the test record in this case shows a pop-in step characteristic of meta-instability.

Finally, for a sufficiently thin specimen, the through thickness stress is reduced to zero and the load displacement curve has the characteristics of general plastic deformation, as shown in Fig. 2c.

One of the main features of K_{IC} is that it is independent of specimen thickness, provided the required criteria are met. The currently recommended experimental procedure for determining the value of K_{IC} is now outlined. The fracture toughness (K_{IC}) value for CT specimen can be determined by the following equation (see Sect. 2.9.2):

$$K_{IC} = \frac{P_Q}{B \cdot W^{\frac{1}{2}}} \cdot Y\ (a/W)$$

According to ASTM standard, E399[8], the following details shall be kept in mind when plotting the load displacement record and calculating the value of K_{IC}:

1) Load the specimen at a loading rate such that the rate of increase of stress intensity is within the range from 0.55 to 2.75 $(MN/m^{3/2})/s$.
2) Select a combination of load-sensing transducer and autographic recorder so that the load, P_Q (see Fig. 2a - c) can be determined from the test record with an accuracy of ± 1%.
3) Calculate the ratio P_{max}/P_Q, where P_{max} is the maximum load the specimen was able to sustain. If this ratio does not exceed 1.10, proceed to calculate K_{IC} as described in Sect. 2.9.2; If P_{max}/P_Q does exceed 1.10, then the test is not a valid K_{IC} test. This is due to the fact that the calculated K bears no relation to K_{IC}.
4) As mentioned initially, check the value of $2.5 \cdot (K_{IC}/\sigma_{YS})^2$, if the value is less than both the specimen thickness (B), and the crack length (a), then the test is valid K_{IC} test.

1.3 A Review Of Stress Corrosion Cracking

Stress corrosion cracking is a mechanical-environmental failure process in which sustained stress and chemical attack combine to initiate and propagate cracking in the material.[11] The stresses involved in stress corrosion cracking need not necessarily be applied stresses.[12] They could be residual stresses produced during manufacture of the material concerned.

Failure by stress corrosion cracking is often caused by simultaneous exposure to a relatively mild chemical environment (e.g. 3.5% NaCl solution) and to a tensile stress well below the yield strength of the test specimen.[12] Under such conditions, fine intergranular or transgranular cracks would penetrate the component, leading to eventual break-up.

Corrosion plays an important part in the initiation of cracks. A pit or notch on the surface of the metal may act as a 'stress raiser', and stress corrosion cracks are often observed to start at the base of a pit or at the point of highest stress concentration (e.g. near a notch root) followed by extension of this crack to final rupture.[12]

On the other hand, once a crack has started, the fracture process continues in the stress corrosion crack stepwise manner until the crack length reaches some critical size and the test specimen fails.[13, 14, 15, 16] Using audio-amplification methods, Pardue and co-workers[15] have shown that a mechanical step or jump can take place during crack propagation. In fact, "Pings" were heard without any amplification.

It has been found that stress corrosion cracking data may be correlated by the stress intensity approach. Fig. 3 shows the dependence of the crack propagation rate da/dt on the applied stress intensity, K_I, where t is the time.[9, 17]

we note that the crack growth curve consists of three regions. In region I and III the crack propagation depends strongly on K_I, but in region II the crack propagation rate is virtually independent of K_I.

Regions I and II are most characteristic. Region III is often not observed owing to a fairly abrupt transition from region II to unstable fast fracture.

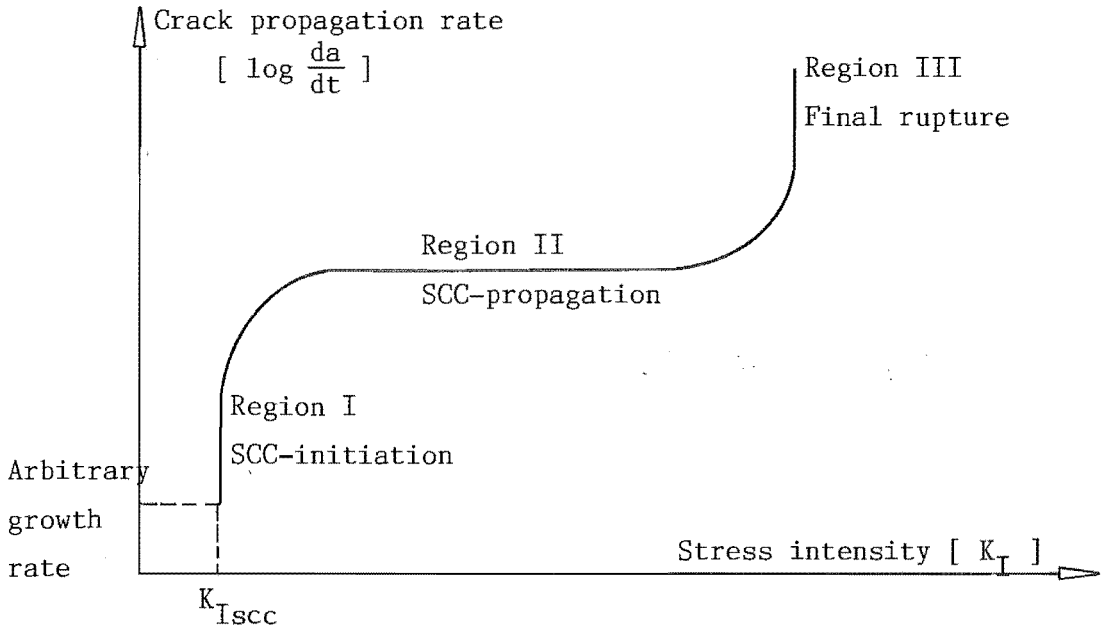

Figure 3: Stress corrosion crack growth rate as a function of K_I

As shown in figure 3 , K_{Iscc} is called the threshold stress intensity[9], below K_{Iscc} a stress corrosion crack does not propagate under sustained load for a given combination of material and corrosive environment.

This threshold stress intensity is an important parameter that can be determined by time-to-failure tests in

which pre-cracked specimens are loaded at various stress intensity levels, thereby failing at different times as shown schematically in Fig. 4[9]

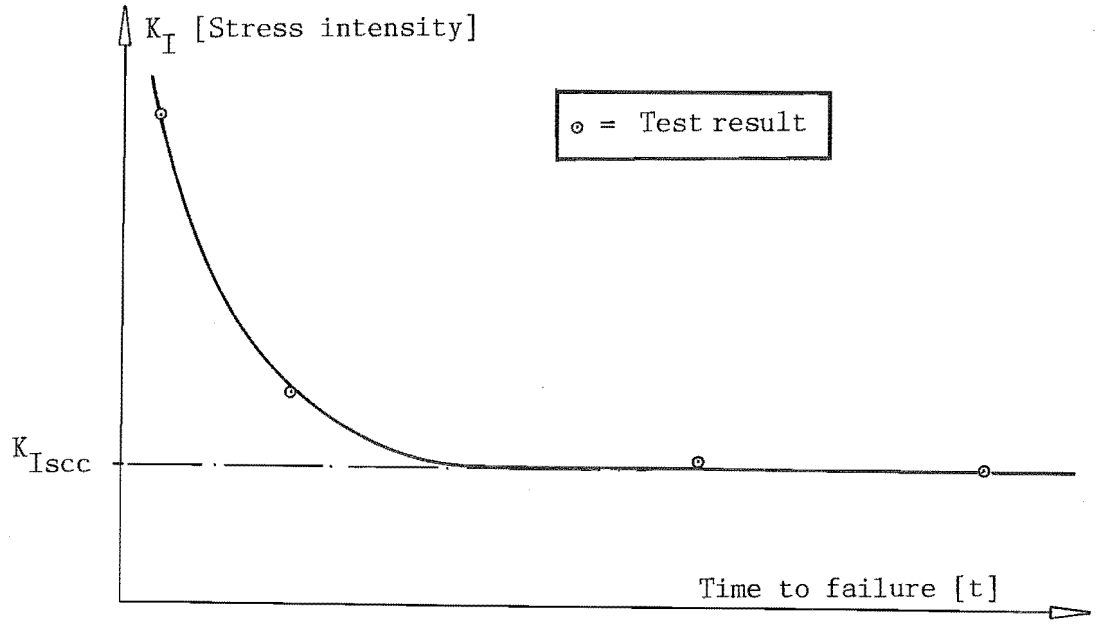

Figure 4: Schematic time-to-failure curve with K_{Iscc}

Basically, when a metal is exposed to a specific corrosive environment, there will be some regions of the microstructure which will be anodic with respect to the rest of the microstructure, and this zone will corrode first.[12, 18] Very often, these regions are the grain boundaries, giving rise to an intergranular crack.

The effect of a tensile stress in accelerating corrosion is primarily to rupture any protective film[12] [For example: This film could be tarnish film (as in the case of brasses) or thin oxide film (as in aluminium alloys)] which might form and hence open up a new anodic zone for further corrosion cracking. However, in many cases, this simple factor is probably complicated by the diffusion rate of the corrodent[13] and precipitation in the grain boundary[19, 20] at the root of the propagating crack.

One of the best known examples of stress corrosion cracking is the season cracking of brass and copper alloys in a moist ammoniacal environment.[12] Failures in copper alloys are particularly interesting because they commonly occur in the absence of any external loads, the effective stress being the residual stress resulting from a cold-working operation. The cracking of brass cartridge cases, which were used in both world wars, were the result of stress corrosion associated with high residual stresses.

To eliminate season cracking, one avoids using cold-formed copper alloys in an ammoniacal environment. In some cases, where copper alloys must, for particular reasons, be used,and where there seems to be any possibility of season cracking, the following manufacturing techniques could be applied to eliminate failures:- (i) the workpiece should be heat treated, to reduce the residual stresses, (ii) the components must be electroplated or painted after the annealing process, to protect from the corrosive environment.

Another example of stress corrosion cracking is caustic embrittlement of boiler steel.[12] In the early years of this century, many rivetted boilers, most of them operating on alkaline well waters (e.g. boilers for steam locomotives), exploded. It is believed that high concentration of alkaline solutions are responsible for producing such failures. It is suggested[12] that the localised concentration of alkaline solution can build up at a mating surface, which is significantly preventing water from circulating whilst permitting evaporation to take place. Such build-up in concentration associated with the working stress due to steam pressure, may induce a localized corrosion path behind washers in bolted components of the boiler.[12] Examination of these failures had also shown cracks or brittle failures at the rivet holes. These areas were cold-worked during riveting operations, and analysis of the whitish deposits found in these areas showed caustic, or sodium hydroxide (alkali additions for controlling the pH-value of the feedwater), to be

the major component. Therefore, brittle fracture in the presence of caustic resulted in the term caustic embrittlement.

Although these two particular types of stress corrosion, season cracking of brasses and caustic embrittlement of plain carbon steel, are now well understood and are unlikely to be a serious problem in future, other types of stress corrosion are not so well understood and are causing increasing concern. Perhaps the most important of these is hydrogen embrittlement. Such stress corrosion failure has been experienced in oil fields.[12] A recent research report of Shewmon[21] indicates that steels (carbon steel and 2.25 Cr-1 Mo steel) exposed to a hot, high-pressure hydrogen at temperatures above 300°C, showed large amounts of methane bubbles were produced on the grain boundaries during stress corrosion. Shewmon adds that the process of bubble growth and link-up is analogous to that by which grain boundary voids link-up to limit the creep ductility of alloys. However, the methods to prevent bubble formation are unclear.

Stress corrosion failures, spectacular and unspectacular, have been reported in many metals - Iron alloys containing 20 and 30% Nickel[22], Aluminium alloys[23], Iron-Silicon single crystal[24], Titanium alloys[25], stainless steels[26] and others, - and in many different situations.[27, 28, 29] In fact, the phenomenon is not even confined to metallic materials - the stress corrosion of glass-fibre polyester[30] is a recent example among nonmetals. Fibre-glass-reinforced polyester plastics are best known to the general public for their use in tanks, pipe or the body of the Corvette automobile. However, polyester plastics show relatively poor resistance to acid or alkali corrosion. Hull and co-workers[30] have tested the material in 0.6 M HCl. The fractographic results show that the fracture surfaces are basically planar, and there is no evidence of individual fibre pull-out, which is characteristic of conventional fracture in non-corrosive environments.

1.3.1 Mechanisms Of Stress Corrosion Cracking

The fundamental processes occurring in stress corrosion have been the subject of a large number of investigations which are summarised in several reviews.[12, 18, 31] It is clear that no single mechanism is involved, the processes varying with the alloy system[29] and corrodent concerned.

In some systems, corrosion aspects are of major importance; in others, the plastic strain and stress are dominant features. Sometimes, failures are intergranular and sometimes transgranular. Different metals in the same corrosive environment can be made to crack in an intergranular or transgranular manner, simply by adding alloying elements to the metal.[29]

During the past 40 years or so, several theories have been advanced to explain in detail the mechanism of stress corrosion cracking.[11] Three major theories are the electrochemical, stress-sorption and electrochemical-mechanical theories. These theories are used to denote premature failure from material/environment combinations of all kinds, ranging from stainless steel in brine to brass in ammonia. It is not surprising, therefore, that several processes are involved. A single mechanism could hardly be expected to account for the entire range of phenomena designated as stress corrosion.

It is recognised that stress corrosion cracking is characterised by the following three factors:

(1) The cracking is affected by heat treatment and compositions of materials.[20, 29]

(2) Cathodic protection reduces stress corrosion cracking.[9]

(3) Pure metals are not susceptible, i.e. there are no galvanic cells set up between adjacent areas in a pure metal due to the homogeneous distribution of pure metal grains.[15, 31, 32]

1.3.2 Electrochemical Theory

Basically speaking, electrochemical processes require the existence of a chemically reactive path or paths in the metal which are anodic to the main volume of the material. The anodic zones are regarded as being distinct from the matrix material, because of the presence of segregates or the precipitated phase, often at grain boundaries. The anodic zones may be either intergranular or transgranular. As pointed out earlier, the path the crack takes depends on the metal and/or corrosive medium, types of dislocation arrays present in the metal, temperature, and on whether the alloy is in the annealed or cold worked condition.

In the case of high strength steels in aqueous solutions, it is well known that electrochemical corrosion can cause hydrogen to be released from the corrodent; the hydrogen can diffuse into the metal, acting as a cathode. Failure under such a cathodic condition is often a result of hydrogen embrittlement.[9, 33] Many researchers propose that such failures should be classed as hydrogen embrittlement, and not as stress corrosion; the latter term should be applied only to those cases where the cracking progresses directly by an anodic reaction at the tip of the growing crack. Such a definition is theoretically precise but difficult to actually apply, particularly in view of the possible association of anodic processes with hydrogen.

From a microstructural point of view, stress corrosion cracks may take either an Intergranular or a Transgranular path:-

(i) Intergranular stress corrosion cracking

For intergranular stress corrosion to occur, it is believed that the cracks originate at the grain boundaries. These cracks are initiated and propagated by internal or applied stress associated with local anodic action at the grain

boundaries.[11]

The grains with different composition in the matrix (Fig. 5) would set up a galvanic concentration cell between the grain boundary and the grain, with subsequent dissolution of the anodic zone. This anodic zone is usually at the grain boundary, (Fig. 5).

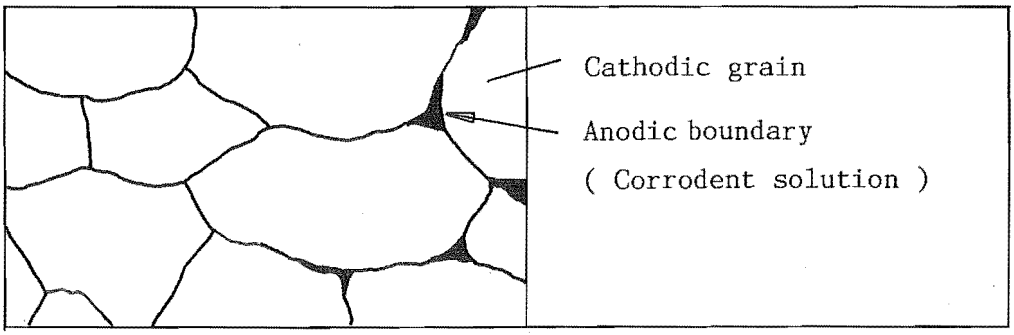

Fig. 5: Description of intergranular attack

In the electrochemical sense, the galvanic corrosion between two metals is well understood. A potential difference usually exists between two dissimilar metals when they are immersed in a corrosive or conductive solution. If these metals are placed in contact, i.e., electrically connected, the potential difference produces electron flow between them. In general, corrosion of the less corrosion resistant metal is usually increased and attack of the more resistant material is decreased, as compared with the behaviour of the metals when they are not in contact. The less resistant metal becomes anodic and the more resistant metal becomes cathodic.

Based on these considerations, it is noted that the mentioned two dissimilar metals also includes the possibility of other combinations, such grain and grain boundary in a metallic matrix.

High strength aluminium alloys depend on precipitated phases for strengthening and are susceptible to intergranular

corrosion. For example, the duraluminium-type alloys (Al-Cu) are strong because of precipitation of the $CuAl_2$ compound.

Robertson and Bakish[18] have pointed out that a substantial potential difference between the copper depleted areas along the grain boundaries and adjacent material or matrix has been observed. From the experimental results, it is deduced that the segregation of the $CuAl_2$ compound in grain boundaries has caused intergranular corrosion along the grain boundary. Indeed, when these alloys are solution quenched, to keep the copper in solution, their susceptibility to intergranular corrosion is very small. On the other hand, grain boundaries are usually more reactive than the matrix, under such conditions, grain interfaces are very reactive and intergranular corrosion results.

It is generally agreed that the addition of chromium to steel may enhance corrosion resistance of the steels in corrosive environments. However, under certain conditions, intergranular fracture can be caused by depletion of chromium in the grain boundary areas (Fig. 6). The most common observed failures of this type is known as 'weld decay' and occurs in the 18/8 austenitic stainless steels.

Erasmus[34] reported that in the temperature range 600-700° C, the sensitized microstructure is produced by chromium depletion along grain boundaries within the heat affected zone formed during welding as a result of $Cr_{23}C_6$ precipitation. More specifically, in the temperature range indicated, chromium carbide ($Cr_{23}C_6$) is virtually insoluble and precipitates out of solid solution, and chromium is thereby removed from solid solution, and the result is metal with lowered chromium content in the area adjacent to the grain boundaries. The chromium depleted zone near the grain boundary is corroded because it does not contain sufficient corrosion resistance to resist attack in corrosive environments. This situation is illustrated schematically in Fig. 6.

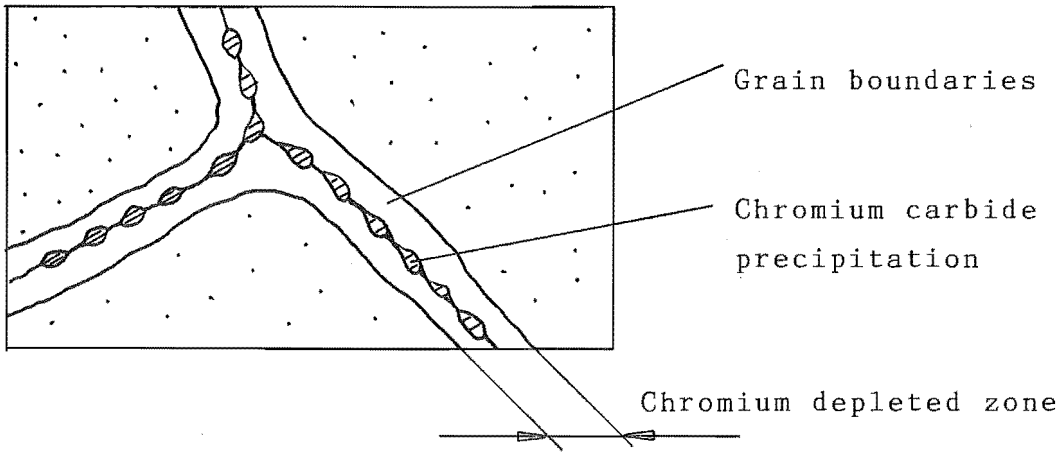

Fig. 6[35]: Schematic illustration of grain boundaries in sensitized type 304 stainless steel

Apparently, in the case of intergranular corrosion, the grain boundary regions could be more anodic, or less corrosion resistance, because of precipitated phases, enrichment of one of the alloying elements, or depletion of one of the alloying elements in the grain boundary areas, thereby providing a susceptible path for crack growth.

It is well known that, small amounts of iron in aluminium, wherein the solubility of iron is low, have been shown to segregate in the grain boundaries and cause intergranular corrosion crack. On the other hand, depletion of chromium in the grain-boundary results in intergranular corrosion of stainless steels.

A recent publication of Bandyopadhyay[33] confirms that the intergranular crack path in high strength steel is an interfacial embrittlement phenomenon due to a combination of impurity elements segregated during the heat treatment of the steel and hydrogen concentrated by the lattice expansion due to hydrostatic tensile stresses.

The role of the tensile stress in intergranular stress corrosion cracking is thought to be one of "tearing" the crack sides apart so as to expose more corrodent to the site of electrochemical attack.

(ii) Transgranular stress corrosion cracking

Stress corrosion cracking is transgranular in austenitic stainless steels (in chloride solutions), in β brass, and for some corrodents in magnesium alloys.[18]

There are two principal postulates as to the initiation and propagation of transgranular cracks.[31] One group of workers consider transgranular cracking to be an example of brittle failure and applies Griffith's criterion for the initiation and propagation of the crack, i.e.,cracks propagate in a series of short, brittle bursts. The second group of investigators proposed that cracking is always a ductile process.[31] This proposal is supported by tests in the laboratory. It is generally agreed that the final failure is by a shearing process as the result of a tensile component of overload.

In the case where transgranular stress corrosion cracking occurs it was traditionally believed that the formation of a protective layer or polarised condition that covers most of the metal is the initial step.[36] This protective layer is often referred to in the literature as a passivating film.

Logan has suggested the tensile stresses destroy the passive film at narrow regions, normal to the applied stress, on the fracture surface.[31] The filmfree material has been discovered to be anodic to the areas of metal which are film covered. These anodic areas are considered to be very small compared with the cathodic areas, and hence rapid electrochemical attack will occur at the anodes, cracks are then initiated. The role of the tensile stress in this theory is one of rupturing the passivating film.

Two recent investigators, Parthasarathi and Polan[29] have shown that transgranular stress corrosion in Cu-Zn-Ni alloys occurs in a solution that forms little tarnish film

on the grain surface. In addition, they have suggested that alloys with low stacking fault energy (i.e., with planar arrays of dislocations) would be more susceptible to transgranular cracking than alloys with higher stacking fault energy (i.e., with cellular arrays of dislocations). It is also believed that the strongly tarnishing film on the surface might protect the fracture surface in the vicinity of the crack tip, and this means that the grain boundaries of high dislocation density, proceed to intergranular cracking.

Finally, it is interesting to note that a further difference between inter- and transgranular corrosion cracking is that the intergranular corrosion remains active even in the absence of applied stress. This could be so serious that the intergranular corrosion often could not be tolerated in practice, even in an unstressed workpiece.[18] In comparison with this, transgranular corrosion cracking is not generally detected in the absence of applied or residual stress.[18]

1.3.3 Stress - Sorption Theory

This theory was first proposed by Uhlig.[37] It has been suggested to arise from reduction of metal bond strength (i.e., the cohesive bond between the surface-metal atoms) by absorption of damaging anions of the corrosive environment at appropriate defect sites and is termed stress-sorption cracking.

It is generally agreed that any kind of absorption, which reduces surface energy would favour crack formation. In this way, it dominates also the stresses necessary to form a new stress corrosion crack.

Stress-sorption theory is based on the assumption that cathodic polarization would effectively inhibit stress corrosion by eliminating the deposition of the anions and associated absorption of damaging corrodent.

The further work of Uhlig and Sava[38] proposed that the mechanism of stress corrosion cracking is one of chemisorption of OH^- or NO_3^- on the metal surface. The absorbate would reduce the surface energy at the crack tip, and the build up of stress concentrations might produce sudden crack extensions which result from the chemisorption process. However, stress corrosion cracking could be prevented or its slow propagation stopped by cathodic protection.

The conjoint action of stress and corrosion required for crack propagation was demonstrated by Priest and co-workers.[16] It has been reported that a growing crack was stopped when cathodic protection was applied. In other words: corrosion stopped —— stress condition unchanged. However, once the cathodic protection was removed, the crack started growing again. The test was repeated several times, and the progress of the crack was photographed.

Hintz and co-workers[39] have studied the SCC of alpha-beta brass in distilled water and sodium sulphate solutions. They have pointed out that the SCC behaviour observed in their studies is most compatible with a SCC mechanism based on the adsorption of one or more damaging species from the corrosive environments. It has been observed that the pH of the solutions and applied electrical potential are significant factors in determining whether cracking of the alloy (alpha beta brass) occurs or not. This is in line with the well known dependence of specific adsorption of ions on both pH and applied potential.

Figure 7[35] shows the effect of pH of distilled water at 50°C on erosion corrosion of carbon steel. As we can see in the figure, low corrosion rates are shown for pH values of 6 and 10 and high rates at a pH 8 and below pH 6. It is thought that the corrosion product (Fe_3O_4) on the steel surface exhibits high rates of deterioration. However, below a pH of 5 the scale (Fe_3O_4) cracked, probably due to the internal stresses, and fresh metal was exposed. It follows,

therefore, the OH^- ions could be adsorbed on defect sites. The formation of $Fe(OH)_2$ and $Fe(OH)_3$ are found to be more protective probably because they hinder transfer of oxygen and ions. Thereafter, the crack must then wait for further slow deformation of the stressed metal to produce a new crack path, or perhaps for electrochemical dissolution to remove an obstruction or to produce the adsorbing ionic species.

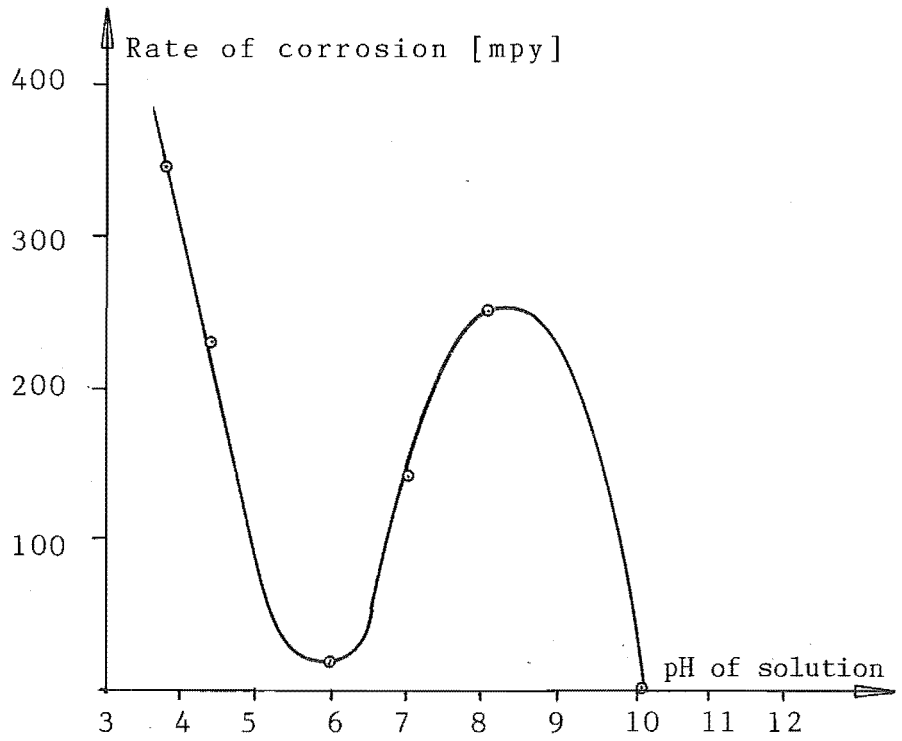

Fig. 7[35]: Effect of pH of distilled water on erosion corrosion of carbon steel at 50° C.

It has similarly been suggested that hydrogen-induced cracking and cracking of metal by liquid metal[40], many characteristics of which are similar to stress sorption cracking, also proceed by reduction of surface energy. An electrochemical corrosion process for explaining the phenomenon of liquid metal embrittlement, of course, is not likely or possible. Therefore, stress sorption mechanism is one of the few mechanisms proposed to describe SCC which has no difficulty in accounting for the special features observed in liquid metal embrittlement study.[40] Apparently stress sorption theory can be categorized either as surface energy reduction or a decohesion model.

1.3.4 Electrochemical - Mechanical Theory

The chemical or electrochemical theory is implicit as playing a part in the initiation and propagation of stress corrosion cracks in most of the mechanisms discussed above. Cowling[9] indicated that cracking can be affected significantly through the use of anodic and cathodic polarisations. This means that the process is not entirely mechanical or electrochemical.

The Electrochemical-Mechanical Theory was first proposed by Keating.[11] He proposed that stress corrosion cracking progresses by an electrochemical-mechanical process in which the electrochemical attack builds up stress concentrations at the tips of cracks. The cracks which initiated by electrochemical attack progress mechanically until the stress concentrations become weak and unable to trigger further mechanical fractures. This process is proceeded by an incubation period as stress concentrations are built up to the point where mechanical cracking is again initiated. Steigerwald, Schaller and Troiano[13] believed that the incubation period of a hydrogenated steel was principally dependent on the diffusion of hydrogen.

There is much evidence to support the electrochemical-mechanical theory in laboratory investigations[13, 14], which show some important features of this discontinuous cracking process. Steigerwald, Schaller and Troiano[13] indicated that the kinetics of crack growth in hydrogenated steel has an important bearing on the mechanism of delayed failure, and they have shown that the crack propagation in a hydrogenated steel was discontinuous by the use of resistance measurements.

Recently, Macdonald and Chung[41] have studied the subcritical crack growth in high strength AISI 4340 steel in 3.5% NaCl aqueous solution at ambient temperature in response to sudden changes in applied stress intensity. The material-

environment system was potentiostatically controlled at cathodic (-1.0 V_{SCE}), open circuit (-0.6 V_{SCE}), and anodic (-0.55 V_{SCE}) potentials in order to ascertain the effect of potential on the crack growth transient behaviour.

Macdonald and Chung[41] have demonstrated the existence of incubation and transient periods during subcritical crack growth in AISI 4340 steel in 3.5% NaCl aqueous solution. They have concluded that:-

1) With sudden application of a constant stress intensity, which is greater than K_{Iscc}, to a stationary crack, steady state crack growth is achieved only after an incubation period of no crack growth and a transient period of time - dependent crack growth rate. The time taken to achieve the steady-state crack growth rate was found to decrease with increasing applied stress intensity.

2) For the case of decreasing applied stress intensity, the time taken to achieve the steady-state crack growth rate was found to increase exponentially with the change in applied stress intensity.

3) The general effect of applied potential is that as the applied potential is made more negative, the time taken to achieve the steady-state crack growth rate is decreased, and the steady-state crack growth rate at a given stress intensity level is increased.

According to Macdonald and Chung, the experimental results are explained in terms of the interaction between hydrogen and the stress distribution ahead of the crack tip. It is proposed that the existence of an incubation period during subcritical crack growth in AISI 4340 steel in 3.5% NaCl solution is a consequence of the delay caused by hydrogen diffusion in achieving a critical hydrogen content in the region of maximum hydrostatic tension.

Macdonald and Chung have indicated that the concentration of hydrogen at the tip of the growing crack will increase as the applied potential is made more cathodic (see

section 1.4). Therefore, it is believed that the time taken to achieve a critical hydrogen content in the region of maximum hydrostatic tension will decrease as the potential is made more negative. The overall effect of these two variable is that the incubation period will be shortened as the applied stress intensity and/or the applied cathodic potential is increased.

It is noted that once a critical combination of hydrogen content and stress level is achieved, a secondary microcrack initiates. Secondary microcrack then grows dynamically on the primary crack plane in both directions (see Fig. 23 of section 1.5). Growth in the reverse direction results in linkage with the primary crack; However, growth also occurs in the forward direction away from the primary crack tip. These cracks will eventually arrest because the local stress level and/or hydrogen content are too low to maintain growth. Subsequently, another secondary crack will initiate and propagate once the critical conditions of stress and hydrogen concentration are satisfied. Based on these considerations, therefore, it is proposed that the primary crack propagates in a discontinuous manner on the microscopic scale because the incubation period for a secondary crack is assumed to be much longer than the propagation time.

Apparently, Macdonald and Chung's study aimed at developing an understanding of the effect of electrochemical potential on crack growth transients. Their experimental results are in qualitative agreement with the electrochemical-mechanical theory, and they tend to support this claim.

The electrochemical-mechanical theory is gaining more favour as a possible mechanism due to the crack propagation rates being too high to support the electrochemical theory alone.

1.4 Hydrogen Embrittlement

Hydrogen embrittlement may be defined as the brittle or quasi-brittle fracture of a material under the conjoint influences of mechanical stress and hydrogen bearing environment. Hydrogen embrittlement is distinguished from stress corrosion cracking generally by the interactions with applied currents . The general characteristics of hydrogen embrittlement and stress corrosion cracking are illustrated in Fig. 8.

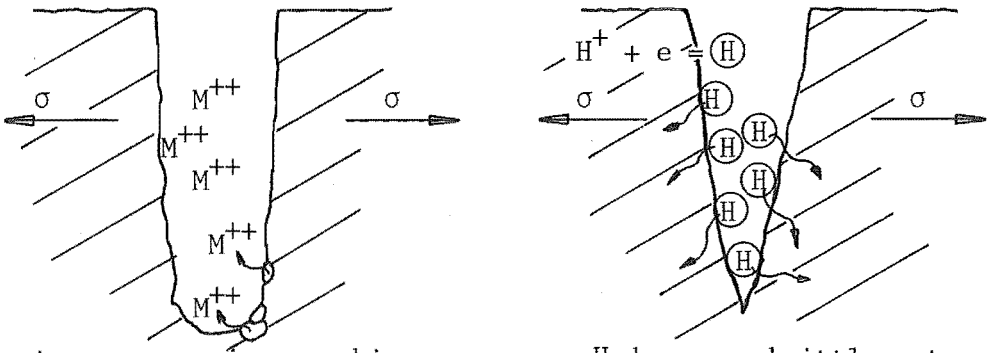

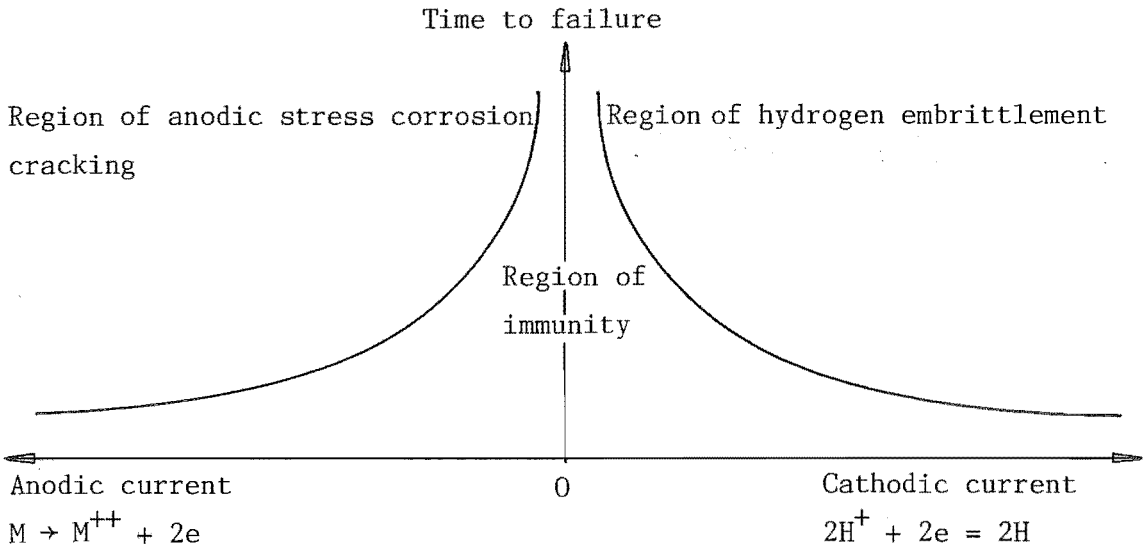

Fig. 8[35]: Schematic illustration of anodic stress corrosion cracking and cathodic hydrogen embrittlement.

As we can see in the figure, the electrochemical nature of stress corrosion cracking and hydrogen embrittlement mechanisms are associated with the following factors:

1) An oxidation or anodic polarization is indicated by an increase in valence or a production of electrons for stress corrosion cracking.
2) A decrease in valence charge signifies a reduction or cathodic polarization for hydrogen embrittlement mechanism.

It is noted that the principal reactions for both electrochemical processes are given by the following equations:

Oxidation (anodic reaction): $M \rightarrow M^{++} + 2e$

(M^{++} : Metal ion)

Reduction (cathodic reaction): $2H^{+} + 2e \rightarrow H_2$

(H^{+} : Hydrogen ion)

Based on the above considerations, it is suggested that, for the case where the applied current makes the specimen more anodic and accelerates cracking is considered to be stress corrosion cracking, with the anodic dissolution process contributing to the progress of cracking. On the other hand, for the case where cracking is accentuated by current in the opposite direction which accelerates the hydrogen evolution reaction is considered to be hydrogen embrittlement.

It is generally agreed[11, 42] that atomic hydrogen is formed in aqueous corrodent by the following reaction:

<u>At the anodic region</u>: anodic polarization (above the corrosion potential)

$Fe \rightarrow Fe^{++} + 2e^{-}$ 1)

<u>At the cathodic region</u>: cathodic polarization (below the corrosion potential)

$H_2O + \frac{1}{2} \cdot O_2 + 2e^{-} \rightarrow 2OH^{-}$ 2)

with

$H^{+} + e^{-} \rightarrow H_{adsorbed}$ (hydrogen discharge) 3)

and

$$2H_{adsorbed} \rightarrow 2H_2 \text{ (catalytic combination)} \qquad 4)$$

Hughes, Lamborn and Liebert believed[27] that stress corrosion cracking of a low-alloy steel (BS 970: En 26) in neutral chloride solution is generally considered to be due to hydrogen embrittlement.

In reviewing the mechanism of hydrogen embrittlement, Meyn[43] has indicated that sufficient hydrogen enters the material under sustained load to have a significant effect on the mechanical properties, considering that hydrogen is likely to concentrate in areas of stress at the crack tips, in this way promoting embrittlement within the grains.

Similar considerations applying to hydrogen embrittlement mechanism have also been established by Parkins[44]. He has pointed out in his recent publication that the adsorped hydrogen may embrittle material in one of two ways:

1) Directly by adsorption at the crack tip region and lowering the surface energy of the material, and thereby lowering the fracture stress of the material.
2) Indirectly by diffusion to some region in advance of the crack tip region where the stress or strain conditions are favourable for crack nucleation. These regions could be the zones of maximum stress triaxiality, and are usually located at the elastic plastic interface of the plastic zone formed at the crack front.

Obviously, the two suggested mechanisms may involve the surface reaction of hydrogen gas with the newly created surfaces at the crack tip, and the diffusion of atomic hydrogen into the crack tip region. It is noted that in the former case where the reactions of the hydrogen gas with the freshly created crack surface lower the surface energy is also defined as 'surface embrittlement mechanism', and the latter case

where the embrittlement reaction involves a region of material ahead of the crack tip is defined as 'volume embrittlement'.(45)

However, Parkins[44] added that there is still no general agreement regarding the mechanism of hydrogen embrittlement. The argument is whether environmentally assisted crack growth in aqueous environments is basically assisted by metal dissolution (i.e., corrosion) or by hydrogen embrittlement.

Hydrogen can be introduced into steel in many ways: during melting and casting, during welding[46], during service in contact with hydrogen gas, during stress corrosion in hydrogen sulphide[9], and even unfortunately during electroplating.[46] The entering of hydrogen into metal can cause problems in various ways. For example[47]:- hydrogen in titanium and titanium alloys has been a major problem of the aircraft industry. Kessler, Sherman and Sullivan[47] reported that hydrogen enters into titanium and titanium alloys during the preparation of sponge and ingots. However, the most recent studies have been concerned with such aspects as crack growth kinetics[48] and the dependence of the threshold stress intensity K_{Iscc} for crack extension in steel on variables like temperature[21], gas pressure[33], electrochemical potential[9] and the alloying elements in steel[49], rather than the significance of the hydrogen embrittlement in other metals. This is possibly due to the fact that steels are the most common material for general engineering application.

It is generally agreed that hydrogen atoms are very mobile. Sandoz[50] has proposed a unified theory for the effect of hydrogen on crack growth in martensitic AISI 4340 steel. The author reported that the effects of hydrogen are principally the same whether the hydrogen is supplied as molecular gas, through stress corrosion, or by electrolytic charging.

Over the past several years, a vast amount of research has been done on hydrogen embrittlement. Resource literature on this topic is therefore abundant. Under these circumstances, the most that has been attempted in this chapter is to summarize some of the features of the phenomenon on which there seems to be fairly general agreement.

In reviewing the current literatures concerning the hydrogen-embrittlement mechanisms, it is obvious that there are four widely accepted postulations which describe the mechanisms of the hydrogen assisted cracking. The four major postulations are:-

I) Embrittlement resulting from accumulated hydrogen at embrittlement sites.
II) Lowering of surface energy by adsorption of hydrogen.
III) Hydrogen interaction with dislocations.
IV) Lowering of the binding energy by interaction of hydrogen.

I. Embrittlement resulting from accumulated hydrogen at embrittlement sites

This mechanism is based on the assumption that the penetration of atomic hydrogen into the metal structure may precipitate from interstitial sites in the lattices forming H_2 molecules. The molecular form of hydrogen (H_2) does not diffuse through solid solution, this creates a high local pressure resulting in small microcracks or voids in the metal.(51)

A schematic illustration of the penetration/adsorption of hydrogen into a metal is given in Fig. 9. The sketch shows that a cross-sectional view of the vessel wall. The material section is exposed to a aqueous solution (e.g. 3.5% NaCl, 0.1 N HCl or 1 N H_2SO_4-aqueous solution), which is considered to be a mild corrodent, but a strong electrolyte.(51, 52)

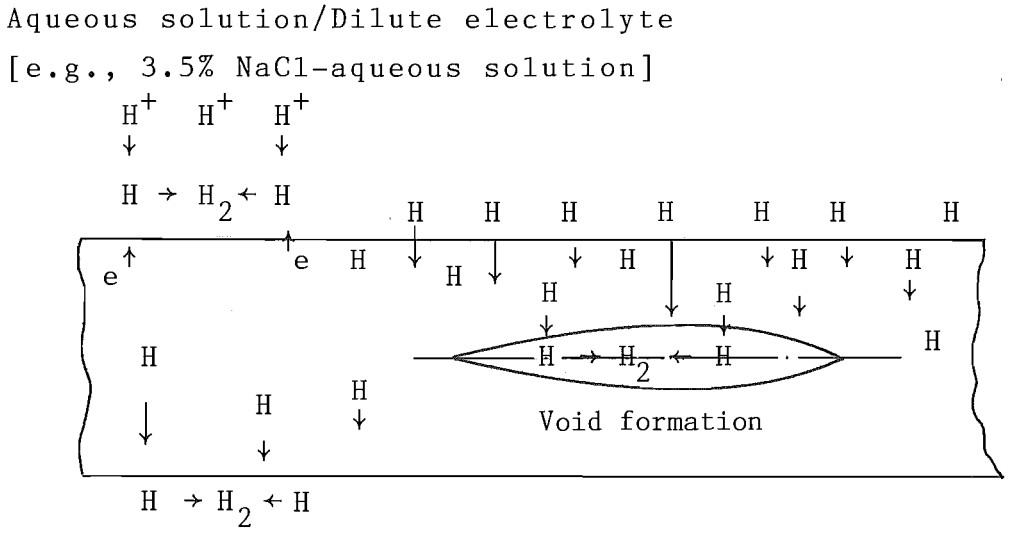

Fig. 9[35]: Schematic illustration showing the penetration or adsorption of atomic hydrogen into a metal.

As we can see in the sketch, atomic hydrogen (H) is the only species capable of diffusion through steel and other metals. Hydrogen embrittlement is produced only by the atomic form of hydrogen. If the hydrogen atoms diffuse into a void (which resulted from the dissolved hydrogen atoms from the interstitial sites), they may combine into molecular hydrogen. Consequently, the formation of hydrogen molecules may create a high gas pressure in the void. According to Fontana and Greene[35], the equilibrium pressure of H_2 molecules in contact with atomic hydrogen could be several hundred thousand atmospheric pressure, which is sufficient to rupture any alloy system (such as steels, Ni-alloys, Ti-alloys etc.).

The internal hydrogen pressure might be reduced if the internal voids extended. As the concentration and pressure of hydrogen gas within the voids decreased, consequently, hydrogen atoms may again diffuse into the extended voids. Due to the formation of the molecular form of hydrogen (H_2), the gas pressure again builds up causing microcrack propagation.

II. Lowering of surface energy by adsorption of hydrogen

This proposed embrittlement mechanism is an extension of the Griffith equation (Sect. 1.2.1, equation 2). As we can see in the Griffith equation the addition of γ, the true surface energy term, may considerably increase the fracture stress.

A facile explanation of hydrogen embrittlement is the reverse argument, i.e., a reduction in the parameters of the true surface energy term (γ) of the Griffith equation may lower the fracture stress for the failure process.

Based on the above considerations, Troiano[53] has suggested that adsorbed hydrogen would lower the resistive cohesive force of the metal lattice. There is general agreement that when a metal fractures, energy must be supplied to create the two new surfaces formed by the crack. Since this energy must be supplied by the applied stress, any decrease in this surface energy could result in fracture at a lower applied stress. It has been suggested that adsorbed hydrogen could be the means of lowering the surface energy, thereby helping crack propagation. More precisely, hydrogen is evolved (e.g. by dissociation) and enters the metal matrix at growing crack tips during aqueous SCC as well as during electrolytic charging, thereby decreasing the strength of interatomic bonds at the surfaces layers (just beneath the first atomic layers) at crack tips[40,53].

With regard to the experimental data supporting the above proposal, Brown and Smith[54, 55, 56] have shown that the electrochemical conditions at the tip of a growing crack were not as same as in the bulk solution. It was observed that the pH measurements of the solution at the crack tip had shown the pH values to be 1.7 in titanium alloys, 3.5 in aluminium alloys and 4.0 for high strength steels, regardless of the pH values of the bulk solutions. The experimental observations are considered to be particularly useful to support the proposed mechanism.

Recently, Jones and Wolfer[57] have studied the modelling of crack growth processes in fusion reactor materials. In the light of laboratory investigations, Jones and Wolfer have proposed that a reduction in the surface energy by hydrogen adsorption was found to cause a decrease in the fatigue threshold stress intensity, and the supporting evidence for the proposal is based on investigations of the effect of the chemical environment on crack growth processes in austenitic and ferritic stainless steels.

III. Hydrogen interaction with dislocations

The hydrogen transport phenomena in metal have been studied by many researchers.[40, 58, 59, 60] They have pointed out that there are many types of the trapping sites which trap hydrogen in metal. For example, they are grain boundary, microvoid, the interface of the nonmetallic inclusion, dislocation, etc. However, dislocation is suggested as a principal trap site among them and its interaction with hydrogen gas has been studied extensively.[40,58,59,60]

Hong and Lee[58] have studied the interaction of hydrogen with dislocations in iron . It is noted that thermal analysis technique was applied in their investigation, and gas chromatograph was used to detect the amount of hydrogen evolved from the specimen. The interaction of hydrogen with dislocations have been investigated from two points of view. One is the trapping nature of hydrogen at dislocation, the other is the effects of hydrogen on dislocation arrangements and dislocation mobility at the various thermal histories and the different atmospheres, respectively.

On the basis of the transmission electron micrographs (TEM) obtained, Hong and Lee[58] have pointed out that:-

1) The amount of hydrogen trapped at dislocations as observed in the thermal analysis was increased when the densely tangled dislocations are loosened by the repeated thermal analysis. Considering these results, it is proposed that hydrogen is trapped at the stress field around dislocation and not at the core of it.

2) The dislocation rearrangement proceeds more rapidly when the specimen is heat treated under the hydrogen atmosphere than under vacuum, and it proceeds most rapidly under a hydrogen atmosphere followed by a vacuum. From this, Hong and Lee[58] believed that the dislocation mobility is increased by hydrogen, especially when the hydrogen escapes from the dislocation to a normal interstitial lattice site, in the abscence of the applied stress.

Recently, Musolff and Smail [59] have indicated that:—

1) If hydrogen within the metal interacts strongly enough with the dislocations, the stress required to move enough of these dislocations at the required velocity may become greater than the fracture stress. The component would then fracture. They added that even if this extreme situation does not occur, impeding the dislocation motion associated with the propagation of a crack allows that crack to grow with a smaller expenditure of energy; i.e., at a lower stress.

2) If several adge dislocations are forced together, a small crack is formed. Any hydrogen associated with these dislocations could then serve to stabilize this crack by combining to form hydrogen gas.

Indeed, Erasmus[60] has also indicated that the "traps" (e.g., dislocations) containing the hydrogen gas at great pressure must normally expand creating voids. For example, when the steel has a low resistance to cleavage crack propagation these voids will appear as long, sharp cleavage cracks. Thus hydrogen pressure alone, in the absence of any externally applied stress, is able to nucleate cracks.

Erasmus[60] added that cleavage crack growth under internal hydrogen pressure is similar to that occurring under an externally applied tensile stress. Initially, the rate of crack growth is slow and occurs plastically by a process of dislocation coalescence. When the crack has grown to a length such that the Griffith criterion for elastic propagation is satisfied, then propagation becomes unstable and crack propagates rapidly. However, since the rate of crack growth is greater than the diffusion rate of hydrogen in steel, essentially no hydrogen enters the crack once rapid propagation begins. The pressure within the crack consequently decreases and propagation is arrested, the crack tip being blunted by plastic relaxation when the crack stops.

A comparative study of stress corrosion cracking, hydrogen assisted cracking, and liquid-metal embrittlement in Al, Ni, Ti and Fe- based alloys has been reviewed in a recent publication of Lynch.[40] He has pointed out that chemisorption of liquid-metal or hydrogen atoms facilitates the nucleation of dislocations at crack tips, and thereby results in crack growth by an alternate-slip process at crack tips combined with some general matrix slip ahead of cracks which produces nucleation and growth of voids. He added that such a process would produce dimpled fracture surfaces macroscopically parallel to {100} planes, with crack growth in <110> directions.

In the light of laboratory investigations, Lynch has concluded that crack growth in embrittling environments occurs by plastic flow. It follows, therefore, that since adsorption can only influence the first few atomic layers at freshly cracked surfaces at the crack tip region, an effect on the nucleation or egress of dislocations at crack tips must be responsible for the effect of environment on crack growth.

We note that Lynch's conclusion has been explained in terms of the adsorption/dislocation-nucleation model. This model fits well with most laboratory observations[53, 68, 74 77, 78] cited in the present thesis.

IV. Lowering of the binding energy by interaction of hydrogen

Consider the combination of two atoms M and H to form a diatomic molecule MH. Let us assume that O_M is the atomic orbital of an electron in atom M which concerns the combination, and O_H the atomic orbital of a similar electron in atom H.

If we put O to be linear combination of the atomic orbitals, then we can write:

$$O = O_M \pm C \cdot O_H \qquad 1)$$

Where C is a factor which weights the relative contributions of O_M and O_H to O. The factor +C, representing the two atoms M and H, which is called a bonding molecular orbital, and the electrons in it are called bonding electrons. On the other hand, the factor -C, corresponding to the difference between the two atomic orbitals, leads to repulsion between atom M and H, which is known as an antibonding molecular orbital, and the electrons in it are said to be antibonding.

Based on the above considerations, Maron and Lando[61] have shown that whether a given electron is bonding or antibonding may depend on the interaction of the atomic orbitals. If these orbitals overlap appreciably and lead to a concentration of electronic charge between the nuclei, then bonding results. However, when the atomic orbitals repel each other, no overlap or concentration of charge between M and H is possible. We then get a strong repulsion between the two nuclei, and no bonding can take place.

Based on the concept of bonding and antibonding electrons, Erasmus[51] stated that an addition of hydrogen electrons entering the 3d-band of the transition metals (i.e., the 10 elements of Sc, Ti, V, Cr, Mn, Fe, Co, Ni, Cu, and Zn of the fourth period in the periodic table) may produce antibonding orbitals. The arrangement of electrons in transition metals is illustrated in table 1.

Table 1 : Electron configuration of transition metal[61]

Shell		K	L		M			N			
Subshell		1s	2s	2p	3s	3p	3d	4s	4p	4d	4f
At. No	Element										
21	Sc	2	2	6	2	6	1	2			
22	Ti	2	2	6	2	6	2	2			
23	V	2	2	6	2	6	3	2			
24	Cr	2	2	6	2	6	4	1			
25	Mn	2	2	6	2	6	5	2			
26	Fe	2	2	6	2	6	6	2			
27	Co	2	2	6	2	6	7	2			
28	Ni	2	2	6	2	6	8	2			
29	Cu	2	2	6	2	6	10	1			
30	Zn	2	2	6	2	6	10	2			

It is generally agreed that in the 3d-band of the transition metals, additional electrons go into an inner electron shell (except Cu & Zn), whereas the number of electrons in the outer shell tends to remain constant. Therefore, the outer shell electrons experience similar forces of attraction in these atoms. However, from the standpoint of electron probability or electron charge density, increasing the number of electrons in the 3d-band of the transition metals would increase the repulsive force between the positively charged nuclei, thereby lowering the fracture resistance of the metal. In short, the effect of the electronic donation of electrons from hydrogen to the 3d-band of the transition metals would lower the fracture stress of the interatomic bond.

Therefore, the electronic donation of electrons from hydrogen to the 3d-band of the transition metals would lower the fracture stress of the solid solution.

Mc Lellan and Harkins[62] have indicated that the formation of the hydride compound TiH_2 in titanium alloys is thought to be a classical example for the postulation. Further examples are provided by Birnbaum[63] in his recent study concerning the hydrogen-related second-phase embrittlement of solids. It is pointed out that the hydride formation in V, Ti, Mg, Nb, Ta, and Zr base alloys has been clearly shown to sensitive to the application of external stress.

In reviewing the current publications concerning the four postulations for the hydrogen embrittlement mechanism, it is obvious that the first, second and third postulations (i.e.,'Embrittlement resulting from accumulated hydrogen at embrittlement sites', 'Lowering of surface energy by adsorption of hydrogen',and 'Hydrogen interaction with dislocations') are found to be more favourable for explaining the failure mechanism.

With regard to the fourth postulation (Lowering of the binding energy by interaction of hydrogen), it is apparent that the postulation is important academically, however, it is probably of secondary importance from a practical view.

1.4.1 Hydrogen Embrittlement In Steels

Hydrogen embrittlement is a very common and one of the most serious failures encountered in steels. Shaw and Johnson[64] have pointed out that hydrogen embrittlement of steels can be broadly classified into the three categories:-

High strength steels, with yield strengths of the order of 1200 MPa which are prone to cracking in pure hydrogen gas, intermediate strength steels ($\sigma_y \simeq 850$ MPa) which are less susceptible to fracture in hydrogen gas but crack readily in H_2S gas, and low strength steels ($\sigma_y \simeq 500$ MPa) which will only crack in hydrogen charged aqueous solutions.

The environment assisted crack growth in high strength steels and other high strength alloys in hydrogenous environments (such as H_2O and H_2S) has been reviewed in a recent study of Wei[65]. It has been reported that the crack growth response in hydrogen embrittlement of ferrous metals by external environments may be controlled by five major processes operating in sequence, and causing failure of a structure or component by the conjoint action of mechanical stress and corrosion.

According to Wei[65], the five sequential embrittlement processes are:

1) Transport of hydrogen or hydrogenous gases to the crack tip region.
2) Sequential processes involved in the reactions of hydrogen gas or gases with freshly created crack surfaces to evolve hydrogen (namely, physical and dissociative chemical adsorption).
3) Atomic hydrogen entry into the solid solution (or by adsorption).
4) Diffusion of hydrogen to the fracture zone.
5) Hydrogen-metal interactions leading to embrittlement (i.e., the embrittlement reaction).

It is noted that the above-mentioned embrittlement sequences that correspond to hydrogen embrittlement of high strength steel are only valid for embrittlement reactions at relatively low temperature, the high temperature fracture processes, such as internal oxidation, and hydrogen attack[66] (A form of material degradation which occurs when steels are exposed to a high temperature, high pressure hydrogen environment) are excluded from the discussion.

Fig. 10 shows a schematic illustration of the various embrittlement sequences.

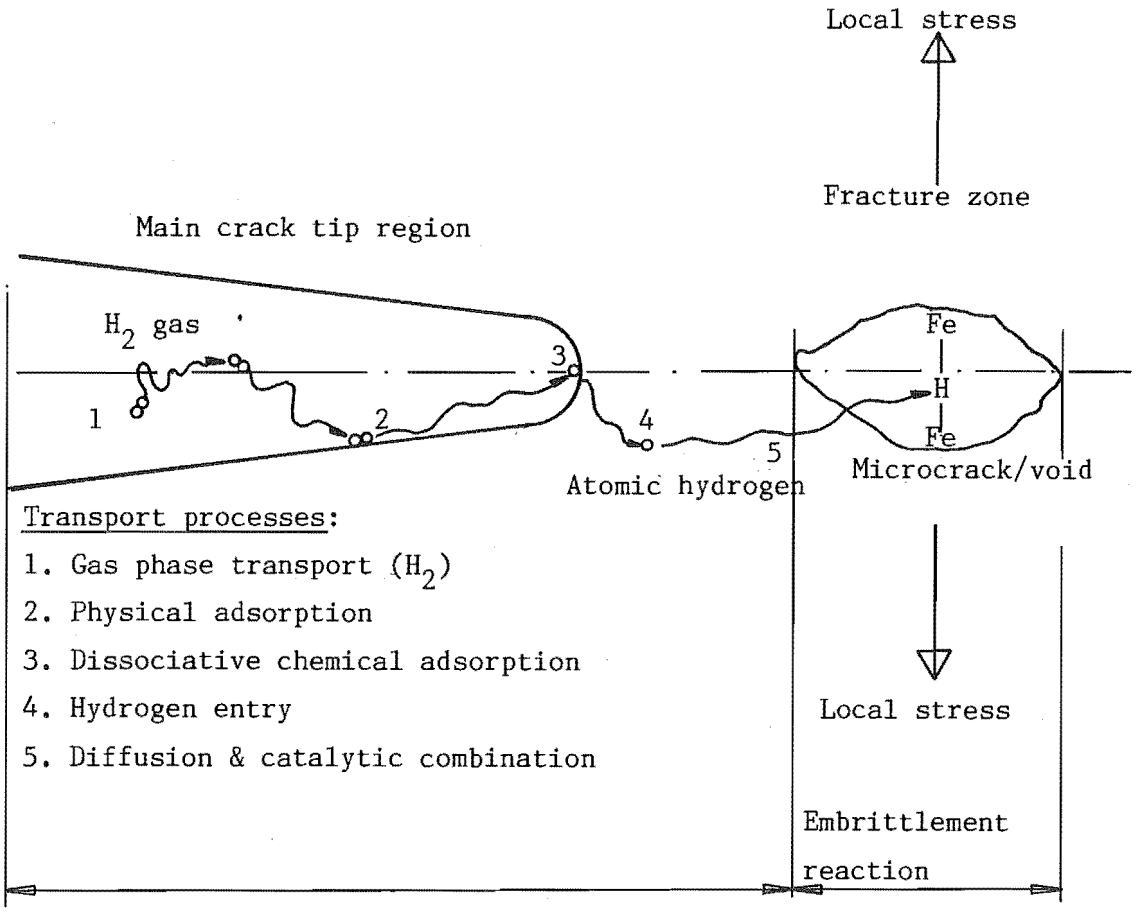

Fig. 10[65]: Schematic illustration of various sequential processes involved in embrittlement of ferrous alloys by external environments.

From the illustrative example, we see that environment assisted crack growth is dependent on the production of freshly cracked surfaces at the crack tip region, and the fracture process zone is located in the vicinity of the main crack tip.

Based on the above considerations, currently Gao and co-workers[67] have indicated in their studies that fractographic analysis of AISI 4340 steel fractured under sustained load in hydrogen and in hydrogen sulphide (over a range of temperatures and pressures) gave no evidence of crack nucleation in advance of the main crack, therefore, it has been concluded that the fracture process zone is located within one prior-austenite grain diameter from the main crack tip.

Another major point arising from Gao's investigation[67] is that, for high temperature hydrogenous environments, the cracking occurred predominantly by intergranular separation and microvoid coalescence. If a steel is exposed to a high temperature, high pressure hydrogen environment, decarburization may occur. The removal of carbon (i.e., decarburization) from the matrix may result in an increase in ductility of the steel. It follows, therefore, that microvoid coalescence or ductile rupture is produced by separation of the voids during plastic straining of the solid solution. The decarburization produced in a hydrogen environment at high temperature, is discussed later(See P. 63).

For crack growth in a high strength steel at low temperature, Gao and co-workers have indicated that the hydrogen-assisted cracking followed predominantly along prior austenite grain boundaries, with a small amount of quasi-cleavage separation. Moreover, it is reported that the prior-austenite grain boundaries are thought to be most susceptible to hydrogen embrittlement, followed by the [110] and [112] cleavage planes. It is noted that, the fracture mode of cracking following predominantly along prior austenite grain boundaries with a small amount of quasi-cleavage separation, is thought to agree with the current fractographic results, obtained from

ULTIMO-200 steel fractured in 3.5% NaCl aqueous solution, where the failure mechanism is suspected to be due to hydrogen embrittlement.

From consideration of the low ductility of high strength steels in common use, it may be noted that cleavage and quasi-cleavage commonly appear in the rapid fracture region (e.g. Region III of SCC-test) of high strength steels. This is due to the fact that high strength steels are usually very much cleaner than plain carbon steels. Therefore, they require much less hydrogen for the embrittlement reaction. In addition, it could also be deduced that high strength steels are inherently notch sensitive, and to accommodate hydrogen gas pressure within the voids in the fracture zone (Fig. 10), these steels will crack rather than flow plastically as plain carbon steels.

In developing a suitable model for stress corrosion crack growth in high strength steel, Hirose and Mura[68] have also indicated that hydrogen-assisted crack growth followed predominantly along prior-austenite grain boundaries, and the crack advances step-wise by connecting the detached micro-crack or void formed ahead of the main crack.

Apparently, Gao, Hirose and their co-workers suggest that hydrogen embrittlement of high strength steels involves a region of material ahead of the crack tip; that is, it occurs by a "volume embrittlement" mechanism as opposed to a "surface" mechanism in which suggested that the embrittlement reaction involves the freshly created crack surfaces at the crack tip.

The experimental evidence shows that volume embrittlement may result from interactions of the microstructure with the accumulated hydrogen. The atomic hydrogen entering the material, would either reduce the interatomic bond strength, or be trapped at several different types of defects in steels (for example: dislocations, impurity atoms, inclusion parti-

cles, as well as interfaces between the matrix and carbide particles etc.), consequently altering the local chemistry or microstructure (for example: hydride formation and decarburization).

Alloy steels usually contain significant amounts of alloying elements (such as Mn, P, S, Cr, Mo and V etc.), which are known to increase the machineability, hardenability, strength, and impact resistance of the steels. For example: Machineability of the free-cutting steels is improved by manganese sulphide inclusions; phosphorous increases the rate of strain hardening and the machineability (up to 0.4% of phosphorous) of free-cutting steels[60]; and the carbide stabilizing elements such as Cr,Mo and V form $Cr_{23}C_6$, Mo_2C and V_4C_3-coherent alloy carbides result in significant secondary hardening in high strength steels[5, 60].

However, the carbide stabilizing elements would reduce the ductility of the steels, making the steel more susceptible to hydrogen embrittlement, although these alloying elements such as Mn, Cr, Mo and V are seen to increase the resistance of the steels to hydrogen attack in high temperature, high pressure hydrogenous environments.[21, 66, 69]

Recently, the effect of alloying elements on hydrogen embrittlement in high strength steel was investigated. Nakamura and Furubayashi[49] who have pointed out that alloying elements such as Mn and C have a significant effect on the crack propagation behaviour in high strength steel.

They studied the roles of Mn and C on the threshold stress intensity (K_{Iscc}) which decreases with an increase in C content and increases with Mn content up to 0.84 Wt % followed by a decrease in K_{Iscc} with an increase of Mn content from 0.84 to 2.13 Wt %. K_{Iscc} was significantly low for specimens without any Mn content. The crack propagation behaviour of delayed fracture of the high strength steel was investigated in pressurized hydrogen gas in the pressure range

up to 784 KPa at room temperature.

Referring to the dependence of hydrogen embrittlement on carbon content, it has been thought to be associated with the tempering temperature, which increases with an increase in carbon content, consequently the precipitation of non-coherent cementite particles increases with the tempering temperature.

It is well known that the precipitated non-coherent cementite particles along the grain/martensite lath boundaries are normally hard and brittle. Therefore, it is reasonable to deduce that those boundaries containing hard and brittle cementite particles networks might be weakened by means of cracking of the cementite particles themselves in the hydrogenous environment or suffer decohesion from the matrix at or near the cementite inclusion ends[69] which promotes intergranular embrittlement.

Similar to the effect of carbon on hydrogen-induced cracking, the addition of manganese in high strength steel has been thought to promote the segregation of phosphorous to grain or martensite lath boundaries. The result of an increase in the crack propagation rate with an increase of manganese content could be due to the hydrogen embrittlement of grain or martensite lath boundaries caused by the intergranular phosphorous segregation.

Nakamura and Furubayashi[49] have also pointed out that the fractographic results of the specimens fractured in hydrogen gas were almost entirely intergranular with a small amount of quasi-cleavage facet on the fracture surface and for the specimens fractured in air, the fractographic results showed basically dimple rupture fracture surfaces.

On the basis of the fractographic results obtained, it can be deduced that the susceptibility to hydrogen-induced

crack initiation in high strength steel is related to intergranular fracture. Indeed, the statement has been supported by Bandyopadhyay and co-workers[33], who have recently pointed out that measurements of the threshold stress intensity (K_{Iscc}) for hydrogen-induced cracking in 4340-type steel is associated with intergranular fracture initiation in hydrogenous environments.

The results presented by Bandyopadhyay and co-workers are detailed in Sect. 1.5. However, it should be emphasized that the results also provided a considerable amount of experimental data which proved that the tendency for intergranular hydrogen-induced cracking is related to the segregation of phosphorous and sulphur to the prior austenite grain boundaries.

Based on the above considerations, therefore, it is reasonable to assume that hydrogen embrittlement in steels is associated with the non-metallic inclusions. Indeed, Ryall and co-workers[70] have also indicated that the non-coherent precipitates, such as sulphide inclusions, or phosphorous segregation along the grain boundaries have the property of contracting more than the steel matrix during cooling, resulting in internal voids in the steel/inclusion interface.

It is considered that the interfaces between non-metallic inclusions and the steel matrix serve as sinks or traps for initial hydrogen precipitation. The atomic hydrogen may diffuse into the voids and interfaces where it recombines and precipitates internally as molecular hydrogen gas. Extremely high local gas pressure may be generated at these internal voids, finally resulting in the fine hairline cracks in the steel matrix[60].

Ryall and co-workers[70] reported that carbon-manganese steels with sulphur contents less than 0.01% are much more prone to hydrogen-induced cracking than steels having a sulphur content in the higher range of 0.020 to 0.030 Wt %.

In keeping with this view, it seems reasonable to believe that the non-metallic inclusions and non-coherent precipitates in steel may increase the steel's resistance to internal hydrogen embrittlement, this is probably due to the fact that the non-metallic inclusions and the non-coherent precipitates in steel can be expected to provide a large proportion of the internal void volume, the more voids in the solid solution the less pressure can be built up for a given hydrogen content, hence less internal embrittlement reactions will occur.

Following the above reasoning, therefore special attention must be paid to the steelmaking process, because high sulphur content steels are unacceptable for the engineering components and structures in which higher toughness and good weldability are required.

Decarburization, or the removal of carbon from steel is often produced in hydrogen environment at high temperature. (21, 35, 66) It is generally agreed that ferrous alloys are often strengthened by interstitial carbon or by carbide precipitations in the matrix. However, if the ferrous alloys are exposed to hydrogen gas at high temperature, hydrogen attack may occur by decarburization of the matrix accompanied by the formation of hydrocarbons or methane gas (CH_4). The principal reaction is given by the following equation:-

$$M_xC + 2H_2 = CH_4 + x \cdot M$$

As we can see in the above equation, carbides (e.g., Fe_3C) or dissolved carbon (indicated as M_xC) may react with the hydrogen gas to form methane gas in the hydrogenous environment at high temperature. Obviously, the reaction results in the removal of dissolved carbon from the solid solution. Consequently, the removal of carbon from the steel may lower the tensile strength, and increase the ductility of the steel. On the other hand, since atomic hydrogen diffuses readily in the metal structure, hydrogen-induced cracking may

result from the formation of methane gas (CH_4) in internal voids (also known as methane bubbles in steel).

Recently, Shewmon[21] has studied the hydrogen attack of pressure vessel steels. He reported that the formation of methane bubbles along the grain boundaries in hydrogen attack of the steel is associated with the following sequences which proceed simultaneously during the decarburization process.

1) Diffusion of atomic hydrogen to the methane bubbles.
2) The carbide dissolution and carbon diffusion.
3) The formation of methane gas at the bubble surface.
4) Surface diffusion of iron atoms toward bubble tip, consequently, diffusion of Fe atoms along the grain boundary.
5) Accommodation by creep of the adjacent grains.

It is noted that the development of the methane gas bubbles along the grain boundaries and their growth to fissures in hydrogen attack of steel is illustrated in Figs 11 and 12.

With regard to the nature of the nuclei for the bubble formation, Shewmon[21] has pointed out that the mechanism remains unclear. However, Sundararajan and Shewmon[66] had indicated that the bubbles did not nucleate on the visible inclusions, and it had been thought to be related to the hydrogen traps or sinks which have evaded fractographic observation to date.

Referring to the bubbles link-up into fissures, it is reported that the formation of fissures is limited mainly by grain boundary diffusion, and the factors limiting bubble nucleation are considered to be due to the local methane gas pressure associated with the applied tensile stress. In order to gain more evidence to support the above considerations, Shewmon[21] has indicated that further laboratory work has to be done.

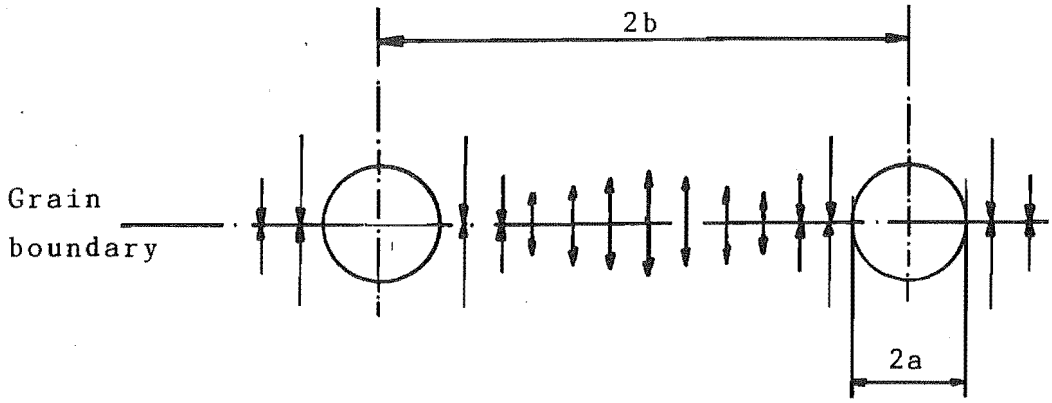

Fig. 11a): Bubbles of radius a and spacing 2b on grain boundary; Arrows normal to the grain boundary represent sign and magnitude of local stress in matrix which results from uniform deposition of atoms between bubbles.

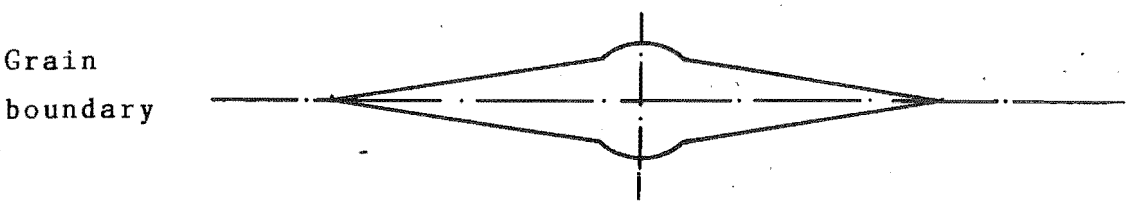

Fig. 11b): Due to the higher stresses (the local methane gas pressure and the applied tensile stress) and greater relative boundary diffusion, the existing bubble has changed to a disc-shaped bubble.

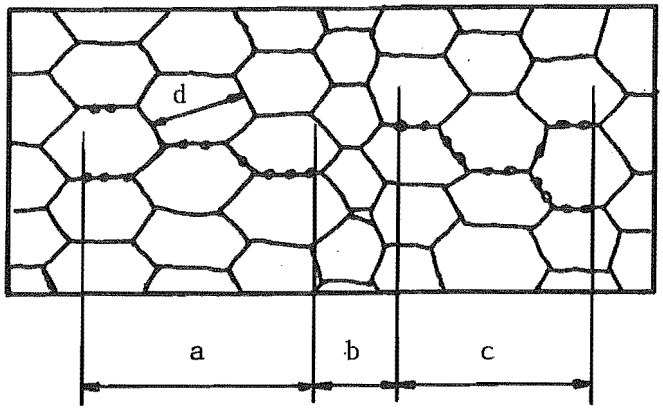

Fig. 11c): Schematic illustration of discontinuous nature of 'bubbled' grain boundaries: d is the grain diameter, b represents the bubble free regions, which must accommodate expansion of 'bubbled' boundaries via lattice/dislocation creep and boundary sliding.

Fig. 11 : Schematic illustration of spacing and distribution of bubbles used to describe bubble growth sequence. (21)

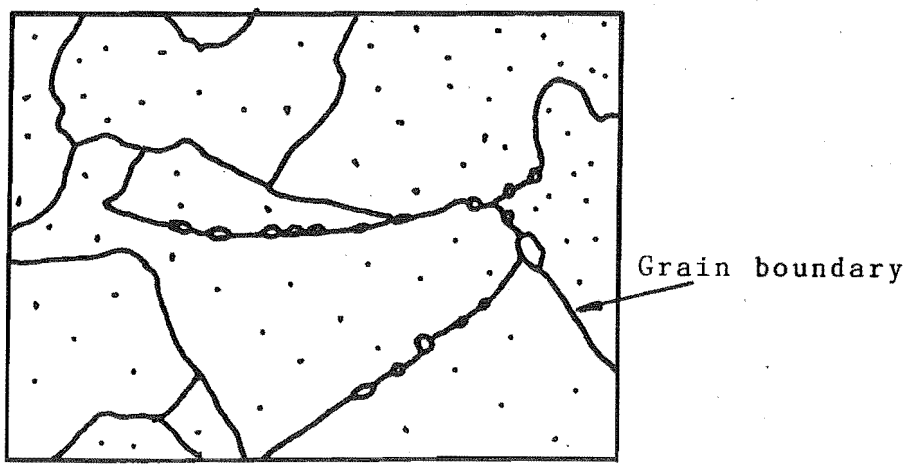

Remarks: ○○ : Methane bubbles

⌇⌇⌇⌇ : Bubble link-up into fissures

Fig. 12 : Schematic illustration of methane bubbles in hydrogen attack of steel.(21)

Fontana and Greene[35] indicated that chromium and molybdenum additions to steel improves its resistance to cracking and decarburization in hydrogen atmospheres. Indeed alloying with carbide stabilizing element can significantly increase the steel's resistance to hydrogen attack.

In the light of laboratory investigations, Shewmon[21] has pointed out that alloying with chromium improves the steel's resistance to hydrogen attack by means of reducing the methane gas bubble density. However, Shewmon[21] added that chromium has insignificant effect on the bubble growth rate.

The tendency to hydrogen attack is proportional to the carbon activity in the steel.[66] Alloying with the carbide stabilizing elements such Mo, Cr, V, Ti or Mn may decrease the activity of carbon in steel, thereby improving the resistance of the steel to hydrogen attack.

In many instances, hydrogen gas streams may contain water vapour, and other reactions may occur. An interesting example of the case is that wet hydrogen is capable of decarburizing steels by the following reaction at the steel/water interface[35]:

$$C_{(Fe)} + H_2O = H_2 + CO \quad \text{(Decarburization process)}$$

As we can see in the above equation, carbides (for example Fe_3C) or dissolved carbon may react with the water or water vapour to form hydrogen and carbon monoxide. Fontana and Greene[35] have pointed out that the rate and direction of the above reaction are associated with the carbon activity in the ferrous alloy/steel and on the amounts of water vapour, carbon monoxide, and hydrogen in the gas stream. However, if the ferrous alloy or steel is exposed to a high-temperature water vapour environment, the diffusing hydrogen presumably results from the following reaction:

$$Fe + H_2O = FeO + H_2 \quad \text{(Oxidation/anodic reaction)}$$

Based on the above considerations, therefore, it has been deduced that in hydrogen-water vapour environments both decarburization and oxidation are possible. In general, it can be said that both water and water vapour can supply hydrogen to the surface of steel, and under certain circumstances, atomic hydrogen will diffuse into the metal matrix causing the deleterious embrittlement.

Regarding the effects of moisture on hydrogen embrittlement, concrete evidence was established by Hancock and Johnson [71]. They have investigated hydrogen-induced cracking in H-11 type high strength steel associated with various chemical environments, and their experimental results are summarized in Table 2.

Table 2: Subcritical crack initiation stress intensity (K_I)

Pressure	atmospheric		
Chemical environment	hydrogen	wet argon	dry argon
K_I ($MN/m^{3/2}$)	12	20	44

As we can see in Table 2, the embrittlement potential of humidified argon has a lower subcritical crack initiation stress intensity (K_I = 20 $MN/m^{3/2}$) than that of dry argon (K_I = 44 $MN/m^{3/2}$). This indicated that the rate of crack growth in a humid environment is more rapidly than that in a dry environment.

Although the effect of capillary condensation at the crack tip has not been demonstrated from the investigation directly, it is believed that in highly humidified environments the stress corrosion or hydrogen-induced crack may propagate

in a little pool of condensate water associated with a certain hydrostatic pressure. In keeping with this view, the average measurement of the subcritical crack initiation stress intensity is lower in wet argon than in dry argon. However, the molecular gas (e.g. carbon monoxide, or hydrogen gas) pressure within the voids in the plastic region just ahead of a crack tip is believed to be much a higher value than that of the condensate water. Under these circumstances, therefore, the influence of the hydrostatic pressure due to the condensate water may be considered to be less significant.

Another feature of hydrogen embrittlement is hydride formation in metals. Erasmus[51] has indicated that, if an engineering component is exposed to a hydrogen atmosphere, the amount of hydrogen adsorbed during the exposure to H_2 gas is a complex function of temperature.

According to Petrucci[52], hydride formation occurs preferentially in those metals that adsorb large quantities of hydrogen under exothermic reactions. For example, in the following compounds the hydrogen may exist as the hydride ion (H^-):

1) Alkali metals: i.e., those metals having a single electron in the outermost electronic shell, e.g., Ag^+, Cu^+, Na^+ etc.
   Symbol: M^+
   Principal reaction: $2M^+$ (solid) + H_2 (gaseous) → $2MH$ (solid)

2) Alkaline earth metals: i.e., those metals having a pair of electrons in the outermost electronic shell, e.g., Cr^{2+}, Fe^{2+}(ferrous), Cu^{2+}, Mg^{2+}etc.
   Symbol: M^{2+}
   Principal reaction: M^{2+} (solid) + H_2 (gaseous) → MH_2 (solid)

The characteristic ionic charges of some common metals are presented in Table 3.[52] With reference to the table, we can see that hydride formation may not occur in ferrite phase iron/steel in common use. Indeed, Erasmus has also pointed out that hydride formation is not possible in iron base alloys.[60] This is probably due to the fact that the ferrite phase iron/steel with triple positive charged cation (Fe^{3+}) is neither an alkali nor alkaline earth metal.

It is reported that the presence of embrittling hydrides is thought to be very stable at low temperature[60], where dissolved hydrogen reacts to form brittle hydride compounds. For example: TiH_2-hydride compound in titanium alloys.[62]

The solubility of hydrogen in iron/steel will be insignificant at low temperature. Indeed, the hydrogen solubility of iron or steel decreases with a decrease in the temperature (Fig. 13). Ryall and co-workers[70] have indicated that at temperatures below 200°C the retained hydrogen in steel is precipitated at inclusion sites and other voids within the steel in molecular form, and the pressure of hydrogen gas within the voids or inclusion sites may result in the cracking known as hydrogen flakes (the defects consisting of numerous hairline cracks occur preferentially in high strength steel).

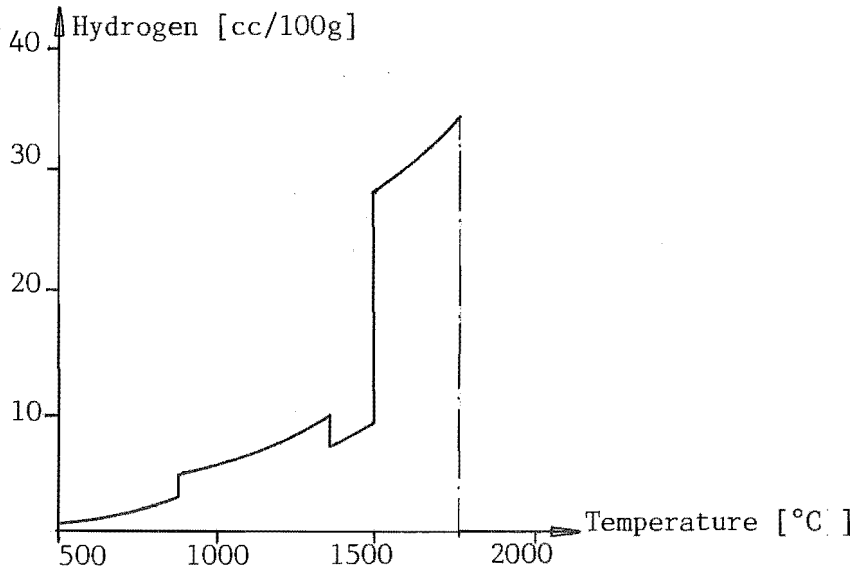

Fig.13[60]: The solubility of hydrogen in iron/steel.

Table 3[52]: Some simple ions

Name	Symbol	Remarks
Positive ions (cations)		
Sodium Copper (I) or cuprous Silver	Na^+ Cu^+ Ag^+	Alkali metals Symbol: M^+
Iron (II) or ferrous Chromium (II) or chromous Magnesium Copper (II) or cupric Zinc Titanium	Fe^{2+} Cr^{2+} Mg^{2+} Cu^{2+} Zn^{2+} Ti^{2+}	Alkaline earth metals Symbol: M^{2+}
Chromium (III) or chromic Iron (III) or ferric	Cr^{3+} Fe^{3+}	Ferric ion
Negative ions (anions)		
Hydride	H^-	

As pointed out previously, Birnbaum[63] has studied the hydrogen related second-phase embrittlement of solids. It has been reported that those alloys based on the group Vb metals (i.e., V, Nb, Ta), on Ti, Mg and Zr, form comparatively stable hydrides in the absence of applied stress, and the thermodynamics of these hydrides has been observed to be sensitive to the applied loads. In addition, Birnbaum has confirmed that the formation of brittle hydride compounds at crack tips has been clearly shown to play an important role in the hydrogen embrittlement of non-ferrous alloys. On the other hand, in those alloys based on Al, Ni and stainless steel, the hydrides are thermodynamically less stable, therefore, the effects of hydrides in the fracture process are thought to be less significant.

Since in this section, attention is focused specifically on hydrogen embrittlement in steels, therefore, no further discussion is given to aspects of hydride-formation peculiar to non-ferrous alloys.

1.4.2 Fracture modes of hydrogen-assisted cracking in steels

It is difficult to establish singly the characteristic fracture mode induced by hydrogen. This is due to the fact that the dominant fracture mode of a hydrogen charged specimen may differ according to applied stress level, strain rate, and microstructure.[72, 73, 75] Although it is complex, fractography has shown that the basic modes of hydrogen assisted cracking can be broadly classified into the four categories of microvoid coalescence (MVC), cleavage (C), quasicleavage (QC), and intergranular cracking (IG). It is important to note that these fracture modes do not necessarily exhibit characteristics of fracture induced only by hydrogen but also are observed in the case of other cracking processes.

Microvoid coalescence occurs preferentially in 1090 or 1045 steels having a spheroidized microstructure. In these materials, fracture of hydrogen charged specimens is usually by dimple rupture or more precisely, by a process of microvoid coalescence[72, 73, 74]. It is reported that small precipitate particles, undissolved carbides, non-metallic inclusions and brittle constituents in the solid solution usually act as nuclei for fracture by microvoid coalescence.

A sketch of four fracture modes (MVC, C, QC, and IG) is presented in Figs 14a-d. It should be emphasized that the schematic illustration of fracture mode development from a single type of fracture nucleus is also intended to include the possibility that other microstructural nuclei exist (e.g. carbide particles, sulphide inclusions etc). The MVC case is illustrated in Fig. 14a, Fig. 14b is for the cleavage mode, Fig. 14c is for the QC mode, and Fig. 14d is intergranular cracking.

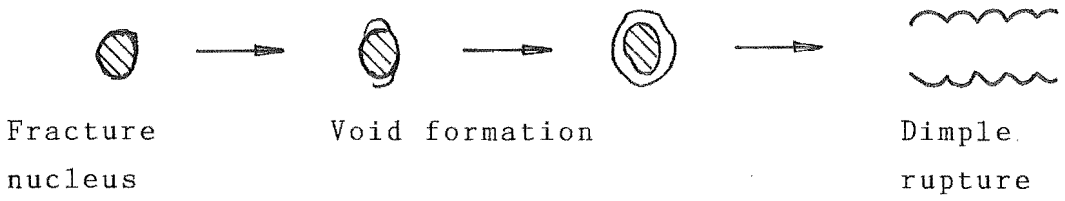

Fig. 14a) : Microvoid coalescence or dimple rupture.

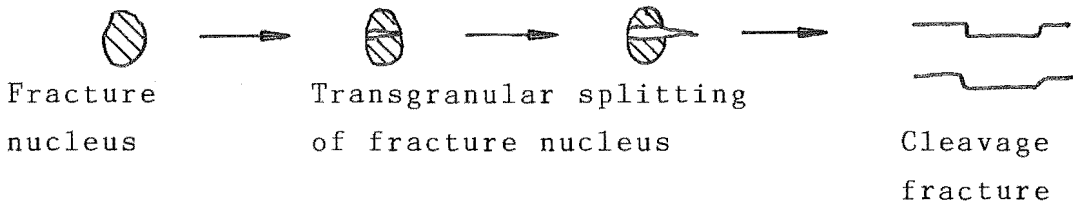

Fig. 14b) : Cleavage fracture.

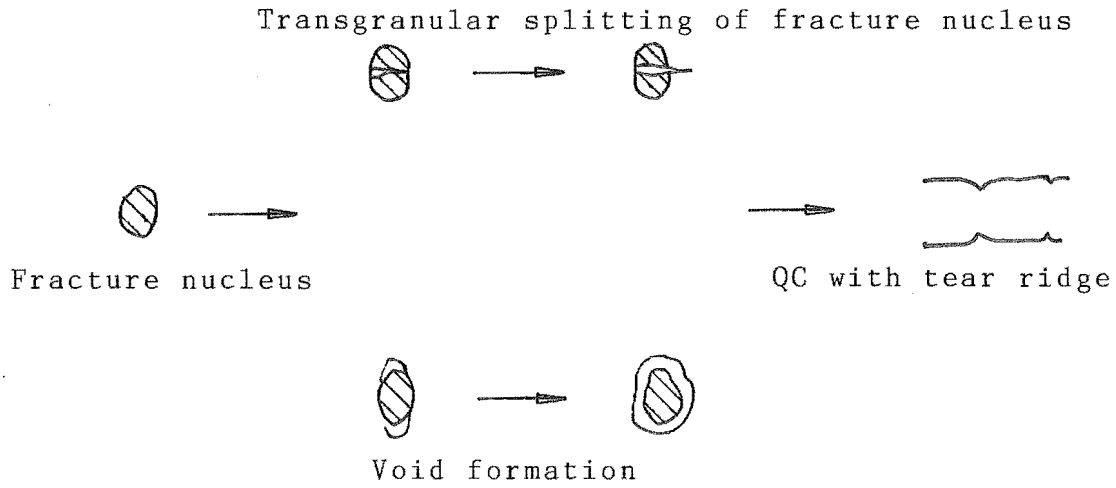

Fig. 14c) : Quasi-cleavage fracture.

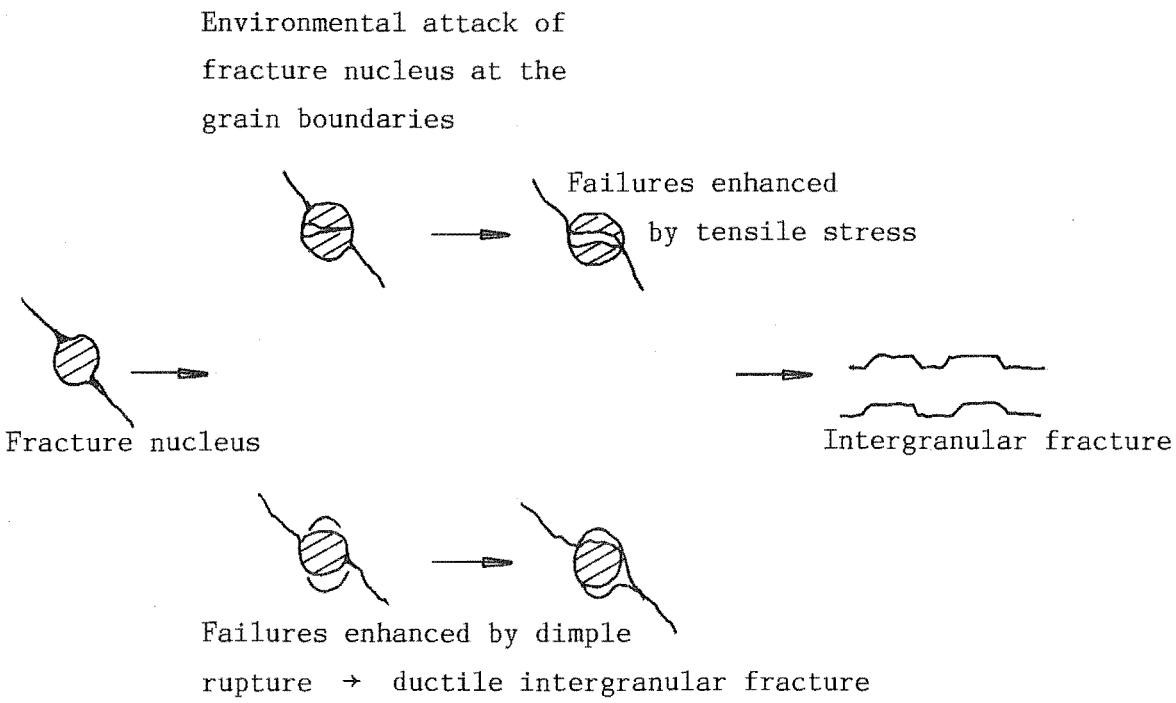

Fig. 14d[72]: Intergranular fracture

Thompson and Bernstein[72] have examined the influence of dissolved hydrogen on the fracture surface in spheroidized 1045 steel. They have pointed out that in tensile tests on spheroidized 1045 steel, fracture surfaces were almost entirely composed of microvoid coalescence both with and without hydrogen charging.

Erasmus[34] thought that when the solid solution around the fracture nucleus deforms plastically under triaxial stress conditions, the internal free surfaces around the fracture nucleus are propagated by separation of the void (or dimple rupture) during plastic straining, the nucleated fracture surface propagates zig-zag fashion from void to void until all the voids (formed around the fracture nuclei) impinge on one another

The general fracture appearance under the electron microscope has a dimple surface, which is produced by the ductile fracture propagation under the condition of microvoid coalescence.

It is noted that, the above considerations refer basically to MVC in the conventional tensile test specimens. However, it is unclear whether they can be referred to MVC induced by hydrogen embrittlement.

In addition, Thompson and Bernstein have shown that cleavage and quasicleavage fractures occurs preferentially in quenched and tempered martensitic 1045 steel as well as in pearlitic 1045 steel, which have much higher yield strength than spheroidized 1045 steel.

Fig. 15 provides a summary of hydrogen-induced cracking processes associated with the material microstructures like inclusions, grain boundaries, lattice, as well as voids and pores which are believed to influence the fracture mode of the failed components. It is recognized that the roadmap

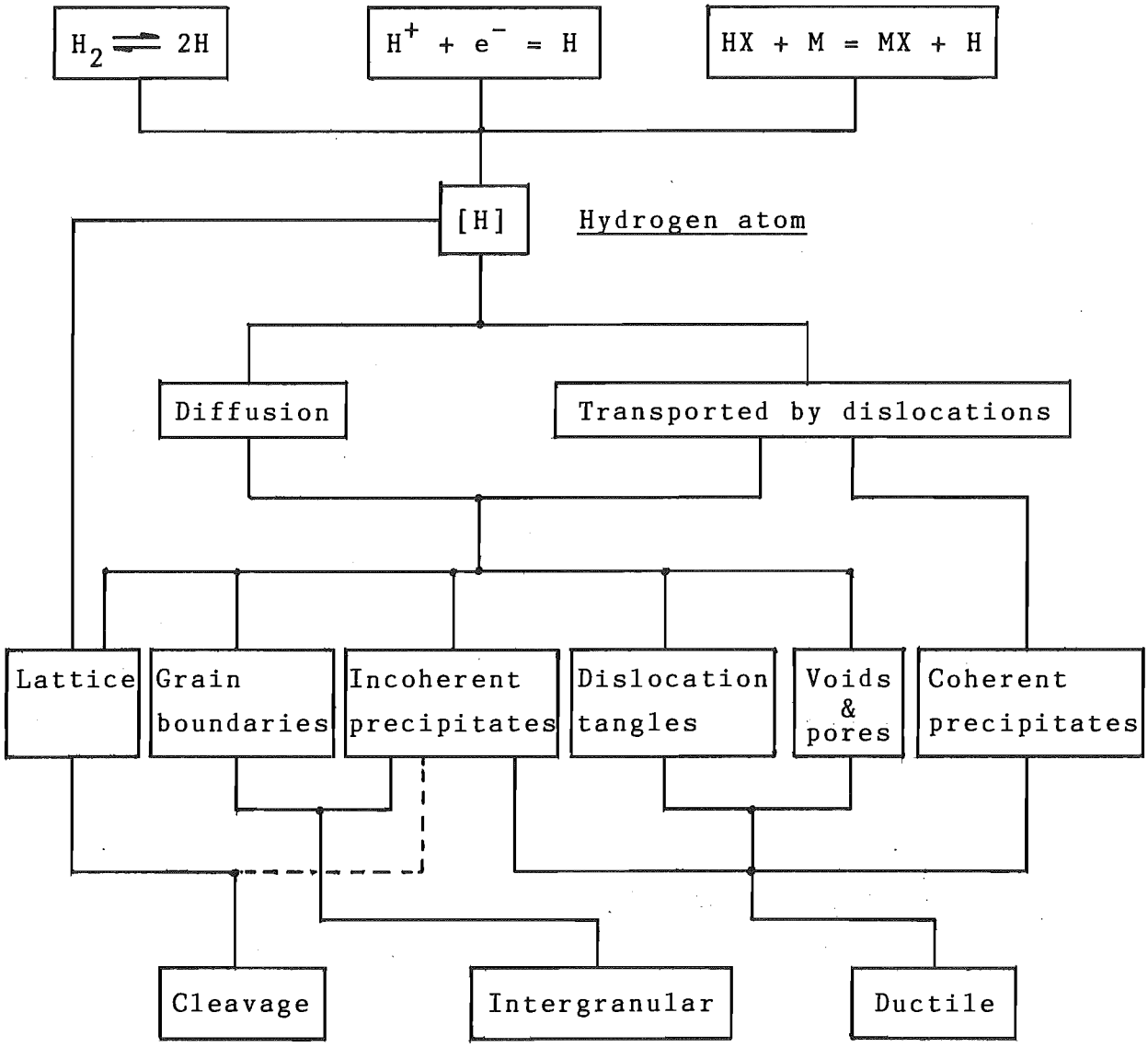

Remark : Dashed line refers to cleavage in hydrides.

Fig. 15[72]: A quantitative model for hydrogen-induced cracking associated with material microstructure.

in Fig. 15 has been made omitting the fracture process. Indeed, the design of the block diagram should include the crack initiation and the subcritical crack propagation steps which indicate how they give rise to the different fracture modes. However, in designing such a detailed roadmap, a considerable amount of experimental work needs to be done first, before an adequate model can be presented.

As we can see in the schematic illustration, hydrogen atoms are transported by diffusion or via mobile dislocations leading to accumulation at various microstructural phases, and the final fracture mode is dominated by the particular microstructures.

The interaction of hydrogen with dislocations in iron and steel has been studied by many researchers. Recently Hong and Lee[58] have shown that the interstitial hydrogen atom increases dislocation mobility, and it is believed that hydrogen is trapped in the stress field around dislocations and promotes the nucleation rate of kinks by lowering the difference in activation energy of formation between dislocation and kinks. However, it is generally agreed that interstitial atoms decrease the dislocation mobility because they act as pinning points for kinks and hinder the side motion of kinks. To explain this apparent contradiction, Hong and Lee have proposed that it will be necessary to investigate the rapid transport of hydrogen atoms by dislocations into the interior of steels in greater detail. On the other hand, it is believed that the nucleation of dislocations could be facilitated by dissolved hydrogen at the tip of a crack as well as by adsorbed hydrogen, and both of these interactions would reduce the (shear) strength of interatomic bonds of the solid solution. In reviewing the current arguments concerning the subject, a recent diffusion/dislocation-nucleation theory established by Hirose and Mura[68] is detailed in section 1.5.

Recently, Onyewuenyi and Hirth[73] have investigated

the effects of hydrogen on notch ductility and fracture in spheroidized AISI 1090 steel (Yield strength: 320 MPa). In the light of their investigations, they have indicated that the fractographic features of fractured hydrogen charged specimens are a mix of dimples and quasicleavage. This is evidence that the fracture process of AISI 1090 steel charged with hydrogen may involve an extensive localized plastic flow during crack propagation.

Cleavage and quasicleavage fractures are found to occur in quenched and tempered high-strength steels. In general cleavage fracture may have macro scale flat facets and quasi-cleavage fracture may exhibit macro scale ridges (Figs 14b and 14c).

Kikuta and Araki[74] have indicated that in hydrogen-assisted cracking of high strength steel HT-80 formation of transgranular cracks was often observed with subcracks along the boundary of martensite lath and were crystallographic, forming on variants of [110] planes. In addition, they have pointed out that the occurrence of quasicleavage fracture of hydrogen embrittlement has the following features: QC of hydrogen embrittlement is related to hydrogen diffusion under the applied stress condition. It is noted that hydrogen first diffuses towards dislocations on slip planes in martensite lath in the heat affected zone (i.e., HAZ of a weld) under a relatively low stress level. From the experimental results, Kikuta and Araki[74] have concluded that a certain time delay (also known as an incubation period) is required before fracture occurs; QC may be initiated from a region of the highest hydrogen concentration which is normally located on the highest dislocation densities on slip planes in lath. Apparently, Kikuta and Araki suggested hydrogen embrittlement in high strength steel is considered to be slip-plane decohesion.

Kikuta and Araki[74] have also pointed out that exami-

nation of fracture surfaces by electron microscopy has shown striation-like or ripple patterns. The formation of these striations is found to be due to collapse of slip planes associated with the localized plastic deformation without the void formation as shown in Fig. 14a for the case of MVC.

These striations are formed because materials deform plastically not only on the slip plane but also on the cross-slip plane within the individual laths. Therefore, Kikuta and Araki have proposed that the fracture appearance be named quasicleavage fracture of hydrogen embrittlement (QC_{HE}).

Referring to the intergranular fracture of hydrogen embrittlement, the most commonly observed failures of this type are associated with the environmental attack of a secondary metallic phase or element segregated to or precipitated at the grain boundaries.

The recent SCC study by Yoshino and Ikegaya[45] of martensitic stainless steels in chloride and sulphide environments provides further support for $Cr_{23}C_6$ carbide particles and the retained austenite at the grain boundary promoting intergranular SCC in corrosive environments. Their observations suggest that the single tempered martensitic stainless steels containing $Cr_{23}C_6$ carbide particles and retained austenite at grain boundary are sensitive to intergranular cracking (IG_{HE}).

It is thought that the retained austenite at the grain boundary attracts hydrogen atoms because of its greater solubility. The hydrogen atoms interact with dislocations generated by incompatible deformation of the two phases, thereby resulting in the formation of cracks. If it is transformed into martensite, it provides a preferential path for crack propagation.

A further feature of the hydrogen embrittlement of

steels with intergranular fracture mode was presented by Inoue and co-workers.[75] Their studies examined the response of quenched and tempered low alloy steels and a plain carbon steel with 600-800 MPa tensile strength to cathodic hydrogen charging in 3% NaCl aqueous solution with a current density of 2650 A/m^2.

With regard to the SCC behaviour observed in their studies, it is concluded that, the fracture mode of low carbon Si-Mn steels varies preferentially with the strain rate. It was found that the maximun allowable phosphorous concentration at the grain boundaries for intergranular fracture not to occur is about 2 Wt % in the case of $\dot{\varepsilon} \simeq 10^{-4} S^{-1}$, whereas it is about 0.1 Wt % in the case of $\dot{\varepsilon} \simeq 10^{-5} S^{-1}$. Inoue and co-workers have also indicated that the low carbon Si-Mn steels with fine precipitates of boron and nitrogen along the grain boundaries may enhance intergranular hydrogen embrittlement.

Recently, Bandyopadhyay and co-workers[33] have concluded that the intergranular stress corrosion cracking of 4340 steels in H_2 gas is due to a combination of impurity elements segregated during heat treatment, and hydrogen concentrated by the lattice expansion due to hydrostatic tensile stresses: Increasing the concentrations of Mn and Si, would promote the segregation of P and S to the prior austenite grain boundaries and reduce K_{Iscc} values.

On the other hand, the observations of Thompson and Bernstein[72] have indicated that cleavage and quasicleavage fractures occur preferentially in quenched and tempered martensitic plain carbon steel (e.g. AISI 1045).

Referring to the intergranular fracture of hydrogen embrittlement in high strength steel, Kikuta and Araki[74] have reported that intergranular fracture is dominant with a medium and lower constant applied stress within the stress

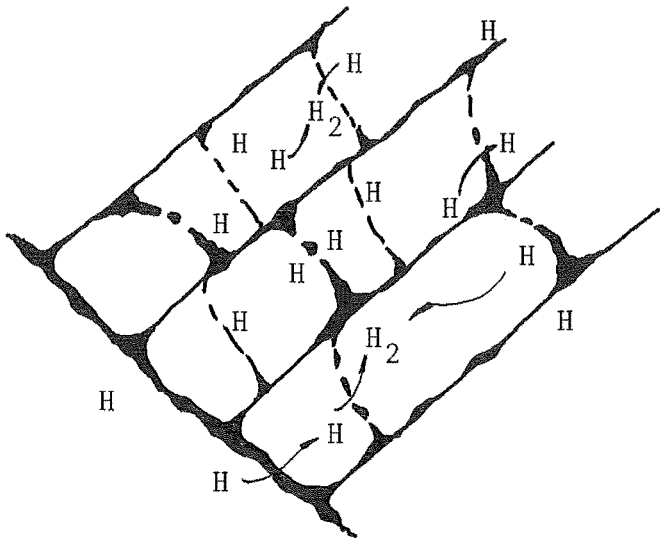

Fig. 16a) : Quasicleavage fracture of hydrogen embrittlement (QC_{HE}).

H : Hydrogen atom

: Bird crack or crack embryo.

Grain boundary

: Slip plane [110] or [112].

: Crack path.

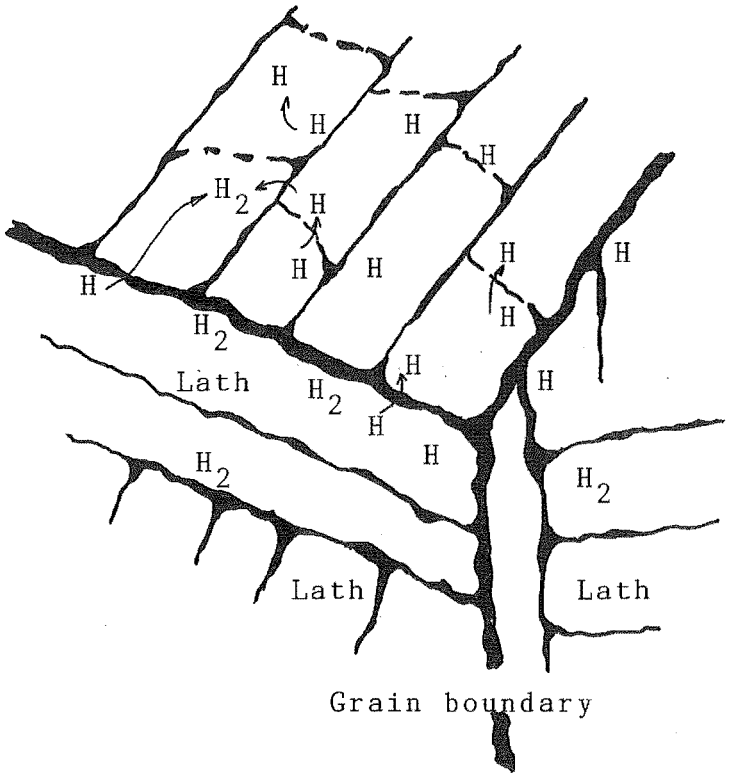

Fig. 16b) : Intergranular fracture of hydrogen embrittlement.

Fig. 16[74]: Schematic representation of fracture profile on hydrogen embrittlement.

range in which delayed fracture occurred.

Figs 16 and 17 show schematic key diagrams of the fracture profile observed in the electron microscope. The characteristic parallel tongue like patterns and microcracks between lath boundaries on the fracture surfaces are believed to result from the accumulated hydrogen at the lath boundaries, and it is based on assumption that the dislocation densities at the lath or grain boundary were estimated to be three orders of magnitude higher than interior values (i.e., the values inside the grain or lath). Consequently, the dissolved hydrogen atoms interact with the dislocations at the boundary, thereby resulting in the formation of microcracks along the grain or lath boundaries, this provides a preferential path for the intergranular crack extension as shown in Fig. 17.

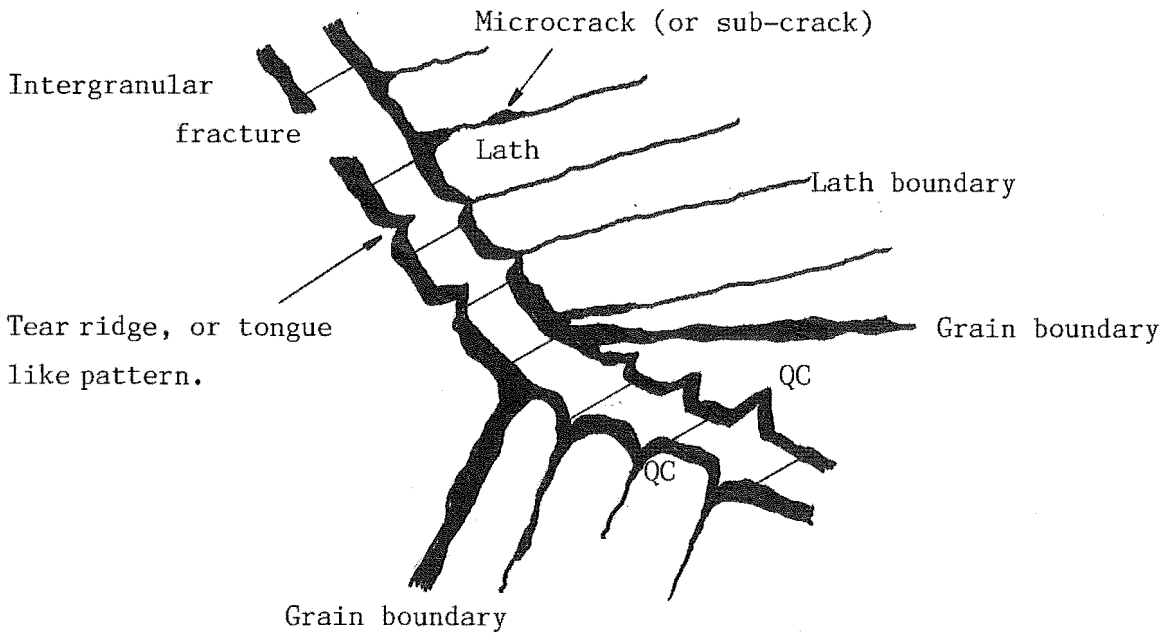

Fig. 17[74]: Schematic representation of fracture profile on intergranular fracture of hydrogen embrittlement.

It is noted that a similar fracture profile to that described in Figures 16 & 17 has also been observed in the present study (Sect. 4.1.1, Fig. 72). Unfortunately, the tongue like pattern (or tear ridge) does not appear very clearly on the grain surface in the fractograph, this is thought to be the result of the low magnification. It is believed that a high magnification fractograph (e.g., at 20,000 x) focused on a single austenite grain would give a clear picture for the tear ridge or tongue like pattern observation. However, it is important to appreciate that, in the author's experience, the fracture surface sometimes showed some corrosion products on it. The layer of corrosion products would make it difficult to determine the mechanics of fracture, too.

1.5 Plastic Flow At Crack Tips And Hydrogen-Assisted Cracking

Stress corrosion cracking of high strength steels in an aqueous solution environment is generally recognized as hydrogen-assisted cracking[9, 33, 48, 49, 68, 76].

A well-known model for hydrogen-assisted cracking (HAC) presented by Beachem[77] suggested that HAC crack tips advanced by microscopic plastic deformation processes, as shown in Fig. 18, that the deformation decreased gradually with the stress intensity factor, and that there were changes in fracture modes associated with the decrease in plasticity.

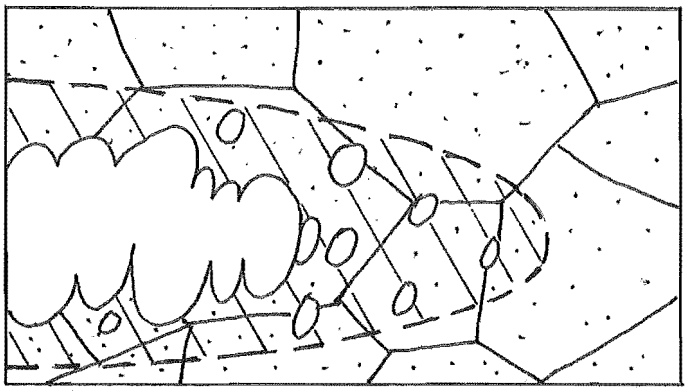

a): High stress intensity(K):- Fracture appearance: microvoid coalescence (MVC).

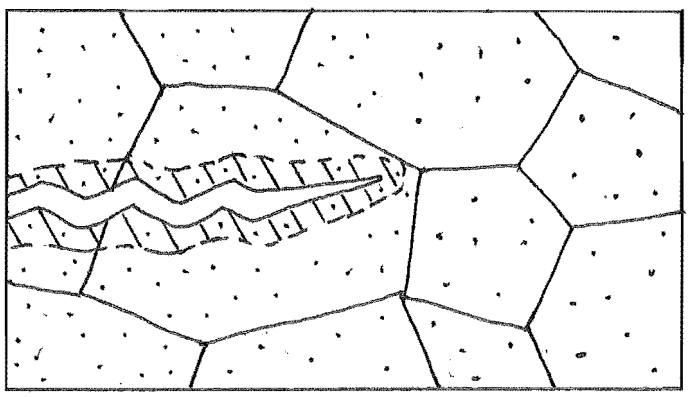

b): Intermediate stress intensity(K):- Fracture appearance: quasi-cleavage (QC).

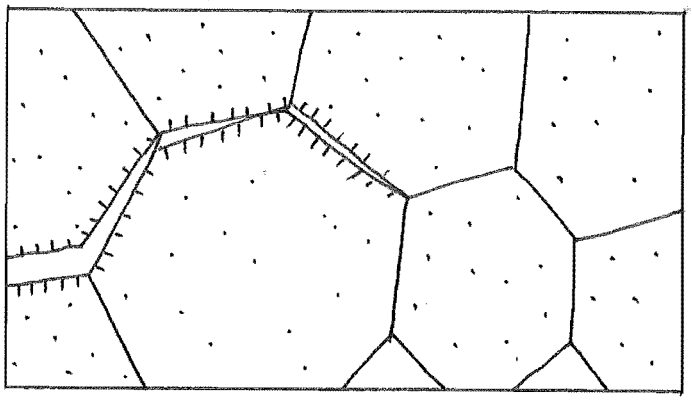

c): Low stress intensity(K):- Fracture appearance: intergranular cracks.

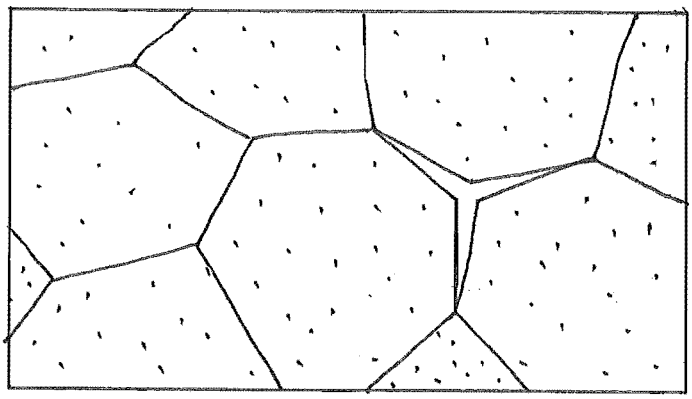

d): Intergranular cracking with an assist from hydrogen pressure.

Fig. 18(a-d): Sketches of microscopic fracture modes observed in Beachem's experiments.[77]

It is important to note that the above observations were collected from specimens of quenched-and-tempered alloys steels of the 4300 series[0.15% C and 0.28% C, yield strength (σ_{YS}) after heat treatment: 1186 MPa for 0.15C-Steel and 1345 MPa(relatively high strength) for 0.28C-Steel] tested in 3.5% NaCl solution and hydrogen gas. Wedge-loaded specimens were used in the investigation, and the overall fracture appearance for both steels are shown in Fig. 19(a to d).

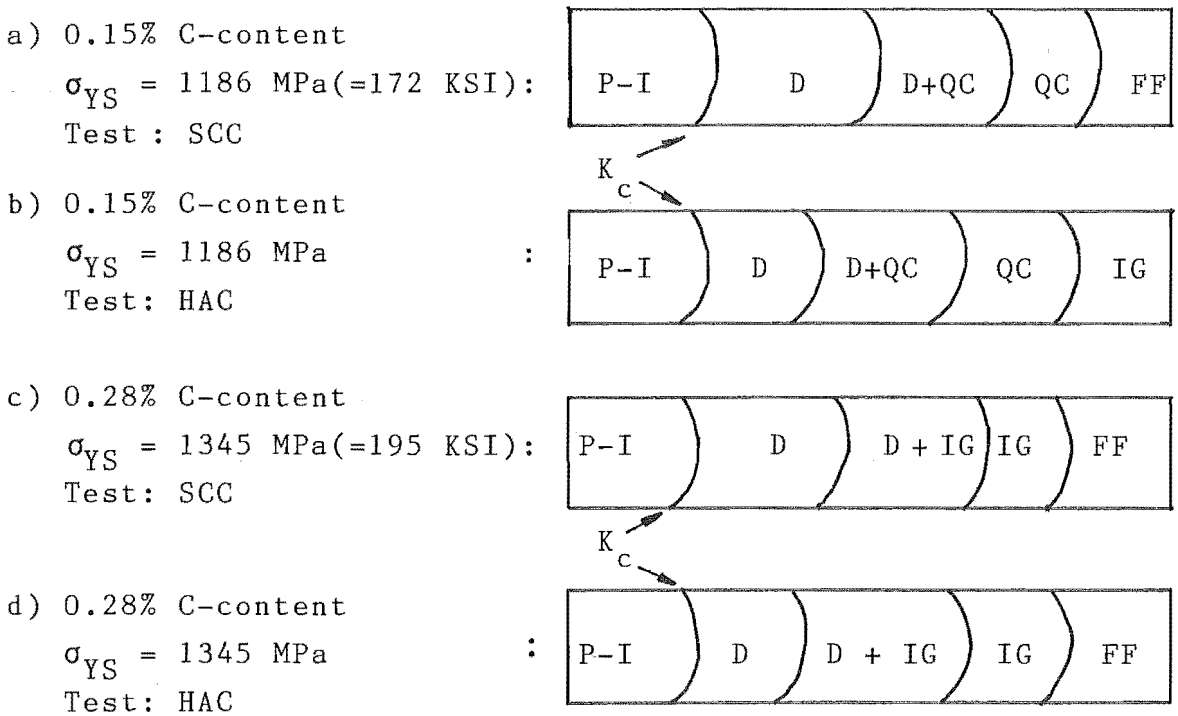

Fig. 19 : Schematics of fracture surfaces obtained from two steels(0.15% C and 0.28% C) tested under SCC and HAC-conditions. P-I = Pop-In crack, D = Dimples (see also Fig. 18a), QC = Quasi-Cleavage, IG = Intergranular Cracks (see also Fig. 18c), FF = Fast Fracture.(77)

Regarding the values of K in the above sketches at the ends of the Pop-in cracks, it is assumed that pop-in cracks stopped growing when the stress intensity factor (K) is equal to K_c.

In the light of Beachem's observations, it is clear that the stress corrosion cracking of high strength steel (e.g. : 0.28% C-steel of 1345 MPa yield strength) has identical fracture appearance with those HAC specimens of the same material (see Figs 19c & 19d). The results suggest that SCC of high strength steel must be hydrogen-assisted cracking.

The series of sketches in Fig. 18 show the tips of cracks growing under four different K conditions with the stress intensity factor decreasing from a) to d), and supports

a suggested explanation of the fracture behaviour at the tip of a crack. According to linear elastic fracture mechanics, the radius of the plastic zone at the tip of a crack is directly proportional to K^2 (Sect. 1.2.2) if the yield strength is constant.

As we can see in the sketches, the plastic zone of lower stress intensity has a longer and sharper crack length. Large numbers of microvoid coalescences can be observed in the fracture mode of high K conditions. This indicates that blunting at the crack tip is increased by increasing the stress intensity at the crack tip.

Referring to the relationship between plastic flow at crack tips and hydrogen-assisted cracking in steels, Lynch[78] has shown a general atomic mechanism of crack growth. The characteristics of stress corrosion crack propagation in high strength steel (D6ac Steel) are expressed on a microscopic scale. Remarkable differences between the tensile overload fracture in air (or inert gas) and hydrogen embrittlement in mercury were observed in Lynch's investigations. Fig. 20 summarizes the general features of the mechanisms involved. The relevant microscopic plasticity zone, in the form of dimples in the microvoid coalescence fracture mode developed in air or inert gas, and in the form of numerous shallow tear ridges in the intergranular or transgranular fracture modes developed by hydrogen-assisted cracking in mercury and hydrogen environment are demonstrated in the sketches.

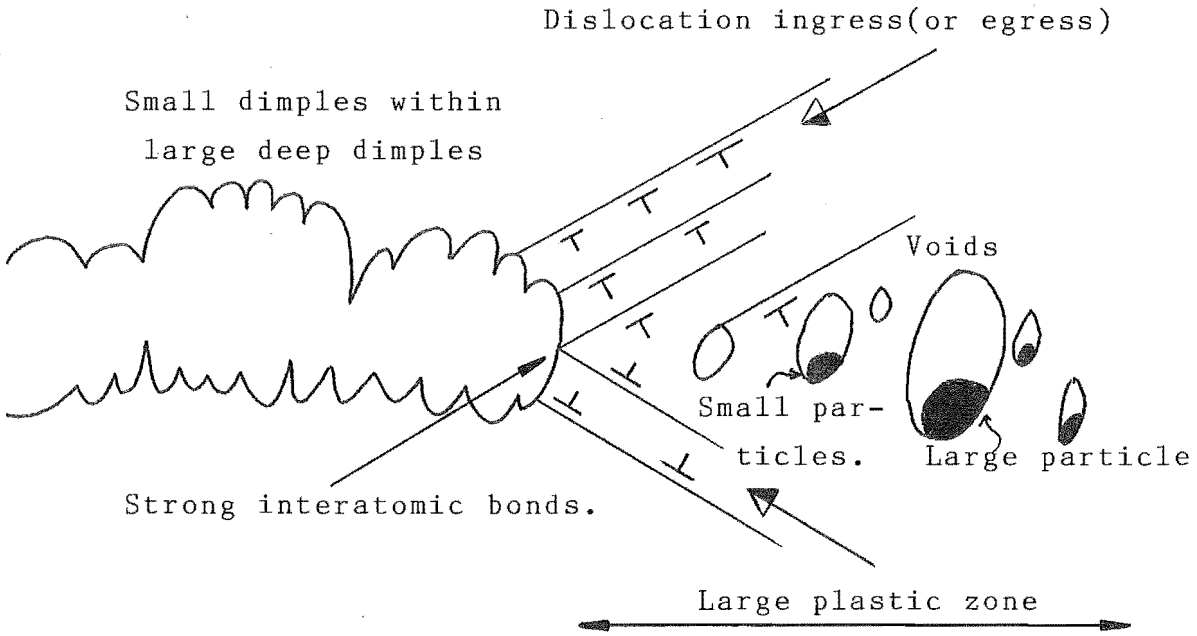

a) : Inert or air environment

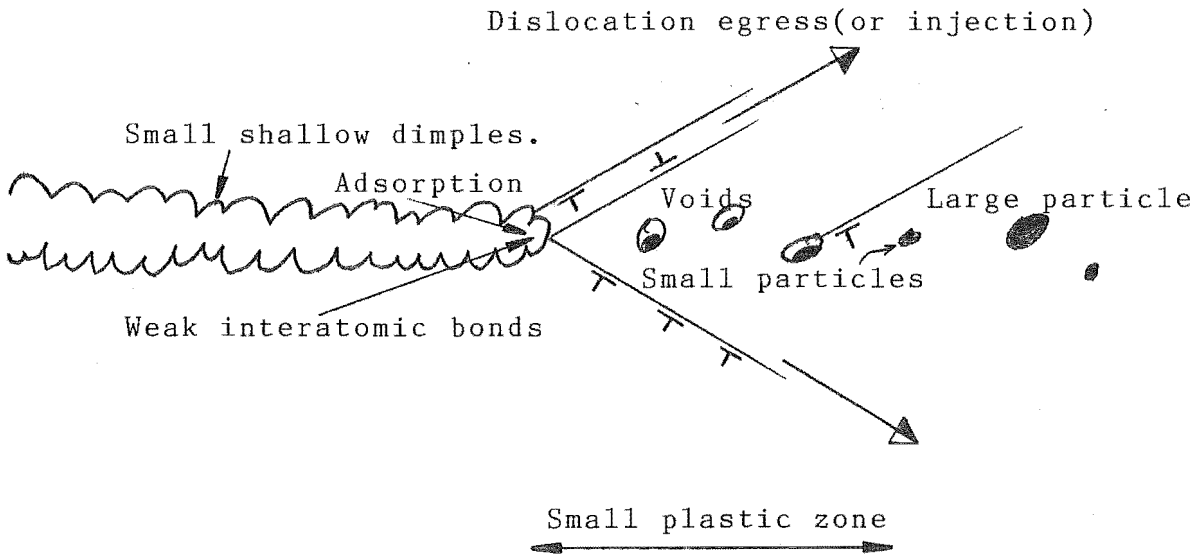

b) : Mercury or hydrogen environment

Fig. 20[78]: Schematic diagrams illustrating the mechanisms of crack growth by microvoid coalescence in a) inert, and b) embrittling environments.

As we can see in the sketch (Fig. 20a), the large dimples produced in air or inert gas environment are associated with the nucleation and growth of voids ahead of crack tips and the subsequent coalescence of voids with one another. It is generally agreed that voids initiate and grow preferentially around the large particles and coalescence of large voids with the crack tip involves coalescence with small voids nucleated from small particles between the crack tip and large voids. In view of these interactions, therefore, small dimples within large dimples are produced on the ductile crack surfaces.

On an atomic scale, Lynch[78] has suggested two factors, which concern the dislocation activity in the plastic region. Firstly, he proposed that most dislocations would either egress behind the crack tip or remain ahead of cracks to give the crack tip blunting and high strain ahead of ductile cracks which is demonstrated in Fig. 20a. Secondly , in air (or oxygen) environments, oxygen adsorbs strongly and produces disruption of the surface lattice with the incorporation of oxygen atoms into the topmost layer of the substrate atoms. The strong iron-oxygen bonds are probably present at crack tips. In inert gas, the topmost layer of surface atoms at crack tips is contracted towards the bulk, this is probably due to the fact that surface atoms have fewer neighbours than bulk atoms, and surface interatomic bonds are therefore stronger than those in the bulk. Strong surface interatomic bonds would probably not influence dislocation egress at crack tips significantly, however, the stronger interatomic bonds would make dislocation nucleation from crack tips difficult.

Referring to the effects of hydrogen ahead of crack tips, Beachem[77] has proposed that dissolved hydrogen facilitates dislocation activity in the plastic region ahead of cracks so that fracture by localised plastic flow occurs more easily. In atomic terms, this implies that adsorbed hydrogen would reduce the cohesive strength of the inter-

atomic bonds at the crack tip so that decohesion or nucleation of dislocations is facilitated. From the considerations of the relationship between dislocation nucleation and hydrogen embrittlement, Tien[79] believed that hydrogen atoms may be transported by dislocations into the metal matrix during the process. Dislocation transport of hydrogen to voids ahead of cracks could generate high pressures within voids which promote void growth. Under these conditions, the growth of the internal crack (Fig. 20b) would be promoted,and the hydrogen quantity accumulated in the plastic region would dominate the crack propagation rate.

The recent publication of Hirose and Mura[68] reported that the hydrogen quantity dissolved in the plastic zone ahead of a crack tip or a notch root is associated with Fick's law of diffusion under the stress condition. Based on the assumption that dislocations with the opposite sign are distributed in and ahead of a crack tip (Fig. 21), and the center of the distribution is the stress free surface, Hirose and Mura have indicated that the stress components along the dislocation array are given as:

$$\sigma^{D}_{xx} = \frac{2\cdot(\tau - k)\cdot x}{(a^2 - x^2)} \qquad 1)$$

$$\sigma^{D}_{yy} = 0 \quad \text{(stress free surface)} \qquad 2)$$

$$\sigma^{D}_{zz} = \frac{2\cdot \nu\cdot(\tau - k)\cdot x}{(a^2 - x^2)} \qquad 3)$$

and

$$P = -\frac{2}{3}\cdot(1 + \nu)\cdot(\tau - k)\cdot \frac{x}{(a^2 - x^2)} \qquad 4)$$

where σ^{D}_{xx}, σ^{D}_{yy} and σ^{D}_{zz} are the principal stress which are determined from the dislocation stress, ν is the Poisson's ratio, τ is the shear stress for the dislocations, k is the dislocation motion resistance, a is the dislocation pile-up distance, and P is the hydrostatic pressure of the hydrogen along the dislocation array.

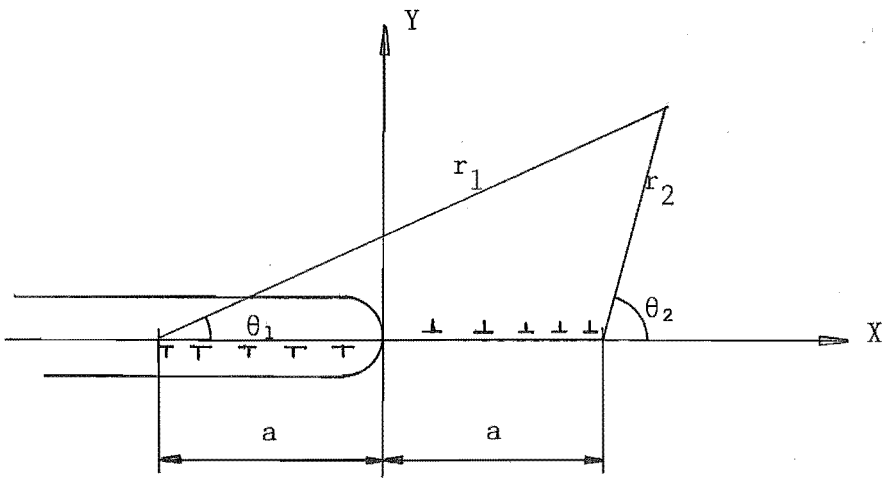

Fig. 21[68]: Dislocation model at the tip of a notch or a main crack.

The hydrogen diffusion is given by Fick's law as:

$$\frac{dC}{dt} = D \cdot \frac{d^2C}{dx^2} + \frac{A \cdot D}{K_b T} \frac{d}{dx} \left(C \cdot \frac{dP}{dx}\right) \qquad 5)$$

Where C is the hydrogen content at the tip of the dislocation array, D is the diffusion coefficient, A is the interaction constant between the dislocation and a solute atom, K_b is the Boltzman constant, and T is the absolute temperature.

An important point to the metallurgist or materials scientist is that when the accumulated hydrogen atoms reach a critical value (C_1), then the saturated region becomes an initial crack. More precisely, once a critical supersaturation of hydrogen atoms is achieved over a critical volume, then metal atom-atom rupture can occur by, for example, a reduction in atom-atom bond strength or accumulation of high local gas pressure associated with the recombination of hydrogen atoms which would be attributed to localized fracture growth or to a modification of the flow stress in front of the crack tip by the hydrogen concentration.

Assuming that d is the width of the saturated region, a is the length of a microcrack which initiates along the dislocation array, b is a function of the nucleation time t (Fig. 22), and the product $C_1 \cdot d$ presents the total number of accumulated hydrogen atoms(I) at the point of instability: Hirose and Mura have established a numerical solution for equation 5):-

$$I(b,t) = \frac{C_o \cdot D}{b} \cdot \tau \cdot \exp\left[\frac{1}{3} \cdot (1+\nu) \cdot (\tau - k) \cdot \frac{A}{K_b \cdot T} \cdot \frac{b/a}{\sqrt{1-(b/a)^2}}\right] \quad 6)$$

or $I(b,t) = C_1 \cdot d = C_1 \cdot (a-b)$ (The exact solution) 7)

where C_o is the hydrogen content at the initial state.

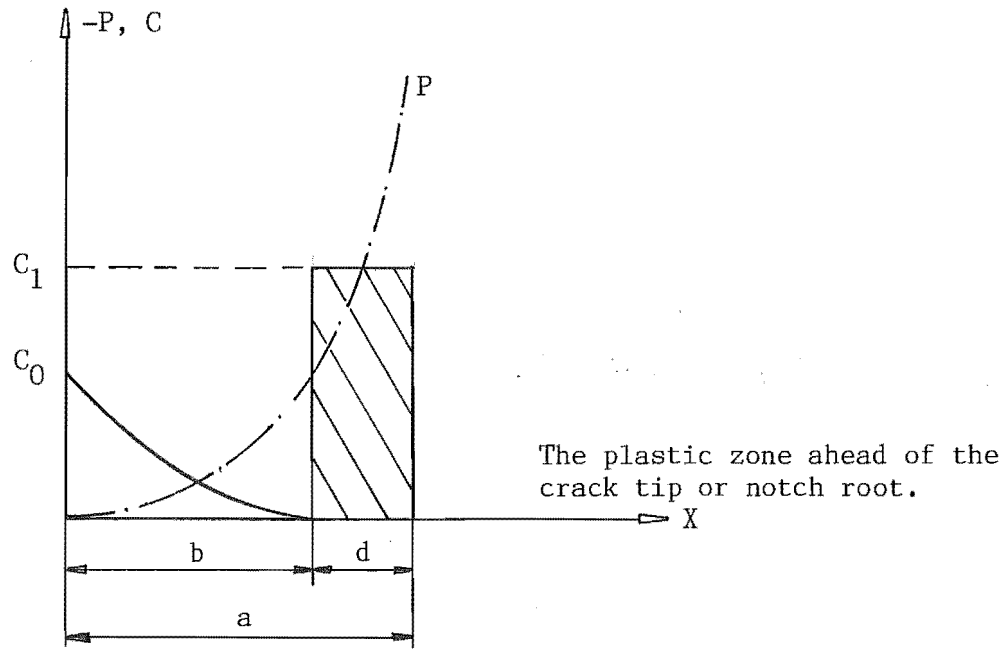

Fig. 22[68]: Model for hydrogen diffusion and hydrostatic stress distribution.

According to Lynch[78], it is noted that for the common martensitic high strength steels, the diffusion of hydrogen atoms at the carbide/matrix interfaces in the plastic zone ahead of crack tip would lower the strength of the interatomic bond at the tip of a crack, thereby facilitating the separation of the carbide/matrix interfaces by means of the local hydrogen pressure at saturated condition.

Based on the micromechanism that the crack advances step-wise by connecting the microcrack formed ahead of the main crack tip, and the hydrogen quantity dissolved in the plastic zone ahead of a main crack tip, an acceptable model for hydrogen-assisted cracking is illustrated in Fig. 23.

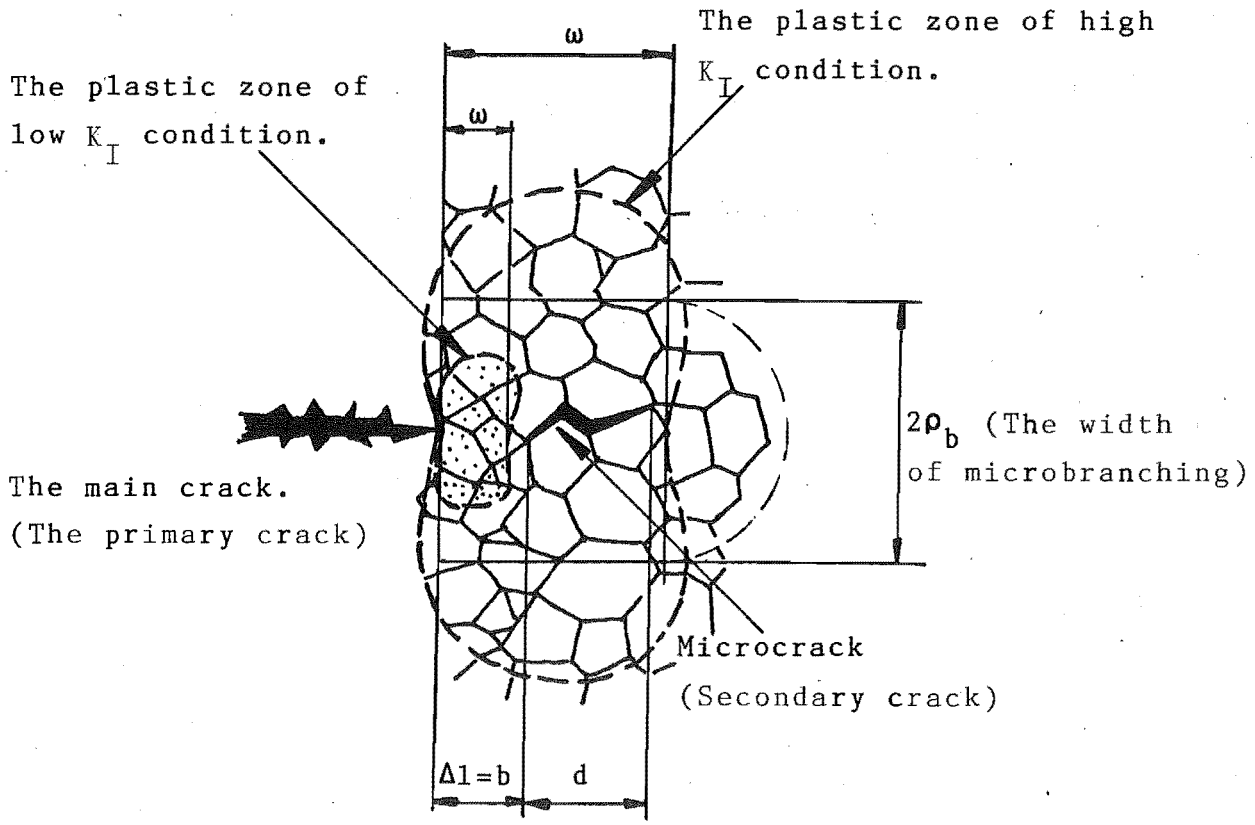

Fig. 23[68]: A sketch for stress corrosion crack growth.

It has been proposed that the existing microcrack along the prior austenite grain boundaries in or near the plastic region would link with the main crack if the mechanical instability condition is satisfied (For example: the accumulated hydrogen atoms reach saturation).

By comparing Fig. 22 and Fig. 23, we may discover that in Fig. 23:- d is the existing microcrack length, b=Δ1 is the average crack length increment between the main crack and the existing microcrack, and a=1 is the actual crack length after extension.

According to Hirose and Mura[68], it has been proposed that the plastic zone size ω may be defined as follow (Under plane stress or plane strain condition) :-

$$\omega = \frac{1}{3 \cdot \pi} \cdot \left(\frac{K}{\sigma_{YS}}\right)^2 \qquad 8)$$

Where K is the stress intensity at the main crack tip, σ_{YS} is the yield strength of the specimen, and E is the Young's Modulus.

It is noted that equation 8) is the current realistic expression concerning the estimation of the plastic zone size ahead of a crack tip for monotonic loading condition.

Note that, in order to facilitate calculation of the plastic zone size ahead of a crack tip for cyclic loading condition, the value of ω_{cy} is calculated by using the following formula.[9]

$$\omega_{cy} = \frac{1}{8 \cdot \pi} \cdot \left(\frac{K}{\sigma_{YS}}\right)^2 \cdot \frac{a_f}{c} \qquad 9)$$

Where:

a_f : pre-crack length

c : mean slot length in CT specimen

} See Figs 36 & 37.

For example, for the samples used in the present project the plastic zone size based on the different stress intensities

at the crack tip (Sect. 2.7.1), the expected initial bluntings for the stress corrosion crack propagation are listed below:

Table 4: Plastic zone size ahead of the crack tip
Remark: The samples are pre-cracked by cyclic loading condition.

c (mm)	a_f (mm)	ΔK ($MN/m^{3/2}$)	ω_{cy} (mm)	Remarks
8.3	11.25	33	0.025	$E = 2 \cdot 10^5$ ($\frac{MN}{m^2}$)
8.3	11.025	20	0.010	σ_{YS} = 1518 MPa
8.3	11.125	12	0.003	ΔK : Stress intensity at the fatigue crack tip.
8.3	11.375	4	0.0003	

It is clear that the plastic zone size is decreased drastically by decreasing the stress intensity at the crack tip. Such indications will help to rationalise differences in stress corrosion crack growth characteristics from the fracture interfaces at different ΔK values but for the same material/environment systems.

An implication from the plastic zone sizes in Teble 4 is that K_{Iscc} (threshold stress intensity factor) values may rise and the crack growth rate may decrease if the ΔK increases owing to significant initial blunting at the fatigue crack tips. It is for this reason that it is generally recommended that the maximum value of the stress intensity (ΔK) at the end of the pre-cracking procedure should always be less than the K_{Iscc} value. However it was not completely followed in the present thesis. This is due to the fact that, in the light of laboratory investigation, the blunting

at the fatigue tip dominates the value of K_{Iscc}, when the amount of transgranular fracture at the tips of pre-crack is significant (see Table 14). The value of K_{Iscc} is increased, when the fracture mode is from a principally transgranular crack to intergranular stress corrosion crack. The value of K_{Iscc} is decreased again, when the fracture mode is from a principally intergranular crack to intergranular stress corrosion crack. But the lowest K_{Iscc} was obtained with the lowest ΔK & entirely transgranular pre-crack (see section 4.2).

Referring to the relationship between the width of microbranching $2 \cdot \rho_b$ and the stress intensity factor K, Austen[17] has developed a realistic model describing the concept of an effective crack tip radius, ρ_c, to explain both the apparent stress intensity and the true stress intensity.

It is noted that, in the light of the present laboratory investigations, the effect of crack blunting due to microbranching seems not to be so significant as the change of fracture mode at the fracture interface (Sect. 4.2). In keeping with this view, therefore, the effect of branching and blunting of stress corrosion cracks are excluded from the discussion.

It is apparent in reviewing the current state of mechanistic understanding of stress corrosion cracking in high strength steels/in gaseous or aqueous environment systems that, although many questions remain unanswered, the basic requirements for hydrogen-assisted crack initiation and propagation are well understood.

In reviewing such a wide subject as the mechanisms of stress corrosion cracking in high strength steels, it is obvious that generalizations have to be made. In this thesis, attention was focused especially on the high strength steels/ in gaseous or aqueous environment systems. Within these

bounds, therefore, the results of various SCC tests of similar materials/environment systems from several workers are reviewed. The results may provide more empirical data for the conclusion that SCC of high strength steels in a corrosive environment is hydrogen-assisted cracking.

Study 1[9]: Factors influencing stress corrosion cracking in high strength steel.

Material: AISI 4340-steel.
Heat treatment: Austenised at 850° C, Oil quenched, Tempered at 320° C for 1 hour. It is noted that this procedure is comparable to the present laboratory heat treatment process.
Chemical composition: similar to ULTIMO-200 steel.
Yield strength: not determined.
Hardness : 527 VPN.
Corrosive environment: H_2S (gas).
Results:

Table 5: Dependence of threshold stress intensity for cracking in H_2S on nature of fatigue pre-crack in 4340-steel.

Test series No.	Pre-cracking environment	Final ΔK	Nature of fatigue crack at transition	Threshold stress intensity
		($MN/m^{3/2}$)		($MN/m^{3/2}$)
I	Air	6.5	About 50% intergranular	10.4
II	Air	3.2	Very little intergranular	13.3
III	Vacuum	3.2	No intergranular	16.7

Comments:

1) Measurements of the threshold stress intensity (K_{Iscc}) for hydrogen-assisted cracking in test series No. I, II, and III have indicated that the intergranular hydrogen embrittlement cracks would propagate more easily from an existing crack of similar nature (i.e., principally intergranular). Further support for this interpretation is also given by the test series No. 1 of Study 2 listed later.
2) Cowling[9] indicated that SCC in high strength steel is due to hydrogen embrittlement. Supporting evidence for the conclusion: similarity of results in NaCl solution and H_2S gas.

Study 2[68]: Growth mechanism of stress corrosion cracking in high strength steel.

Material: AISI 4340-steel.
Chemical composition: similar to ULTIMO-200 steel.
Corrosive environment: 0.1 N H_2SO_4 solution of the temperature at 289° K (similar to 3.5% NaCl, considered as a strong aqueous electrolyte, but a mild corrodent solution).

Results:

Table 6: Mechanical properties and heat treatments

Test series No.	Heat treatment	The main crack initiation stress intensity K_I (monotonic loading)	% Intergranular at transition (from the tip of the main crack to the detached crack)	Yield strength σ_{YS}	Threshold stress intensity (based on 240 h) K_{Iscc}
	850° C + 1 hr Oil quenched	[$MN/m^{3/2}$]		[MPa]	[$MN/m^{3/2}$]
1	200° C temp.	<21.7	about 100%	1530	9.3
2	400° C temp.	<31.0	about 100%	1330	18.6

Comments:

1) Fracture surface is entirely intergranular in Region II (stress corrosion crack region).
2) The value of K_{Iscc} in test series No. 1 is equal to 9.3 $MN/m^{3/2}$. The measurement is made on AISI 4340-steel at the yield strength of 1530 MPa in a heat treated condition similar to the ULTIMO-200 steel at the yield strength of 1518 MPa, which has been used in the present investigation. The result can be of central importance, as it tends to support an important point at the conclusion of the present thesis (Chap. 5), i.e.,:-
   Measurements of the threshold stress intensity (K_{Iscc}) for hydrogen-induced cracking in test series No. I, III, V, and VI of the present thesis are correct.
   It is noted that, the above conclusion is based on the fact that both steels (i.e., the 4340 steel and the ULTIMO-200 steel) have almost identical yield strength values, similar chemical composition and heat treatment.
3) Hirose and Mura[68] agreed that SCC of high strength steel in an aqueous solution environment is a hydrogen-assisted cracking.

Study 3[33]: Hydrogen-induced cracking in 4340-type steel: Effects of composition, yield strength, and H_2 pressure.

Materials: 4340-type steels.

Yield strength:

In the range 1140 MPa (165 KSI) to 1900 MPa (270 KSI).

Corrosive environment:

0.11 MPa H_2 at 23° C (296 K).

Results:

See Table 7, Fig. 24, and Fig. 25.

Table 7: Material list

Index	Description	Steel I.D.No.
1	840 modified 4340 steel	840
2	841 " " "	841
3	842 " " "	842
4	843 " " "	843
5	846 " " "	846
6	B2 commercial air melted 4340 steel	B2
7	B7 high purity NiCrMo-4340 steel	B7
8	B6 high purity with Mn+Si 4340 steel	B6

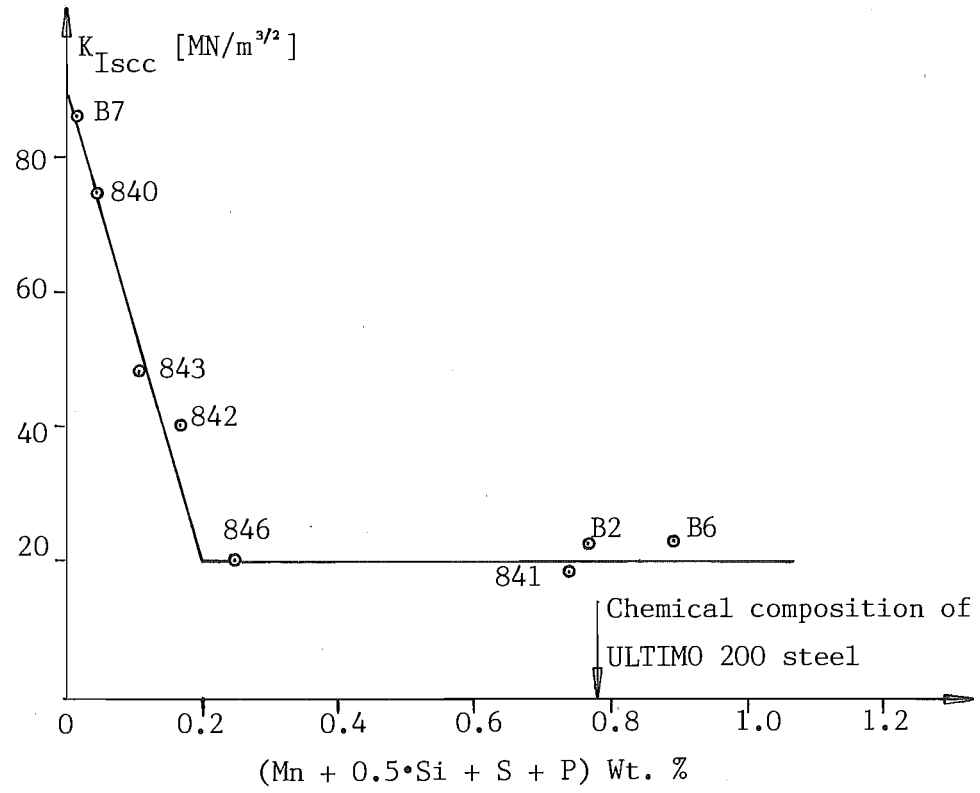

Fig. 24: Dependence of K_{Iscc} in 0.11 MPa H_2 at 296 K on composition parameter related to segregation tendency of S and P in 4340-type steels of constant yield strength (1450 MPa).

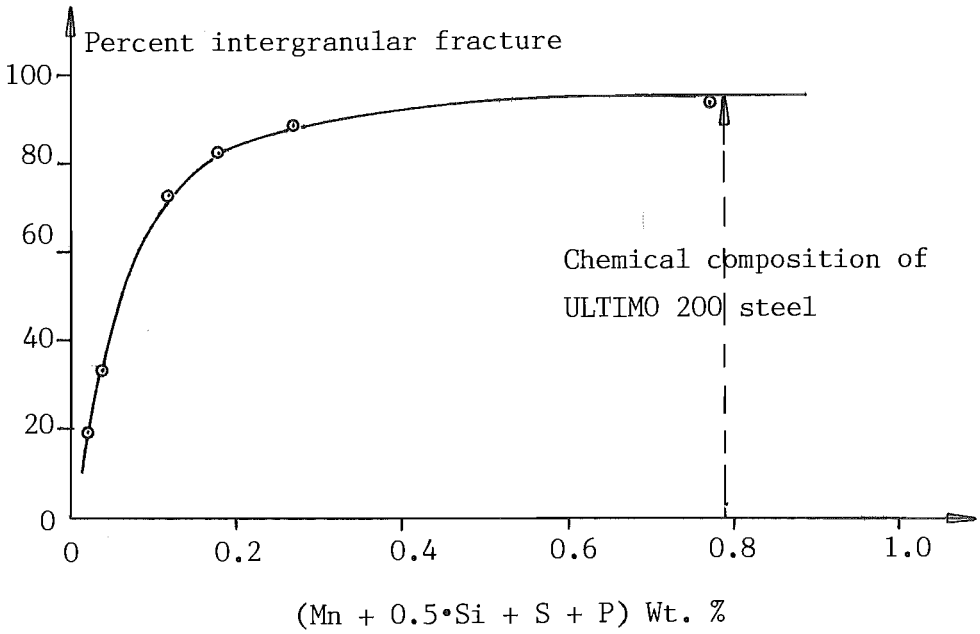

Fig. 25: The increase in percent intergranular fracture with the composition parameter in the specimen referred to in Fig. 24.

Comments:

1) Fig. 24 and 25 show that the susceptibility to hydrogen-induced cracking in high strength steels may vary with the alloying additions.
2) As the percentages of (Mn + 0.5 Si + S + P) are increased from 0.2% to ∿1.0%, the measured K_{Iscc} values are reduced to < 20 $MN/m^{3/2}$. In these circumstances, the threshold stress intensities tend to be independent of the bulk concentration of alloy additions. Moreover, the reduction in K_{Iscc} corresponds to an increase in the amount of intergranular fracture from ∿20% to almost 100%. This circumstantial evidence suggests that the susceptibility to hydrogen-induced cracking in high strength steel is related to the tendency for intergranular fracture in hydrogen from environmental sources (e.g. moisture, aqueous solution, H_2S gas etc.).

Study 4[67]: Crack paths and hydrogen-assisted crack growth response in AISI 4340 steel.

Heat treatment: Normalized, 1 h, at 1173 K; Air cooled and austenitized, 1 h, at 1116 K; Oil quenched; Tempered, 1 h, at 477 K; Air cooled.

Yield strength: 1344 MPa.

Corrosive environment: In H_2 (gas) and H_2S (gas) over a range of temperatures and pressures.

Results:

It has been suggested that the hydrogen embrittlement sequence can be divided into the following three cracking steps:-

1) The supply of hydrogen: This includes gas phase transport, surface reactions, and diffusion of atomic hydrogen into the embrittlement sites.
2) The partitioning of hydrogen among the potential fracture sites in the microstructure. These sites (i.e., the potential crack paths) in AISI 4340 steel includes: a) The prior-austenite grain boundaries, b) [110] and [112] planes through martensites, and c) The martensite lattice itself.
3) This step deals with the embrittlement reaction at each type of site, with the prior-austenite grain boundaries being most susceptible and the martensite lattice least susceptible to hydrogen embrittlement. However, it is noted that, for crack growth in hydrogen gas of 133 KPa (N.B., 1 std. atm. = 101 KPa) at low temperatures (e.g., 23° C or 295 K), the crack path followed predominantly along prior austenite grain boundaries, with a small amount of quasi-cleavage (QC) separation; For crack growth in hydrogen gas of 133 KPa at high temperatures (e.g., 139° C or 412 K), more hydrogen is expected to diffuse into the martensite lattice. Increasing amounts of microvoid coalescence (MVC) or dimple failure occur with increasing gas temperature.

1.6 Concluding Remarks

The principal conclusions of the literature review in sections 1.4 and 1.5 may be summarized as follows:

1) Stress corrosion cracking in high strength steel is due to hydrogen embrittlement. Supporting evidence for the conclusion: similarity of results for the specimens fractured in NaCl solution[9], H_2SO_4 solution[68], H_2S gas[9], and hydrogen gas.[9, 33, 67, 77]

2) Hydrogen-induced cracking in high strength steels follows predominantly along prior-austenite grain boundaries, with a small amount of quasi-cleavage, at low corrodent temperature.[67, 68, 74]

3) The threshold stress intensity (K_{Iscc}) value should decrease, with decreasing degrees of blunting at the crack tip by plastic strain/deformation.[9]

4) Adding the Mn and Si content in high strength steels promotes the segregation of P and S to the grain boundaries and encourages intergranular fracture along prior-austenite grain boundaries.[33]

2. EQUIPMENT DEVELOPMENT AND EXPERIMENTAL TECHNIQUES

2.1 Equipment Development

An important part of this project involved the development of stress corrosion testing equipment capable of performing repeatable tests on Compact Tension (CT) Specimens as shown in Figs 36 and 37. Fracture toughness (K_{IC}) test was made under plane strain conditions on fatigue pre-cracked compact tension specimens in accordance with ASTM standard E399.[8]

The design process was a time-consuming operation and a major part of the time spent on the project was invested in production of the testpiece grips for three existing experimental rigs. The designed test-piece grips and the components for calibration are shown in Figs 26-35.

A description of the design process cannot fully convey all the details which had to be encountered and solved in the development of the equipment. Three experimental rigs were available for development and are shown in Figs 38 and 39. The original design concept of stress corrosion rig No. 3 was modelled from Distington Engineering Company Limited of Workington in England, and was constructed in the University of Canterbury, mechanical engineering department some time ago. Since the machine is only 65 cm high, it was placed on a bench (Fig. 39). For the stress corrosion testing machines Nos 1 and 2 the original design concept was modelled from England, and was made by Mr. O. Bolt (senior technician of the department) under the supervision of Mr. Fahy (senior lecturer of the mechanical engineering department) in 1971.

Fig. 39 also shows that the CT specimen is surrounded by a corrosive solution of 3.5% NaCl in a plastic container. All the parts of the machine exposed to the corrosive medium are made of stainless steel. This is to protect the part

from suffering corrosion in the event of accidental spillage.

The existing experimental rigs had no tensile grips and the priorities of subsequent grip design were:-

(1) Design of loading clevis suitable for the existing experimental rig tension rods.
(2) Design of plastic container for the containment of the corrodent solution around the specimen.
(3) Design of sealing methods for the corrodent solution container around the test-piece.
(4) To ascertain that the existing magnetic stirrer pumping system is reliable.
(5) Design of calibration test-piece.

2.1.1 Loading Clevis

Taking into account the relatively small loads that the stress corrosion specimen required to fracture, it was decided that stainless steel (AISI 304) would provide sufficient strength and rigidity. An adaptor (Fig. 26: Pos 3 to 8) to connect the tension rods rigidly to the loading clevis was then required, and appropriate designs were made.

A loading clevis suitable for testing compact specimens is shown in Figs 31 and 32. Both ends of the specimen are held in such a clevis and loaded through pins (Fig. 30). In order to provide sufficient clearance between the loading pins (Fig. 30) and the clevis holes (Fig. 31), these holes are provided with 0.1 mm accuracy on manufacturing. Careful attention must also be given to achieving as good alignment as possible through careful machining of the adaptor bolts (Fig. 32).

On receipt of the loading clevis it was discovered that the complete assembly retained a large space between the lock nut and the loading clevis (Fig. 31). Since a large clear-

ance at this position would give a sealing problem, to prevent any corrodent leakage around the adaptor bolt, an aluminium plate of 1 mm thickness (Dimension: 80 mm x 110 mm) was added between the plastic container and the lock nut. This also provides a rigid support to the plastic solution container.

General Layout

Scale : 1 cm ≙ 1 cm

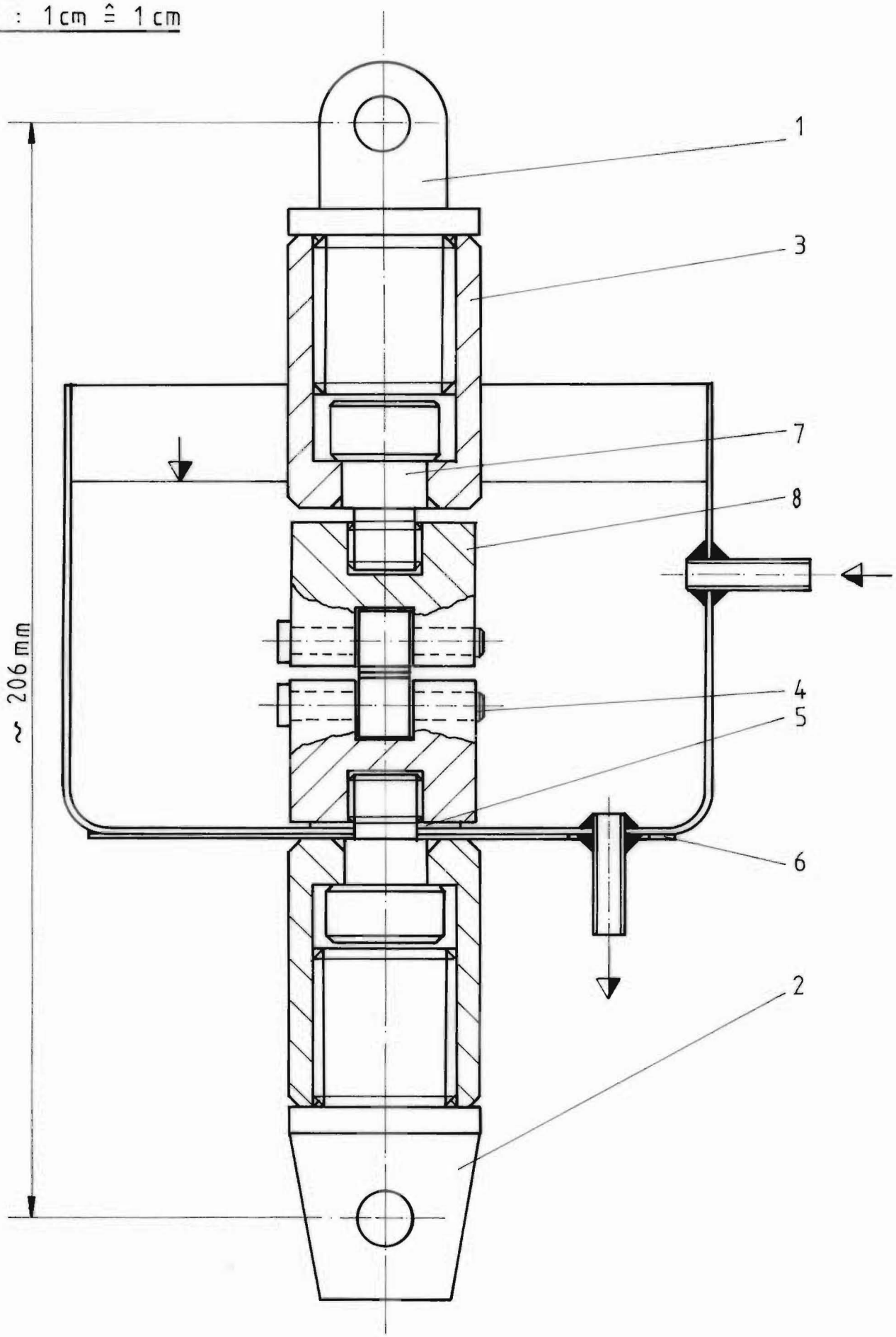

Fig. 26 Stress Corrosion Testing Rig No. 3

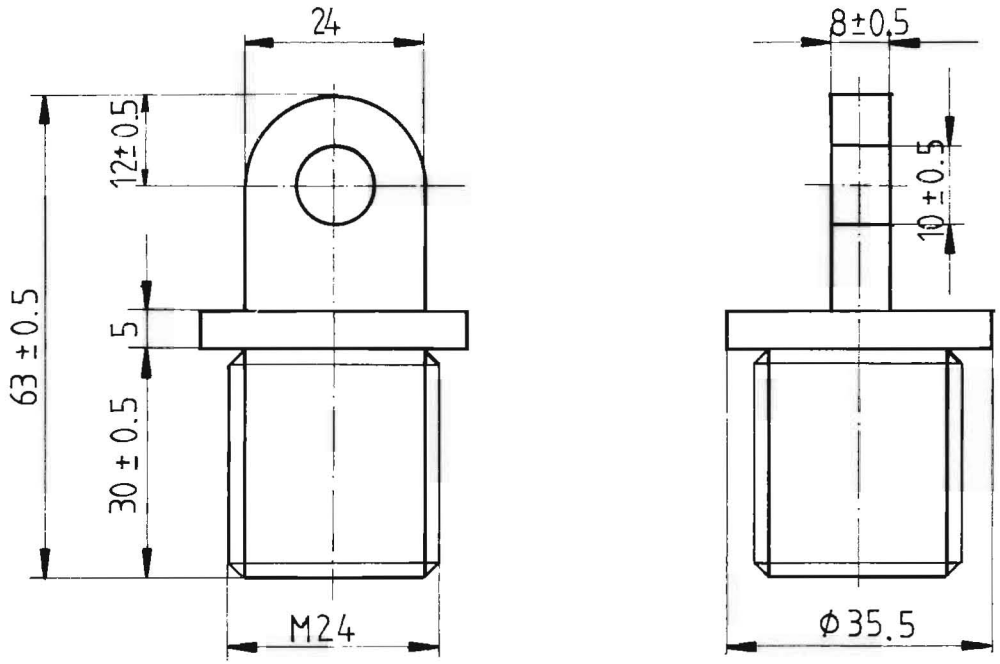

Position : 1

Fig. 27: Upper Tension Bolt

Scale : 1 cm ≙ 1 cm

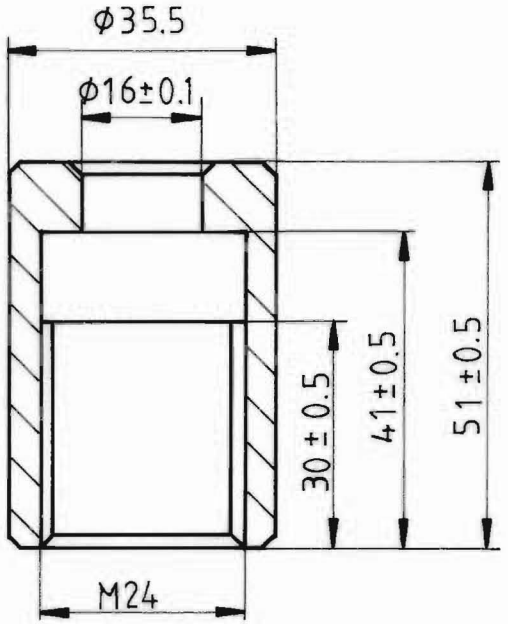

Position : 3

Fig. 28: Upper / Lower Lock N

Scale : 1 cm ≙ 1 cm

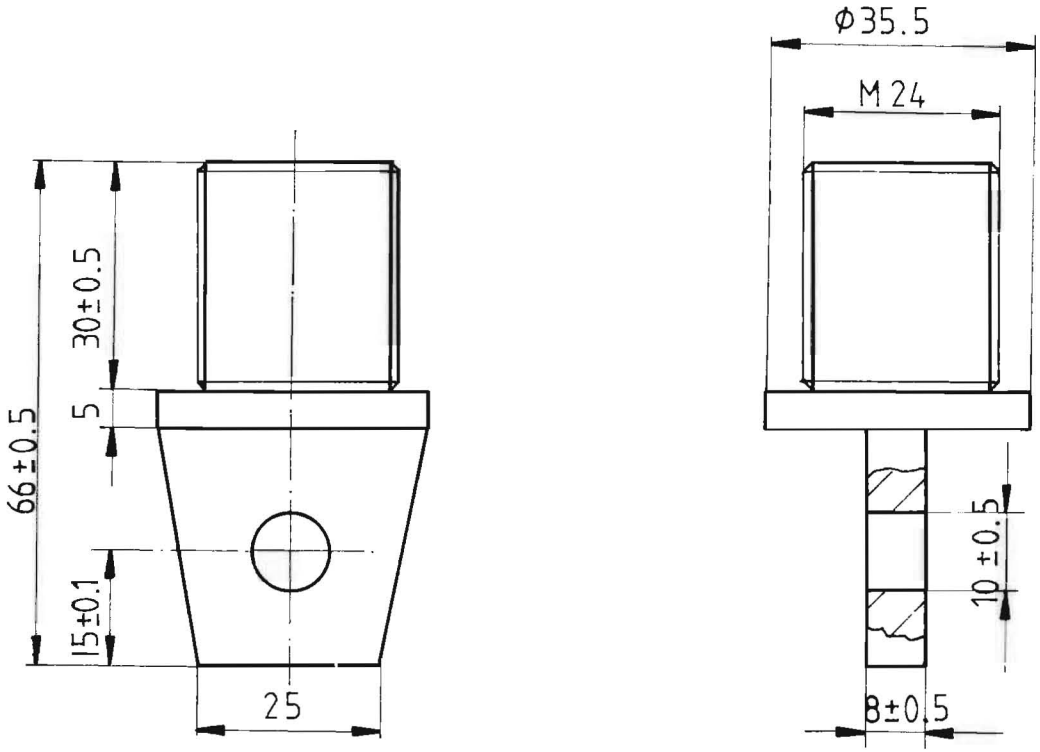

Position : 2

Fig.29: Lower Tension Bolt

Scale : 1 cm ≙ 1 cm

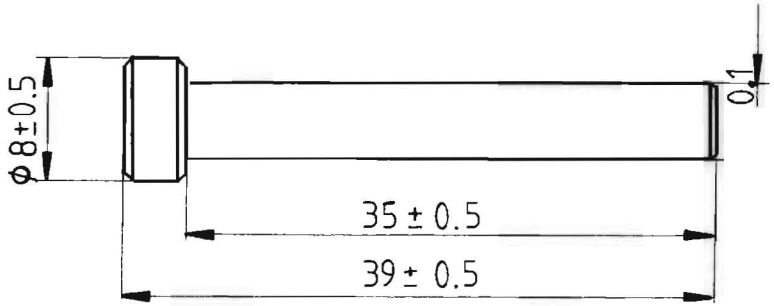

Position : 4

Fig. 30 Linking Pin

Scale : 2 cm ≙ 1 cm

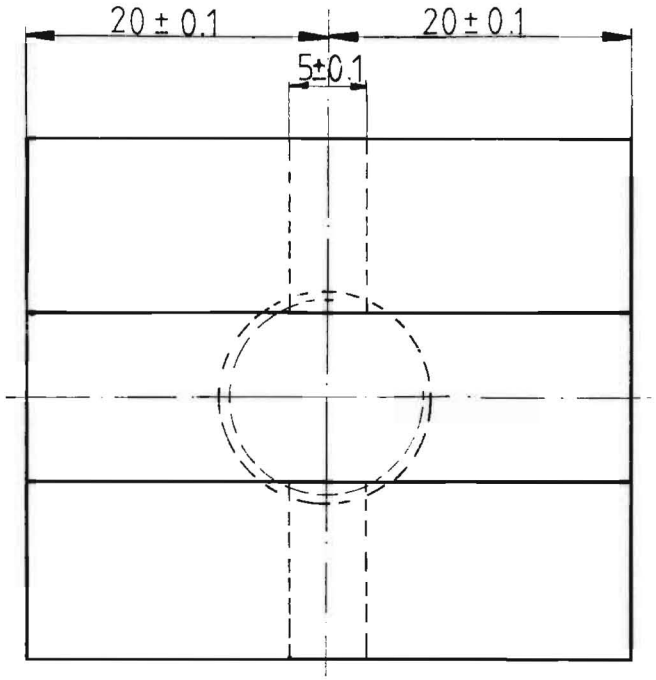

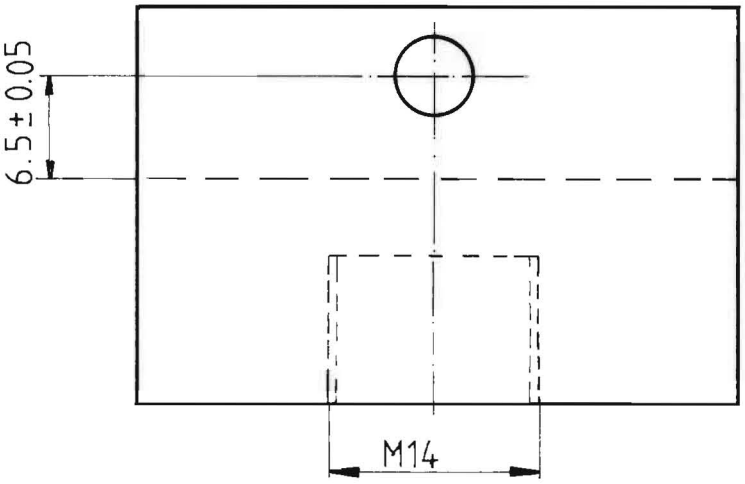

Position : 8

Fig. 31 : Loading Clevis

Scale : 2cm ≙ 1cm

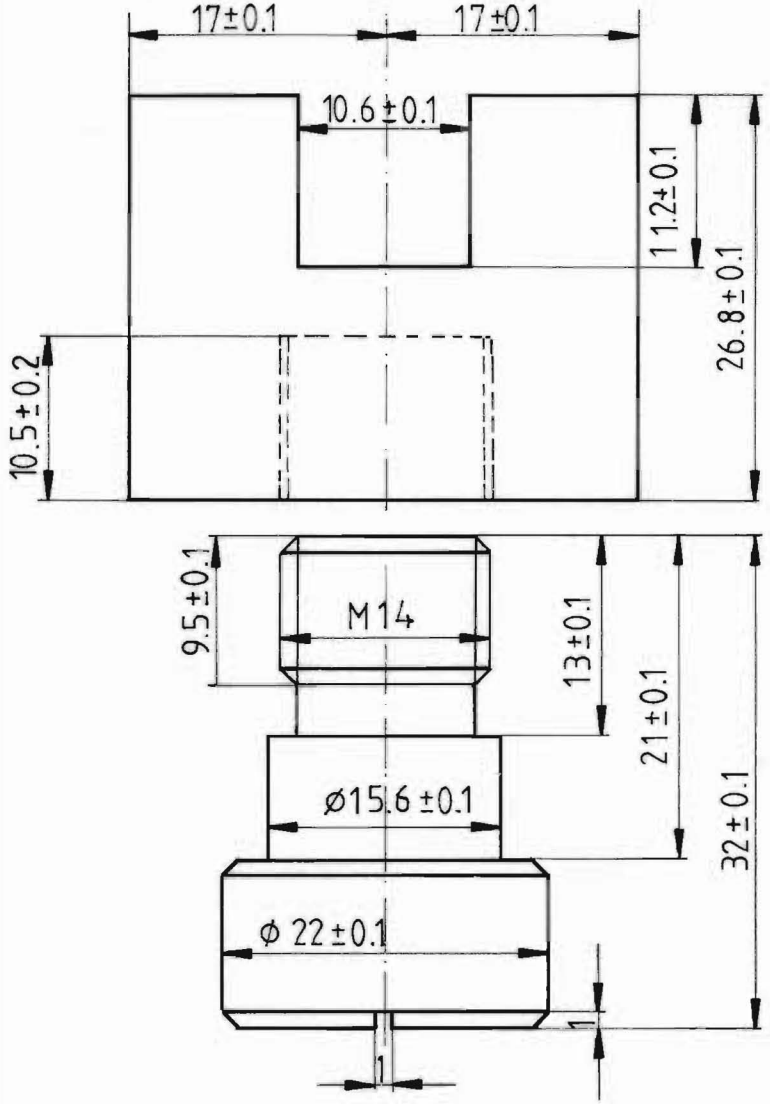

Position : 7

Fig.32 : Adaptor Bolt [Scale : 2 cm ≙ 1 cm]

CALIBRATION COMPONENTS [SCALE : 1 cm ≙ 1 cm]

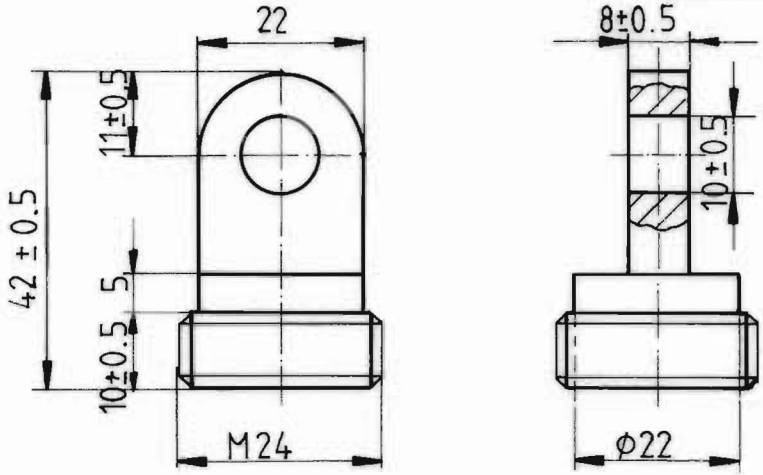

Position : 1

Fig. 33: Upper Calibration Bolt

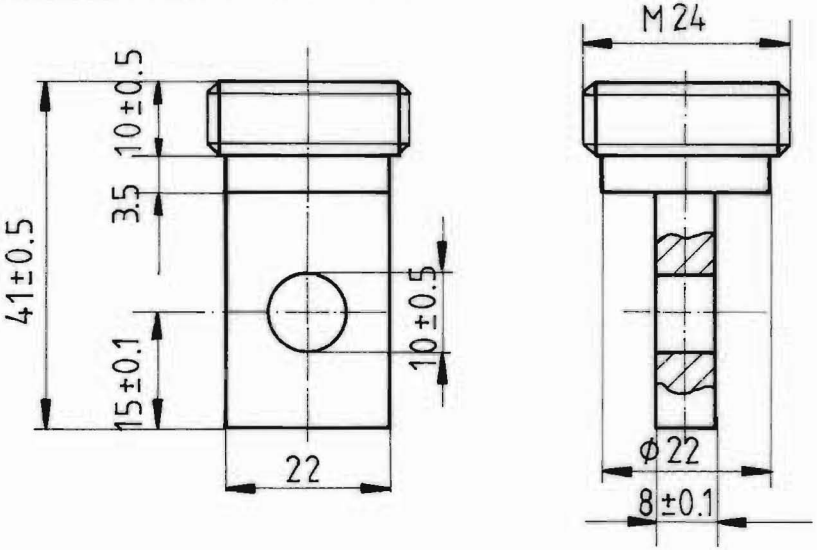

Position : 3

Fig. 34: Lower Calibration Bolt

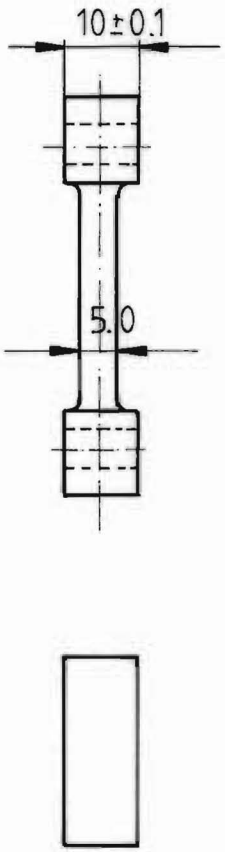

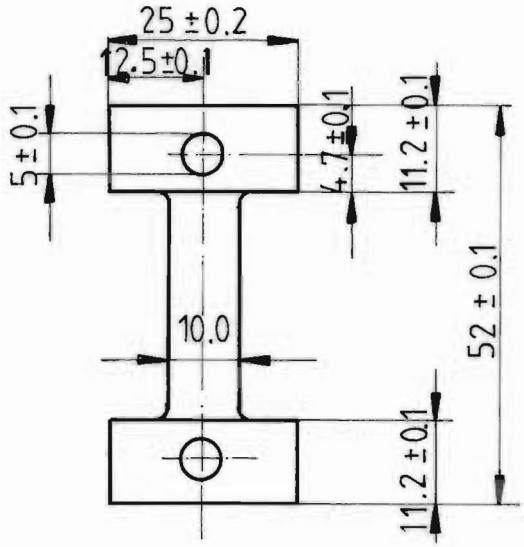

Fig. 35 : Calibration Test Piece

Table 8 : Materials list for the testing equipment

Position	Description	Material	Quantity	Remarks
1	Upper tension bolt	Low carbon steel, En 3	1	For testing rig No.3
2	Lower tension bolt	Low carbon steel, En 3	1	For testing rig No.3
3	Upper lock nut	Stainless steel, AISI 304	3	For each testing rig: 1 pcs
	Lower lock nut	Low carbon steel, En 3	1	For testing rig No.3
4	Linking pin	Stainless steel, AISI 304	8	For each rig: 2 pcs
5	Rubber washer (Dia.25 xDia.14 x 2 mm)	Rubber lining sheet of 2 mm thickness	3	For each rig: 1 pcs
6	Supporting plate (80 x 110 x 1 mm)	Aluminium plate of 1 mm thickness	3	For each rig: 1 pcs
7	Adaptor bolt	Stainless steel, AISI 304	6	For each rig: 2 pcs
8	Loading clevis	Stainless steel, AISI 304	6	For each rig: 2 pcs

Contd . . .

Table 8 :(Contd)

Materials list for calibration components

Position	Description	Material	Quantity	Remarks
1	Upper calibration bolt	Low carbon steel, En 3	1	For testing rig No. 3 only
2	Lower calibration bolt	Same as above	1	Same as above
Fig. 35	Calibration test-piece	Same as above	1	For all the rigs

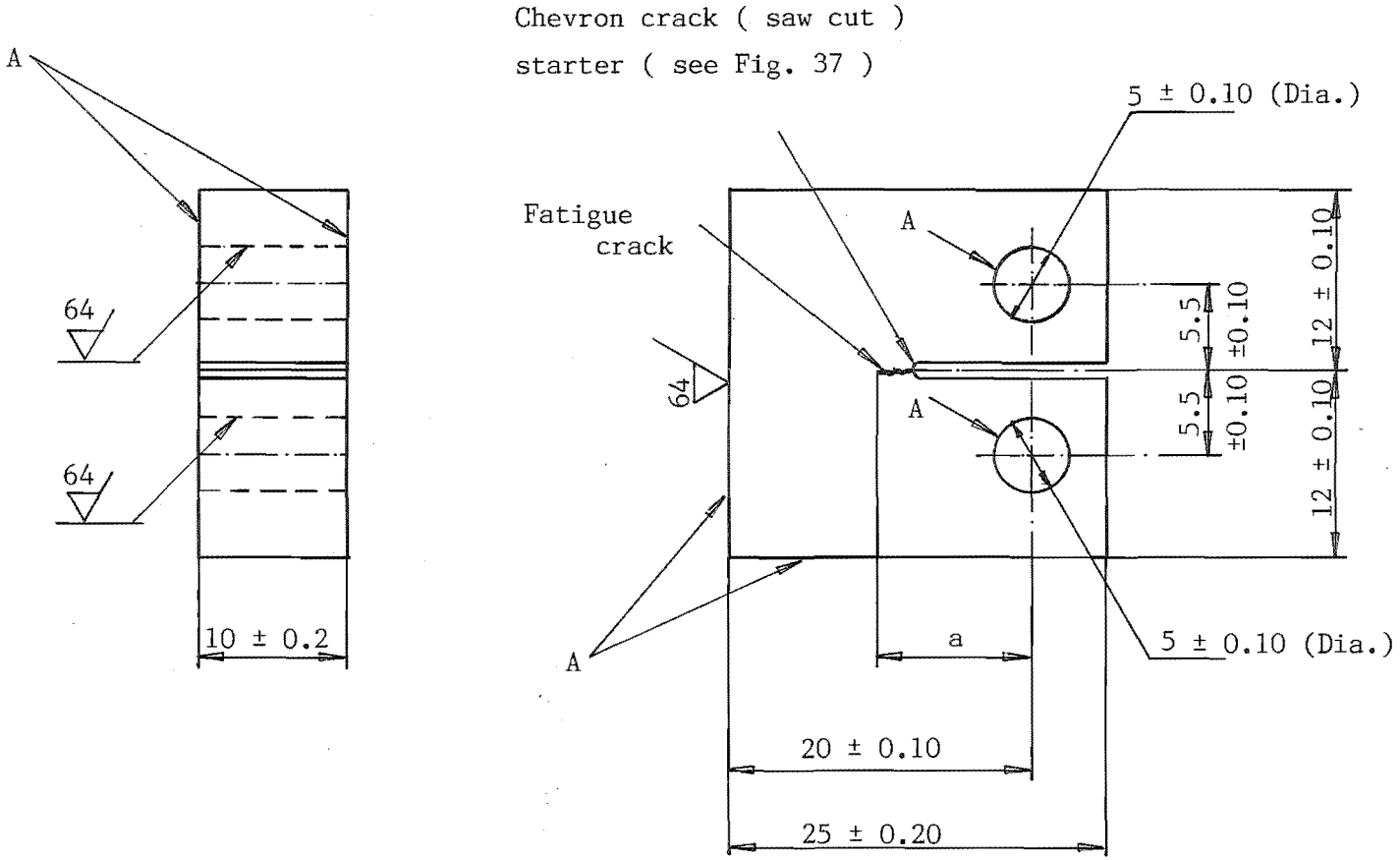

Note: Surfaces A shall be perpendicular or parallel as applicable to within 0.04 mm.

Fig. 36: The ASTM compact tension specimen[8]
(All dimensions in mm)

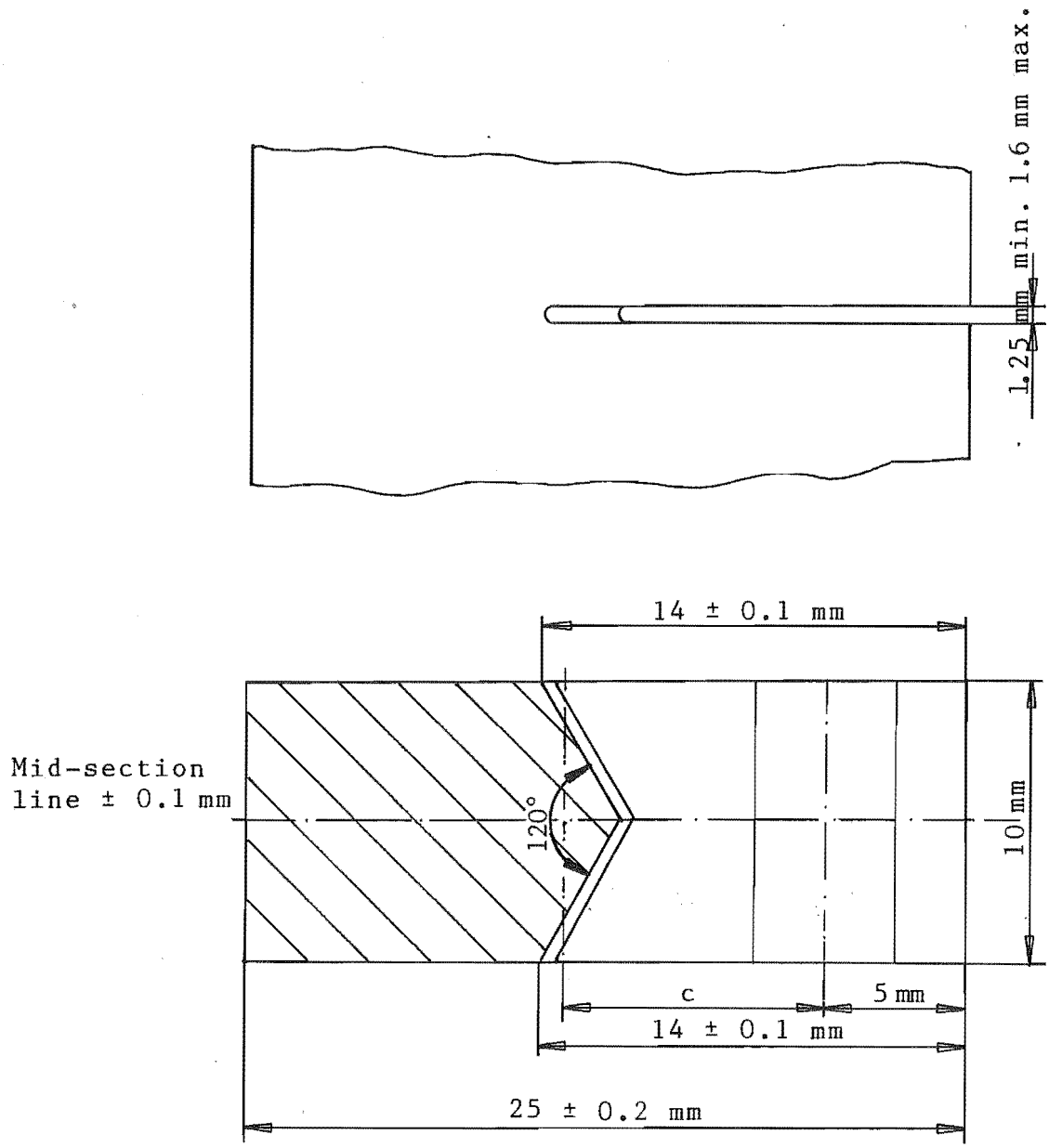

* c : mean slot length (c ≃ 8.3 mm)

Fig. 37 : The modified chevron crack starter

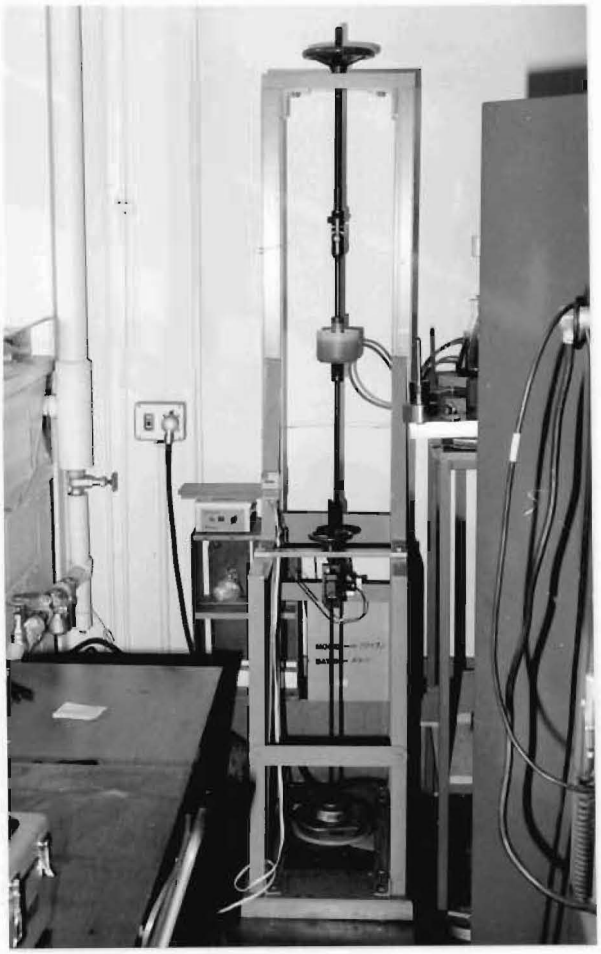

Fig. 38: Stress corrosion testing rig No. 1, rig No. 2 is identical to rig No. 1.
Note that the handwheel at the top of the rig runs on a thrust bearing to reduce friction during the adjustment.
The specimen is attached by the use of clevis and pins to the upper and lower loading bars.

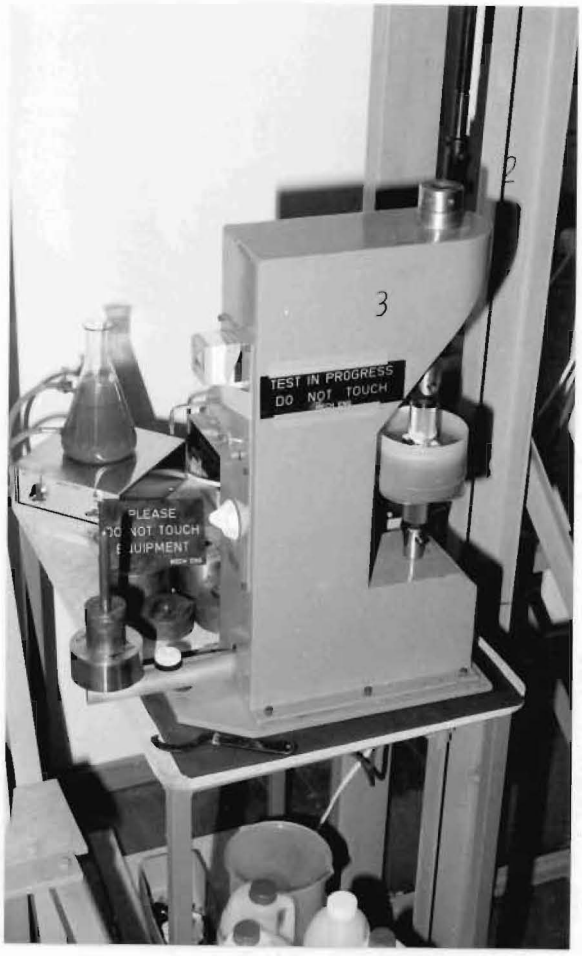

Fig. 39: Stress corrosion testing rig No. 3.
Similar to testing rigs Nos 1 and 2, the adjusting nut at the top runs on a thrust bearing to reduce friction during the adjustment. A screw on the upper loading bar enables the weights to be raised and the constant load applied.

2.1.2 Container Design And Sealing

The solution container had to be designed with a view towards sealing methods, as well as good resistance for the corrosive environment.

The proposed design was to use a plastic bottle of 1 mm wall thickness with 120 mm outside diameter, and 85 mm height. The sealing method used between the plastic container and the adaptor bolt had to be flexible enough to ensure adequate sealing even after relative movement at the test-piece occurred on specimen failure. Therefore, it was decided that a rubber washer of 2 mm thickness (outside diameter: 25 mm, inside diameter: 14mm) would provide a good tight sealing around the adaptor bolt (Fig. 26).

2.1.3 Corrodent Circulation

Circulation of the corrodent through the existing magnetic stirrer pumping system was used to prevent the saline solution from settling in the plastic container. It is important to note that the settling of saline solution would produce a corrodent of uneven concentration, which will affect the test results.

Some corrosion product settled but no salt deposit was found in the plastic container (located in Fig. 40 on the left of the photo). The saline solution in the plastic container moved in a clockwise direction, its flow rate was sufficient to prevent such deposits.

2.1.3.1 Magnetic Stirrer Pumping System

In order to test the existing magnetic stirrer pumping system[36] under operation, and in the absence of the CT specimen, it was decided that a preliminary solution circulation test using a calibration test-piece should be carried out.

The calibration test-piece was positioned between the tension rods of machine 3 according to the operation guide in section 2.4. Transparent plastic tube of 1 mm wall thickness, and 10 mm outside diameter was used for the connecting tubes between the auxiliary flask and the solution container (Fig. 40).

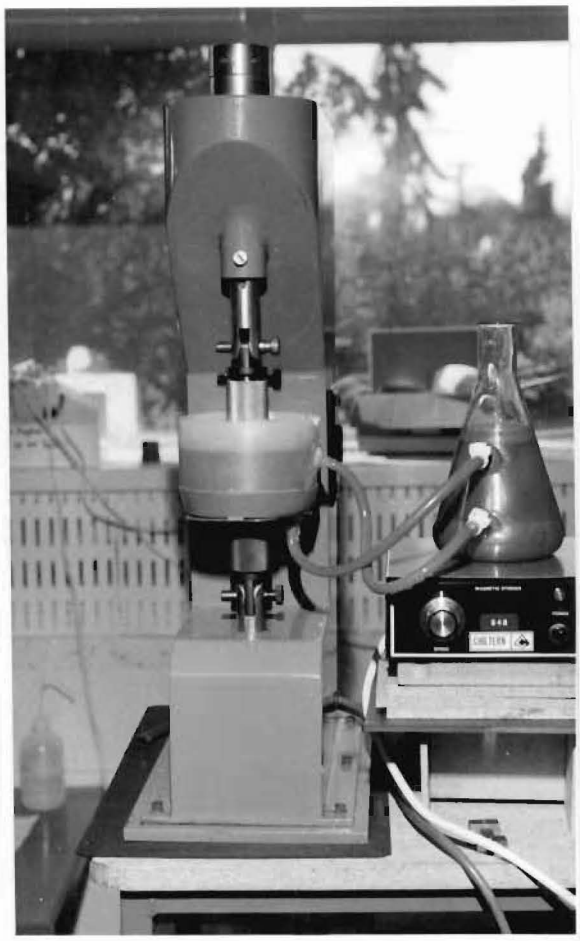

Fig. 40: Stress corrosion testing rig No. 3 with magnetic stirrer pumping system. View to the auxiliary flask: the plastic tube on the top is the outlet to solution container, and the tube at the bottom is the inlet to the flask. Vortex from the magnetic stirrer rotates clockwise.

A circulation test was carried out using cold water (~18° C). Prior to the operation, it was found that large air bubbles remained in the connecting tube. It was also observed that the air bubbles trapped in the tube would cause an air-lock in the circulation test, and stop the solution circulating. Since the cause of the entrapped air bubbles in the tube was the inadequate bleeding of the system during initial filling, it is suggested that a plastic wash bottle filled with solution should stand by the rig, because the air

bubbles in the connecting tube could be easily evacuated by squeezing the solution in the wash bottle into the plastic tube in the solution container. The use of transparent plastic tube as the connecting material has also made filling easier by making any air bubbles readily apparent and therefore steps can be taken to remove them.

During the test it was found that turbulence caused by full speed revolution of the magnetic stirrer created some small bubbles in the connecting tube, therefore, it is suggested that a setting of about 70% of full speed of the magnetic stirrer would ensure a smooth run of the system.

2.1.3.2 The Results Of The Solution Circulation Test

The existing magnetic stirrer pumping system was found to be able to fulfil the requirements of the stress corrosion test, i.e.,

(1) reliability and long life;
(2) ability to handle the corrosive environment of 3.5% NaCl solution;
(3) sufficient degree of intergrity to be able to be left unsupervised overnight.

2.2 Calibration Test-Piece Design

There is no standard calibration test-piece for stress corrosion testing either with constant load or constant deflection devices. Therefore, it was necessary to develop a test-piece to suit all the three existing stress corrosion machines.

It is observed that the dimension between the two specimen holders (upper and lower) of testing rig Nos 1 and 2 is not critical, therefore, the length dimension of the test-

piece was based on the configuration of the testing rig No. 3.

The design shown in Fig. 35 was chosen because of its long parallel section to which strain gauges were adhered and it fitted well to the designed loading clevis.

The calibration test-piece of the low carbon steel En 3 should have a fine surface finished, so it allows adhesion of the strain gauges. It is important to note that a rough surface would effect the adherence of strain gauges, thereby affecting accuracy of the experimental results. It should be noted that the fine surface finished has no influence on the calibration test, because specimen fracture was not required, and the test was only measuring the rate of change of displacement with load within the elastic limit.

2.3 Test Solution Preparation

The experimental environment for testing the CT-specimens was decided to be a cold aqueous solution ($\sim$18° C) of 3.5% NaCl (sodium chloride). This environment has been widely used by the recent workers in tests for delayed fractured susceptibility.[9, 49, 77]

The corrosion reactions occurring at the local anodes and cathodes during wet corrosion of steel have been described in section 1.4.

Hydrogen discharge (see section 1.4, reaction 3) and catalytic combination (see section 1.4, reaction 4) are shown to dominate in acid solutions while oxygen reduction (reaction 2) is the dominant cathode reaction in neutral or alkaline solution. However, according to Cowling[9], the following corrosion reactions may take place in aqueous sodium chloride:-

$$Fe \rightarrow Fe^{2+} + 2e \quad \text{(at the anodic region)}$$

$$2H^{+} + 2e \rightarrow 2H \quad \text{(at the cathodic region)}$$

The "standard" solution of 3.5% aqueous NaCl refers to 3.5% of the pure sodium chloride (salt) and not to its hydrate NaCl solution. Preparation of a solution appropriate strength is achieved through the following procedure:

105 grams (exact) of pure sodium chloride was obtained and placed in a 3000 ml container. To this, 2900 ml of distilled water was added. Upon stirring it was found that 105 grams of sodium chloride had prepared approximately 3000 ml of solution.

It was not necessary to do a pH check because only distilled water was used in the saline solution. However, it is recommended to check the pH-value, if tap water was used for the test.

2.4 Operation Of The Stress Corrosion Testing Rigs

The CT specimen is held between top and bottom loading clevis (Fig. 26), the lower being connected to the lever loading system (Fig 39 and 40), and the upper to an adjusting nut arrangement, so that the lever can be levelled with the specimen in the correct position.

The adjusting nut (handwheel for testing rig Nos 1 and 2) runs on a thrust bearing to reduce friction. The specimen is pinned at the top and the bottom loading clevis (Fig. 26), the upper of which has a quick release pin.

The loading lever operates a micro-switch inside the machine to cut off the power when a specimen fails, and to switch off the hour meter attached to the testing rig, hence the hour meter automatically records the duration of a test. For the testing rig No. 3, a small rubber buffer on the baseplate below the loading lever absorbs the shock when the specimen fractures.

Replacing a fractured specimen is straightforward. The weights are removed and the loading pin disconnected from the clevis. The top tension rod is detached from the adjusting nut (or handwheel); when the adjusting shaft is screwed up out of the way, the lower part of the fractured specimen can be removed from the corrodent container. It is then quite simple to dismantle the upper part of the fractured specimen, clean out the plastic container and, reversing this procedure, to fit a new specimen.

2.5 Calibration Of The Stress Corrosion Rig

Object:

To verify the lever ratio of the constant load testing rig No. 3 through the comparison of the compliance functions (rate of change of displacement with load) with testing rigs Nos 1 and 2 having a defined lever ratio of 10:1.

2.5.1 Calibration Procedure

A test-piece of low carbon steel (En 3) as shown in Fig. 35 was prepared by the department workshop. The calibration test-piece dimensions were measured and two strain gauges were attached directly to two side faces of the test-piece.

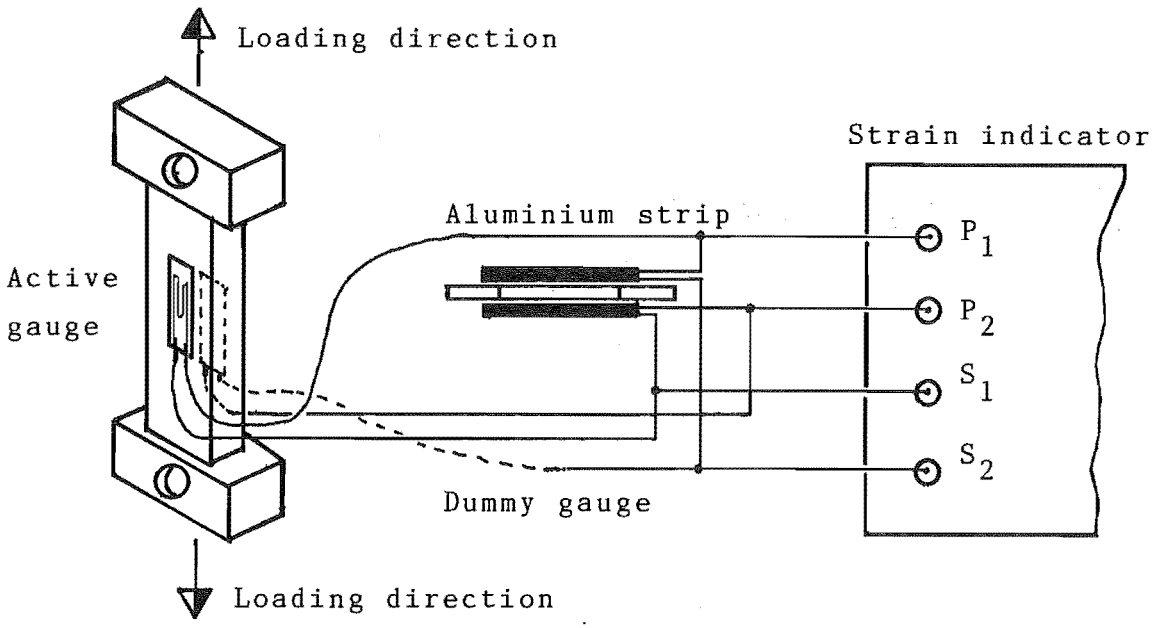

Fig. 41: Full bridge arrangement

The rate of change of displacement with load for three existing stress corrosion testing rigs was measured by the full bridge arrangement as shown in Fig. 41. The displacement readings on the strain indicator are the average strain measurements of the two active gauges on the side faces.

Before describing the results, it is important to appreciate that, in the author's experience, the strain measuring circuit used in the early calibration experiments (quarter-bridge arrangement) was insufficiently stable to produce satisfactory accuracy. The quarter-bridge arrangement was unstable, because of the small bending moment acting on the calibration test-piece. The small bending moment on the test-piece was due to the non central position at which the load was applied to the calibration test-piece. However, the strain difference between the left and right side face was minimal (see Figs 42 & 43), and this means that the bending moment on the testing rigs was not significant.

The full-bridge arrangement provided complete long term stability.

Thermal sensitivity was considered to be less significant, because of the use of steel compensated strain gauge adhering to the steel calibration test-piece. Both have the same thermal expansion coefficient and this meant that the strain gauge would expand at the same rate as the test-piece. However, it is noted that the use of compensated gauges may reduce the problem of fluctuations with temperature, but most certainly doesn't eliminate it.

In our calibration test the full-bridge was attached to the specimen with two active gauges located at the centre of the side face of the calibration test-piece, and two 'dummy' gauges were mounted on an adjacent strip of aluminium (Fig. 41). The excitation current was $\sim$10 volts

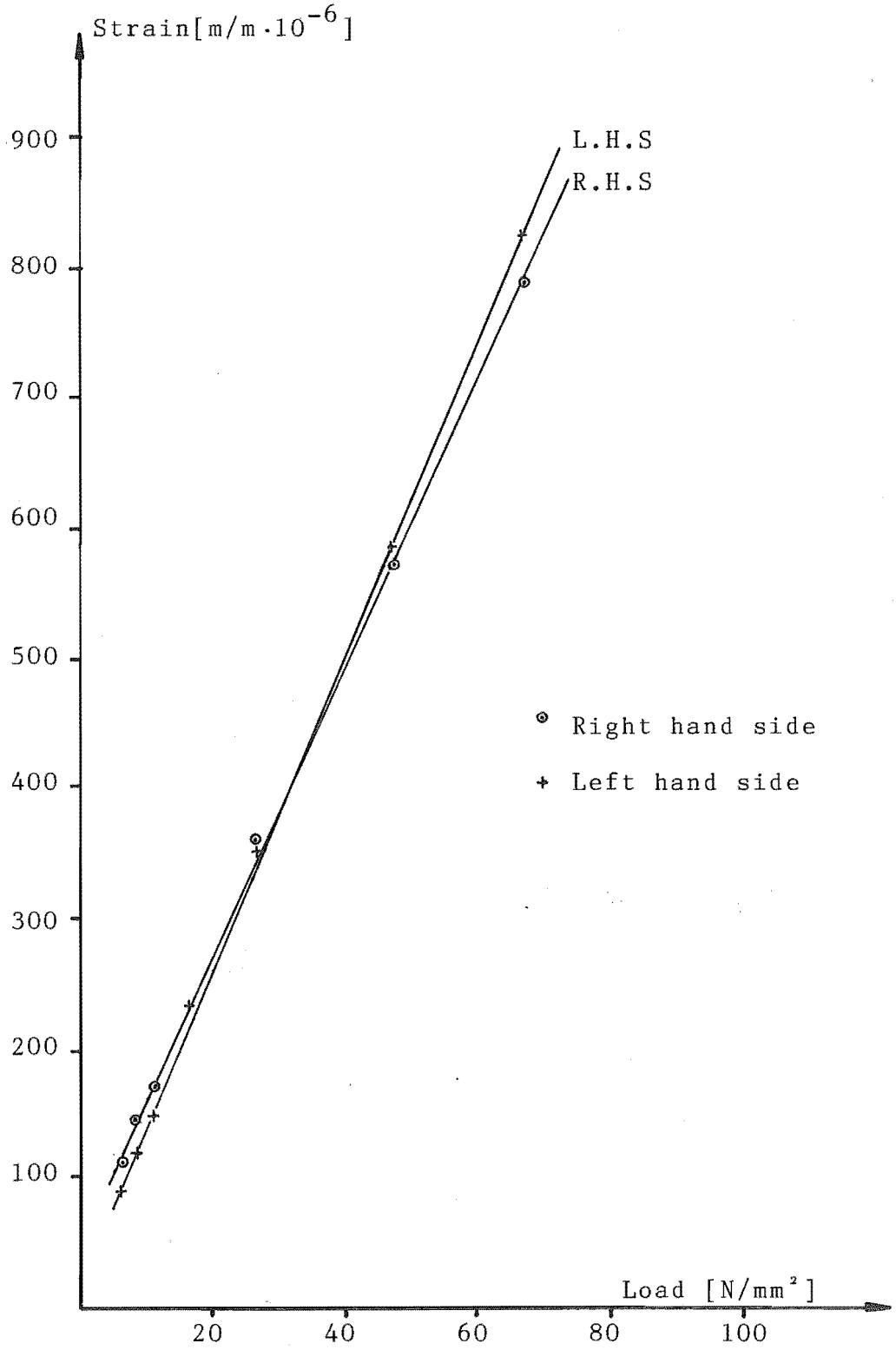

Fig. 42 : Quarter bridge calibration curves for stress corrosion rig No.1.

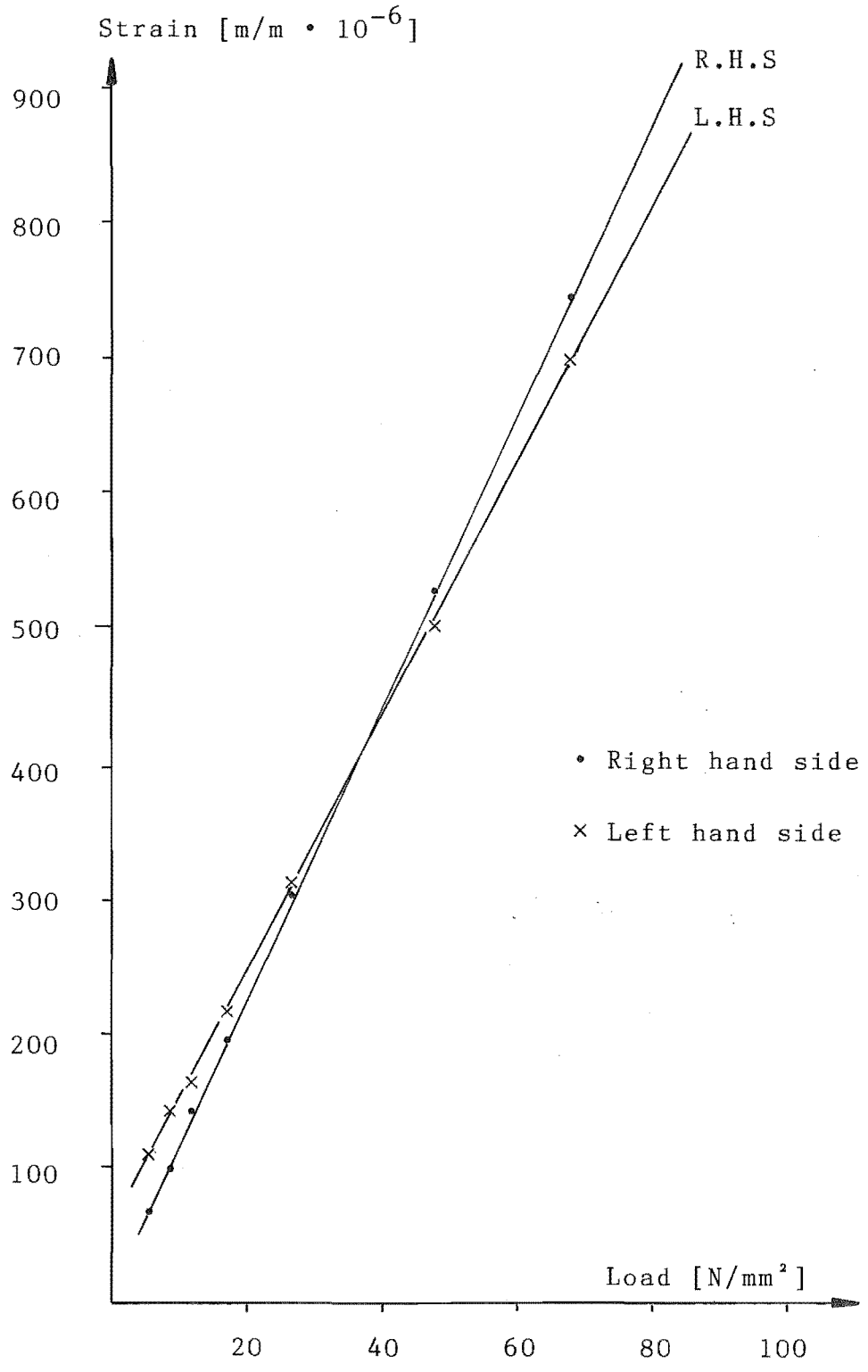

Fig. 43 : Quarter bridge calibration curves for stress corrosion rig No. 2.

Table 9 : Quarter bridge measurements for stress corrosion testing rig Nos. 1 and 2

Testing rig No.	Applied load on the specimen [N/mm^2]	Strain [μm/m]	
		L.H.S	R.H.S
1	6.4	92	119
	8.8	110	158
	11.4	150	175
	16.4	236	226
	26.3	350	359
	46.7	585	570
	66.2	820	781
2	6.4	115	80
	8.8	152	108
	11.4	165	142
	16.4	210	192
	26.3	314	290
	46.3	502	528
	66.2	695	746

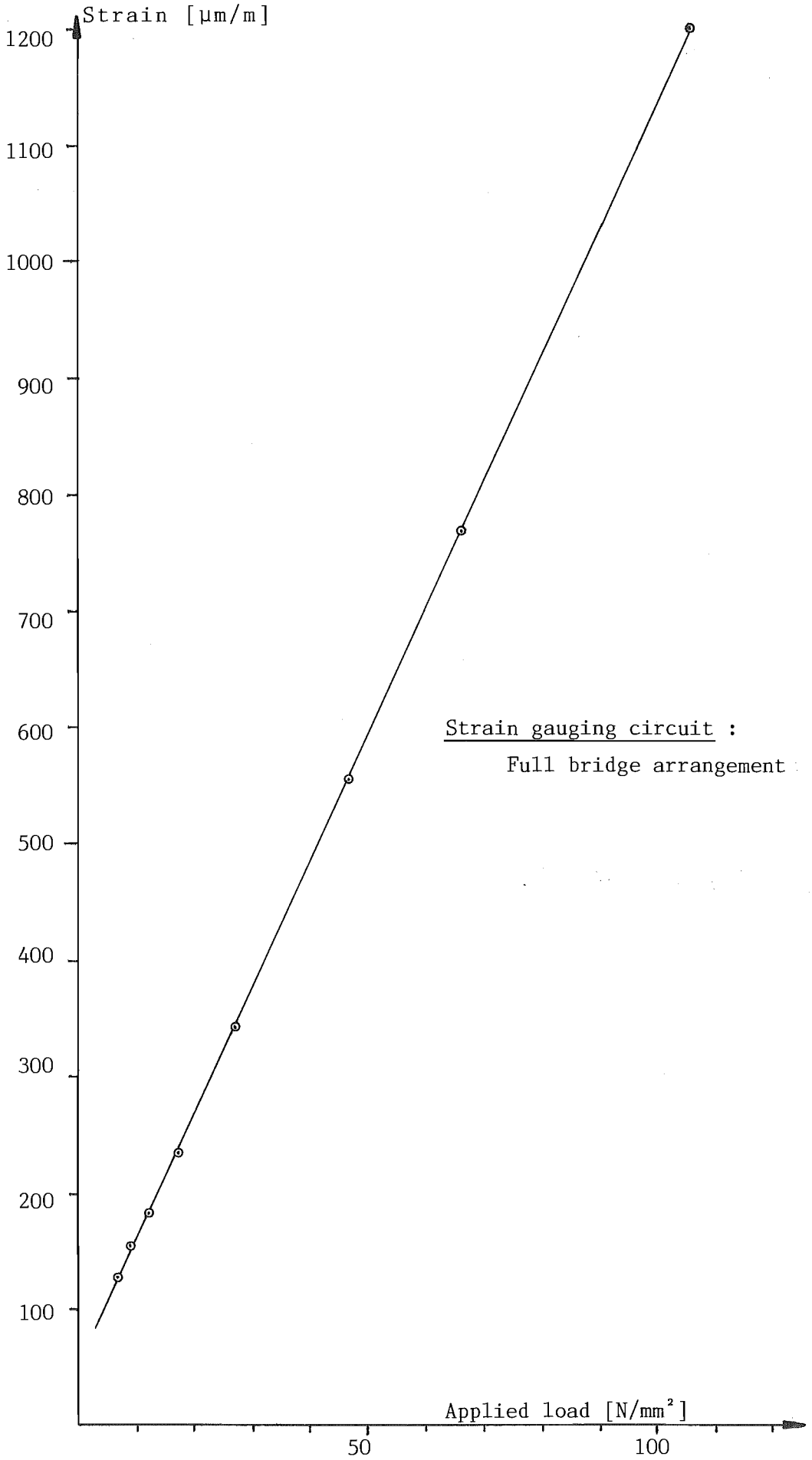

Fig. 44 : Load-extensiongraph for testing rig Nos 1 & 2

Table 10 : Machine 1

Specimen cross sectional area = 5 x 10 = 50 mm^2

Weight on pan	Applied stress on the specimen	Strain
[N]	[N/mm^2]	[$m/m \cdot 10^{-6}$]
319.96	6.4	127
442.56	8.85	154
569.15	11.38	180
818.34	16.37	234
1316.72	26.33	342
2313.48	46.27	557
3310.23	66.20	772
4306.99	86.14	989
5303.75	106.0	1208

Table 11 : Machine 2

Specimen cross sectional area = 5 x 10 = 50 mm^2

319.96	6.40	127
442.56	8.85	152
569.15	11.38	182
818.34	16.37	234
1316.72	26.33	346
2313.48	46.27	556
3310.23	66.20	775
4306.99	86.14	992
5303.75	106.0	1211

Table 12 : Machine 3

Specimen cross sectional area = 5•10 = 50 mm^2,
Lever ratio :- 45 : 1

Weight on pan [F] [N]	Applied stress on the specimen [N/mm^2]	Strain [$\mu m/m$]
115.6	2.30	84
290.47	5.80	120
564.17	11.30	178
1007.83	20.20	273
1893.38	37.90	460
2341.45	46.80	560
3233.18	64.70	756
3669.33	73.40	860
4561.06	91.20	1040
These figures were confirmed by the actual dead weight on the pan with the lever ratio of 45 : 1	These figures are read from Fig. 44	

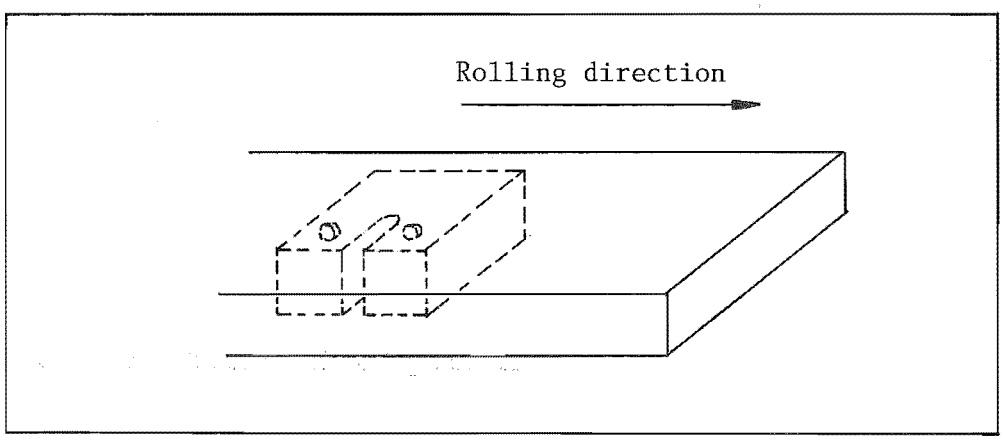

Fig. 45 : Orientation of CT specimen

d.c. and the out of balance voltage was amplified and displayed on a conventional voltmeter mounted on the strain indicator.

The foil gauges were of 120 Ω resistance with a 5 mm gauge length. The static loads were interrupted periodically to determine strain as a function of load up to a value corresponding to $\sigma_{app} = 106 \frac{N}{mm^2}$. The variation in strain with load along the side faces of the specimen for the three testing rigs is listed in Tables 10, 11 and 12.

2.5.2 Calibration Results

A load-extension graph for Stress Corrosion Rigs No's 1 and 2 is shown in Fig. 44. It is observed that both machines have identical characteristics.

The basic set of instructions with Stress Corrosion Rig No. 3 quoted the lever ratio as being 45:1 calculated from the assembly drawings[36], and this has been confirmed from the experimental data (Table 12).

2.6 Material And Procedure

Round bar of 26 mm diameter was taken from a commercial high strength steel ULTIMO 200 and hot rolled to produce a flat section of 12 mm thickness.

All the specimens used were of longitudinal orientation and notched in the through thickness direction (Fig. 45).

ULTIMO 200 steel was chosen for the test because this steel has similar chemical composition and mechanical properties to AISI 4340 steel, which has been very widely used for investigations of stress corrosion cracking.[9, 33, 77]

ULTIMO 200 steel had the following chemical analysis:

Composition of ULTIMO 200 Steel

	C	Mn	Si	Ni	Cr	Mo	S	P	Cu
Wt. percentage	0.43	0.60	0.28	1.70	0.74	0.17	0.017	0.024	0.07

The CT specimens were machined to the shape as shown in Fig. 36. It was suggested that a Chevron Notch with a flank angle of 120^{o} (see Fig. 37) be slotted in the specimens. Test specimens were finished to within close tolerances by fine grinding after heat treatment. In the heat treatment process, all the specimens were heat treated to 1600 MPa tensile strength level according to the following sequence:-

(1) Austenitized the specimens at 850^{o} C for one hour.
(2) Oil quenched.
(3) Tempered at 350^{o} C for one hour and furnace cooled.

Before testing it was necessary to insert a fatigue pre-crack in the CT specimen. For this an Amsler Vibrophore fatigue machine was used and pre-cracking was carried out in air and 3.5% NaCl solution.

For running the sustained load tests, a binary search programme (Fig. 46)[9] was adopted for determining the susceptibility curve (applied stress versus time-to-failure).

The final stress intensities of different pre-crack environments and load conditions are listed in the next section. N.B., the length of the fatigue pre-crack was within the range 0.5 to 0.6 $\frac{a}{W}$. It is important to note that both side faces of the CT specimen had been polished by the use of diamond lapping compound of 5 micron fineness. The well polished side faces would enable the crack growth to be more easily observed.

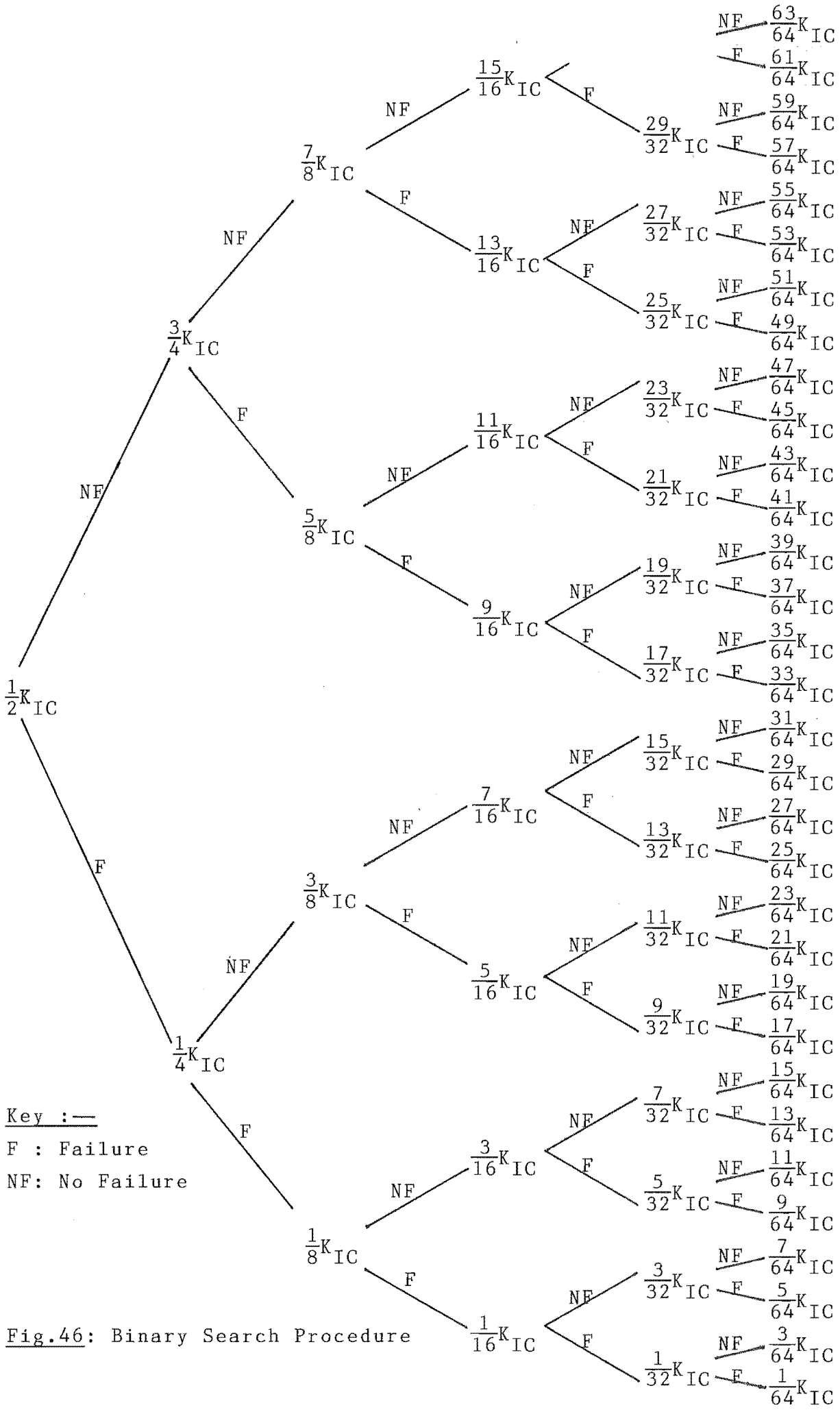

Fig.46: Binary Search Procedure

It was observed that for the chevron notch with a flank angle of 120° the fatigue crack initiation during the pre-cracking (at a low level of stress intensity) process was slow. According to ASTM E399[8], there are several methods of promoting early crack initiation:-

1) by using a chevron notch,
2) by providing a very sharp notch tip,
3) by using a negative fatigue load ratio; for a given maximum fatigue load, the more negative the load ratio, the earlier crack initiation is likely to occur;
4) by statically pre-loading the specimen in such a way that the notch tip is compressed in a direction normal to the intended crack plane but without allowing the specimen strength ratio to be less than -1.

To facilitate fatigue pre-cracking at a low level of stress intensity, it is likely that the third and fourth methods are theoretically possible but difficult to actually apply, particularly in view of the low fatigue load. Hence, ASTM E399 proposed that the notch root radius of a chevron notch should be less than 0.25 mm because of the compound stress intensification at the point of the chevron.

In the present work, the chevron notch was produced by a slotting machine with a 0.3 mm thick diamond wafering blade. This implies that the existing notch root radius is greater than 0.25 mm. Therefore, the fatigue crack initiation at a low level of stress intensity was slow. In order to allow for a reasonable length of fatigue crack to be developed in the CT specimen, and to enable easier control to be exercised over the crack propagation rate, it is suggested that a thiner diamond wafering blade (e.g., of 0.2 mm thickness) shall be used in slotting process for subsequent work. It is noted that there is some difficulties in getting a 0.2 mm thick diamond wafering blade in New Zealand.To overcome this it would be necessary to contact the diamond wafering blade manufacturer (Buehler Ltd., 2120 Greenwood st., Evanston, III, U.S.A 60204) for further details.

Alternatively, a narrow slot can also be produced by a spark machine. The application of spark machine to the slotting process was mentioned by Richards and Deans[80]. They have reported that a narrow (0.25 mm wide) spark-machined slot was used to initiate a fatigue pre-crack in a 25 mm thick CT specimen. It is believed that the use of the spark-machined slot (0.25 mm wide) may promote an early crack initiation in the specimen during the pre-cracking process.

On the other hand, according to ASTM E399, the chevron crack starter notch of 120° is a maximum allowable flank angle that can be introduced into CT specimen. It is assumed that the smaller the flank angle, the faster the fatigue pre-crack will be completed. It is recognized that there is no experimental evidence to support the above assumption. Therefore, it is suggested that, for subsequent work, the chevron flank angle can be altered.

However, according to ASTM E399[8], the following precautions should be born in mind for alternation of the flank angle:

1) The difference between any two of the three pre-crack length measurements (i.e., the crack length measurements at the following position: the center of the fatigue crack front, and midway between the center of the fatigue crack front and the end of the fatigue crack front on each side face of the specimen) shall not exceed 10% of the average of the three measurements.

2) The fatigue crack shall emerge from the chevron notch (Figs 36 & 37) on both surfaces of the specimen. Neither surface crack length shall differ from the average crack length by more than 10%, and the difference between these two surface measurements shall not exceed 10% of the average crack length.

2.7 Stress Intensity At The Fatigue Crack Tip [ΔK]

To facilitate calculation of ΔK, the value of Y is calculated by using the following formula from ASTM standards.[8]

$$Y = \frac{(2 + \frac{a}{W})\cdot(0.866 + 4.64\,\frac{a}{W} - 13.32\,\frac{a^2}{W^2} + 14.72\,\frac{a^3}{W^3} - 5.6\,\frac{a^4}{W^4})}{(1 - \frac{a}{W})^{3/2}} \qquad 1)$$

and for ΔK

$$\Delta K = \frac{P_f}{B\cdot W^{\frac{1}{2}}}\cdot Y \qquad 2)$$

where: B = 10 mm = specimen thickness

W = 20 mm = specimen width.

2.7.1 Specimens Fatigue Pre-Cracked In Air

Specimen I.D. No.	Applied dynamic load P_f(N)	Final fatigue crack length a_f(mm)	Value of Y = f(a/W), for W = 20 mm	ΔK (MN/m$^{3/2}$)
23	4000	11.25	11.872	33
28	2500	11.025	11.413	20
9	1480	11.125	11.613	12
13	500	11.375	12.140	4

2.7.2 Specimens With Subcritical Crack Growth In 3.5% NaCl Solution

24	942.9 N, static loaded for 289 hours.	11.300	11.980	8

2.7.3 Specimen Pre-cracked In 3.5% NaCl Solution With 2.5 KN Dynamic Load

Specimen I.D. No.	Applied dynamic load P_f(N)	Final fatigue crack length a_f(mm)	Value of Y = f(a/W), for W = 20 mm	ΔK ($MN/m^{3/2}$)
15	2250	11.575	12.592	20

2.8 Fracture Mechanics

As mentioned at the outset, stress corrosion cracks do not propagate below the threshold stress, no matter how long they are maintained. In terms of stress intensity factors, these features are illustrated in Figure 3. And the essential experimental set-up for determining a time-to-failure curve with threshold stress (K_{Iscc}) is shown in Fig. 4.

The CT specimen (Fig. 37) is first fatigue-cracked after introducing a notch of 0.3 mm by diamond wafering blade (Fig. 55). The Initial Stress Intensity (K_I) is determined from the length of the pre-crack using the formula of $K = \frac{P \cdot Y}{B \cdot W^{\frac{1}{2}}}$.(8) The crack length at the final rupture (Fig. 47) should give K_{IC}, which is commonly called the critical value of the Stress Intensity Factor.(9) It is important to note that K_{IC} is also known as the fracture toughness of a material.

Two methods could be used to determine the pre-cracked area. In the first: the area at rupture was obtained from a calibration plot - determined by the calibrated strain on the back face (the face opposite that from which the slot is machined) of the compact tension (CT) specimens. This provides a method for measuring crack length when load is known.

In the second: visual examination of the fractured specimen, the fracture surface revealed two distinct modes of crack propagation (Fig. 47). According to ASTM, E399[8], measure the pre-crack length, a,after fracture to the nearest 0.5% at the following three positions: at the center of crack front, and midway between the center of the crack front and the end of the crack front on each side face of the specimen. The average of these three measurements are used as the crack length to calculate K_{IC} value. It is noted that this method was actually applied to determine the pre-cracked length after the test, and a vernier calliper was used to measure the pre-crack length. In addition, a suggested K_{IC} data sheet (see Appendix)[8] was used to record test information and to evaluate the test result.

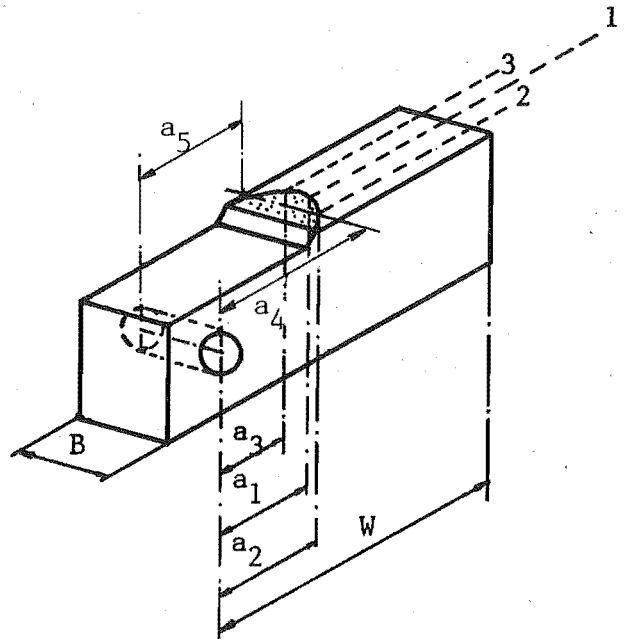

N.B., The mean value of the final pre-crack length ($\bar{a}$) is given by:

$$\bar{a} = \frac{a_1 + a_2 + a_3}{3}$$

Fig. 47[8]: Crack plane of the CT Specimen.

From Fig. 48 it can be seen that the fracture interface formed by slow (hydrogen-induced) crack propagation exhibited a fine texture (intergranular), indicative of brittle fracture. The final fracture surface (Fig. 48), formed by rupture, was rougher and indicated a more ductile fracture.

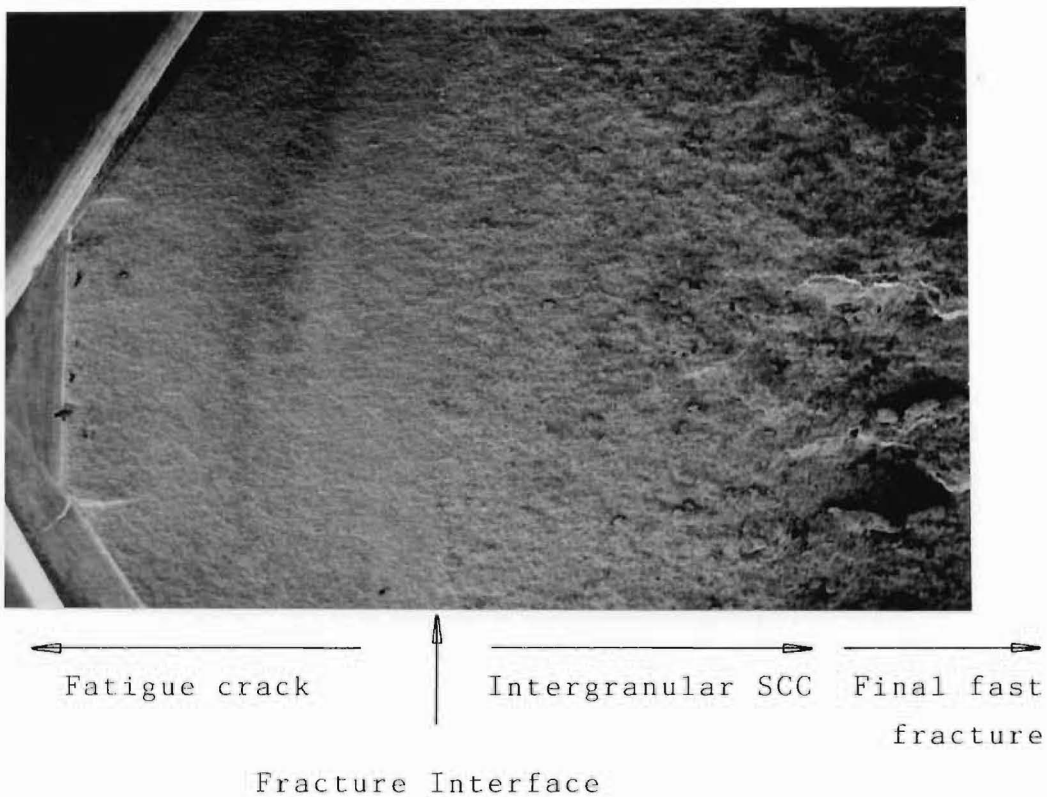

Fig. 48: Fracture modes found on fracture surface of CT SCC specimen. Dark area on the right indicates extent of hydrogen-induced crack zone, at 18 x. (Note that the hydrogen-induced crack zone is detailed in higher magnification fractographs in section 4.1.2)

Any attempt to use fracture mechanics to design against stress corrosion failures must be based on the threshold value (K_{Iscc}), and this amounts simply to substituting K_{Iscc} for the usual K_{IC} value in determining critical flaw size.

2.9 Initial Testing

2.9.1 Tensile Test On ULTIMO 200 Steel

Object: To measure the mechanical properties of ULTIMO 200 Steel by tensile test.

Procedure:

Blank was cut from the hot rolled 12 mm thick flat section, then annealed before rough-machining. The specimens were austenitized for 1 hour at 850°C in the furnace, oil-quenched, then tempered for 1 hour at 350°C.

Final grinding was carried out to the dimensions shown in Fig. 49 after heat treatment.

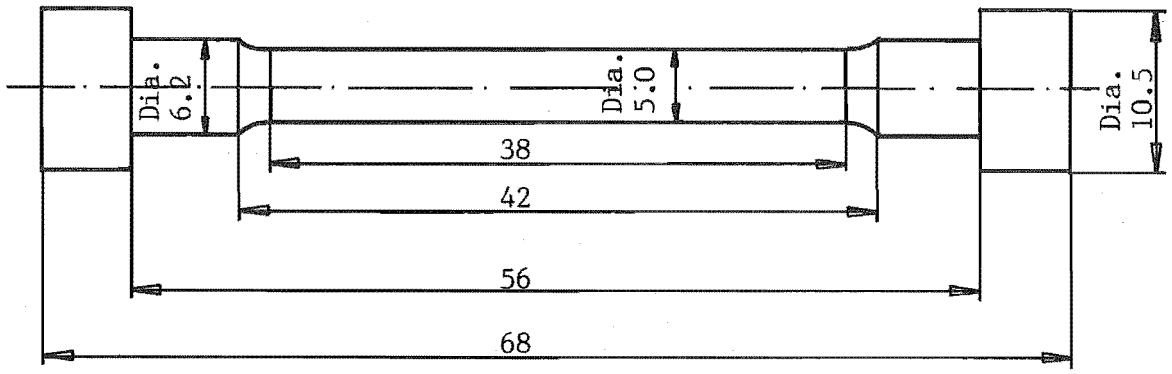

*All dimensions in mm

Fig. 49 : Tensile test specimen

The diameter was checked, and a 25 mm gauge length was scribed. The test-piece was positioned, crosshead speed was set to 0.02 cm/min, and the load applied. A load-extension record was obtained on the recording drum.

Results:

0.2% Proof Load (mean value) : 29.8 KN

Maximum load: 31.4 KN

Specimen diameter and cross area: $r = 2.5$ mm

$A = \pi r^2 = 19.635$ mm^2

Tensile strength (U.T.S): $\frac{31.4}{19.635} = 1599 \frac{N}{mm^2}$

$\fallingdotseq$ 1600 MPa

0.2% Proof stress: $\frac{29.8}{19.635} = 1518 \frac{N}{mm^2}$

= 1518 MPa

The fracture surfaces of the tensile test pieces are shown in Figs 50, 51 & 52.

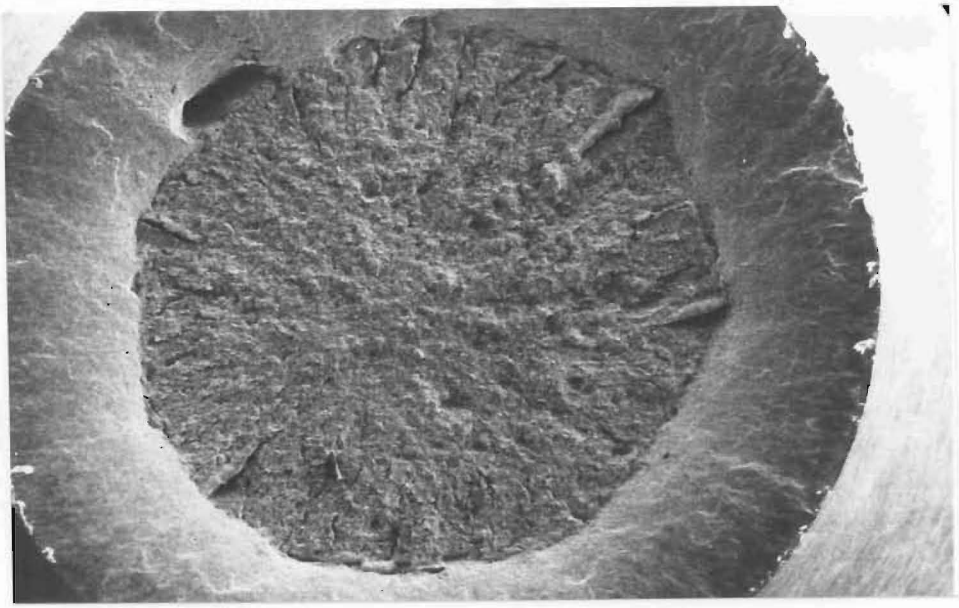

Fig. 50: Fractograph of the tension-overload fracture in ULTIMO-200 steel specimen, with two different areas (i.e., the central fibrous zone and circular shear lip), tested in tension at room temperature. Tensile strength was 1599 MPa, at 27 x.

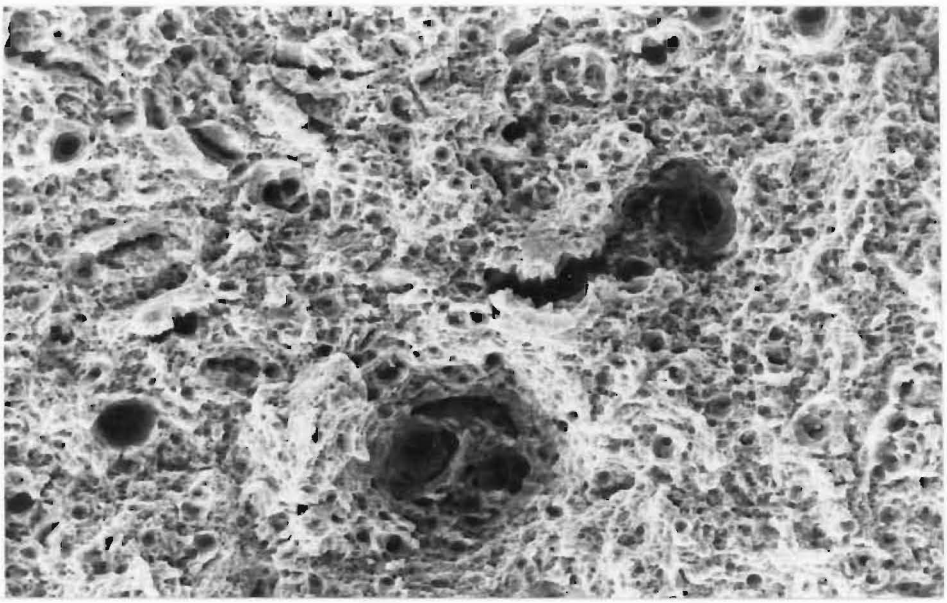

Fig. 51: SEM fractograph taken directly from the central fibrous zone of the tensile fracture in Fig. 50, at 800 x.

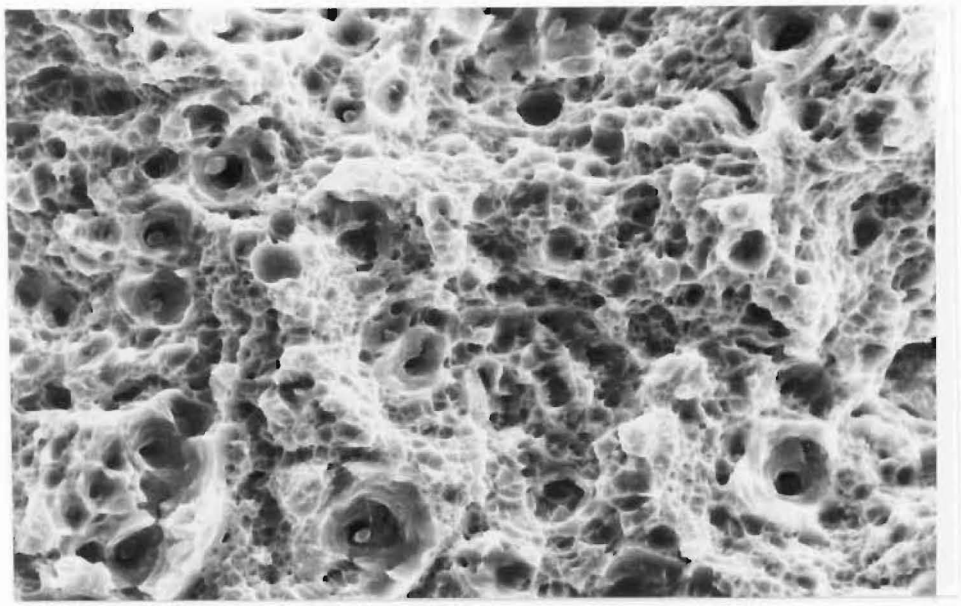

Fig. 52: The appearance of dimples as seen in Fig. 51, at 2200 x.

2.9.2 Fracture Toughness Measurement

The fracture toughness measurement according to ASTM E399[8] was carried out using an Instron universal testing machine at a constant crosshead speed of 0.2 mm per minute. The loading of CT specimen was achieved by a pin - and loading clevis arrangement, and the crack propagation was detected by an Instron crack opening displacement gauge. The clip gauge opening was set to 10 mm and calibrated in 0.1 mm steps up to 11 mm. The main function of the displacement gauge is to provide an input to the Instron servo chart drive system that advances the recorder chart in proportion to the displacement sensed by the gauge.

The stress intensity value was determined from the measurement of the load at a fixed displacement using the following equation.

$$K = \frac{P \cdot Y(a/W)}{B \cdot W^{\frac{1}{2}}} \qquad (1)$$

where P is the applied load, and a, B and W are the crack length specimen thickness and width, respectively. The value Y(a/W) can be determined by the equation detailed in section 2.7.

Figure 53 shows the results obtained for a CT specimen tested in tension to fracture in air are as follows:- The P_Q and P_{max} values were determined by the measurement values of the load-displacement record.

According to ASTM E399[8], the initial slope of the linear portion of the load-displacement record shall be between 0.7 and 1.5. The calculated result from the test record on Fig. 53 has a initial slope of 2.93. Obviously, the calculated slop was out of the range. However, since P_Q could be determined from the record with an accuracy of ± 1%. Therefore, it is noted that the test record satisfies the requirements of ASTM E399. The method of P_Q determination is detailed in section 1.2.3. However, it should be noted that the test record has the form of Fig. 2b in section 1.2.3.

The principal loads recorded in the fracture toughness determination were:-

$$P_Q = 6.6 \text{ KN}$$

$$P_{max} = 6.7 \text{ KN}$$

The ratio P_{max}/P_Q is equal to 1.015, this result is smaller than 1.1, this means that it is allowed to proceed the calculation of K by using equation (1).

The fracture toughness (K_{IC}) value was made by the following calculations:

The specific value of a/W is equal to $\frac{11.5}{20} = 0.572$, so the value of Y(a/W) is given by Eqn. 2.1 (see section 2.7) as 12.420, put all these into equation 1) on previous page:

$$K_{IC} = \frac{P_Q}{B \cdot W^{\frac{1}{2}}} \cdot Y(a/W) = \frac{6600\ N}{10\ mm \cdot 20^{\frac{1}{2}} mm^{\frac{1}{2}}} \cdot 12.42 = 1832.9\ \frac{N}{mm^2} \cdot mm^{\frac{1}{2}}$$

$$\underline{K_{IC} = 58\ MN/m^{3/2}}$$

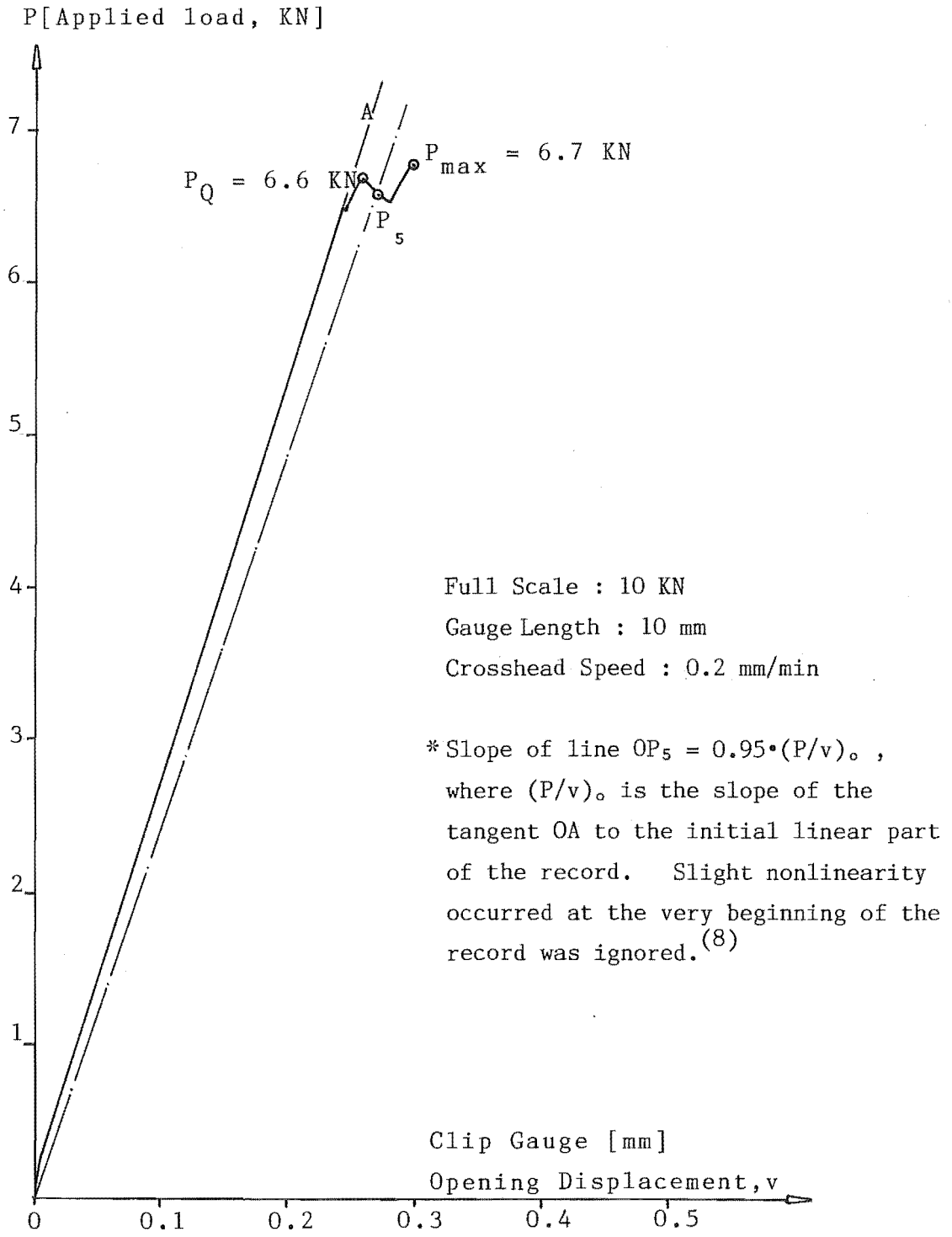

Fig. 53: Load-extension record

In order for a result to be considered valid according to ASTM standard E399, it is required that both the specimen thickness B, and the crack length, a, exceed $2.5 \cdot (K_{IC}/\sigma_{YS})^2$, where σ_{YS} is the 0.2% offset yield strength of the tensile test specimen.

Calculation:

$$B \overset{?}{\geq} 2.5 \cdot \left(\frac{K_{IC}}{\sigma_{YS}}\right)^2 = 2.5 \cdot \left[\frac{1832.9}{1518.0} \; \frac{\frac{N}{mm \cdot mm^{\frac{1}{2}}}}{\frac{N}{mm^2}} \right]^2 = 1.2 \text{ mm}$$

N.B., B_{actual} = 10 mm, and a_{actual} = 11.5 mm. Therefore, both the specimen thickness and the crack length are considered to be satisfactory.

The fracture surface was examined by scanning electron microscopy (SEM) to determine the fracture mode (Fig. 54) with special emphasis on the dimpled surface.

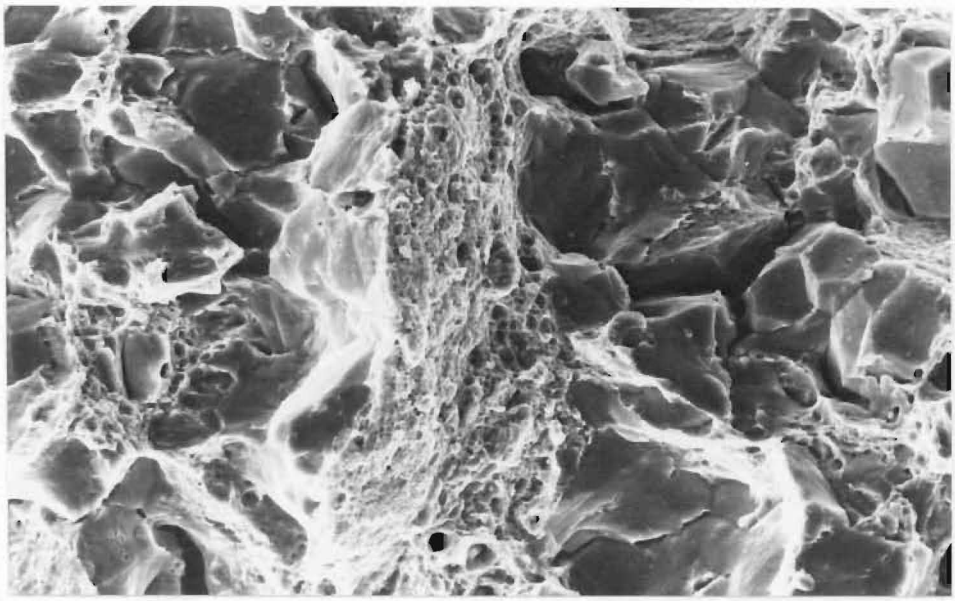

Fig. 54: Typical area of rapid fracture region in the specimen fractured in air, showing a mixture of ductile fracture with intergranular cracking and quasi-cleavage, at 800 x.

2.10 Compressive Back Face Strain Technique

The initial development of this strain gauging technique by Richards and Deans[80] was to enable a study of hydrogen induced cracking from stress concentrations. It was reported that the crack propagation from notches in wedge opening loading specimens was detected by monitoring the sudden change in back face strain (BFS) as the crack initiated.

Richards and Deans[80] also reported in their publication that the compressive Back Face Strain Technique has been successfully applied to detecting crack growth in CT specimens in hydrogen gas at a variety of pressures and temperatures under constant load conditions.

Due to limited time, only a little work has been done on crack length measurement by the use of compressive back face strain gauging. It is not possible to present satisfactory conclusions in this section. However, the BFS technique might be thought to be excellent for providing a method for measuring crack length when the applied load is known or for measuring load when crack length is known.

2.10.1 Slot Length Calibration Experiments On CT Specimens

The calibration experiment was performed on a 10 mm thick CT-specimen. As we can see in Figs 55 and 56, a solid specimen holder was attached to the X-beam for holding the CT specimen. In order to minimize the time or equipment required, a holder was developed that consisted of a section of angle iron of 5 mm thickness (Dimension: 40 mm x 40mm x 40 mm) with two positioning bolts. In addition, a slot of 4 mm width, and 30 mm depth was introduced into the specimen holder. During the slotting process, the CT specimen was bolted on the specimen holder. It is noted that the existing Chevron notch in the CT specimen should be aligned with the slot in the specimen holder, this ensured that the diamond wafering blade performed no extra work on cutting the specimen holder. The CT-type specimen dimensions are shown in Figs 36 & 37. The diamond wafering blade of 0.3 mm thickness was applied to slot the CT specimen in the through thickness direction for various slot lengths for calibration tests.

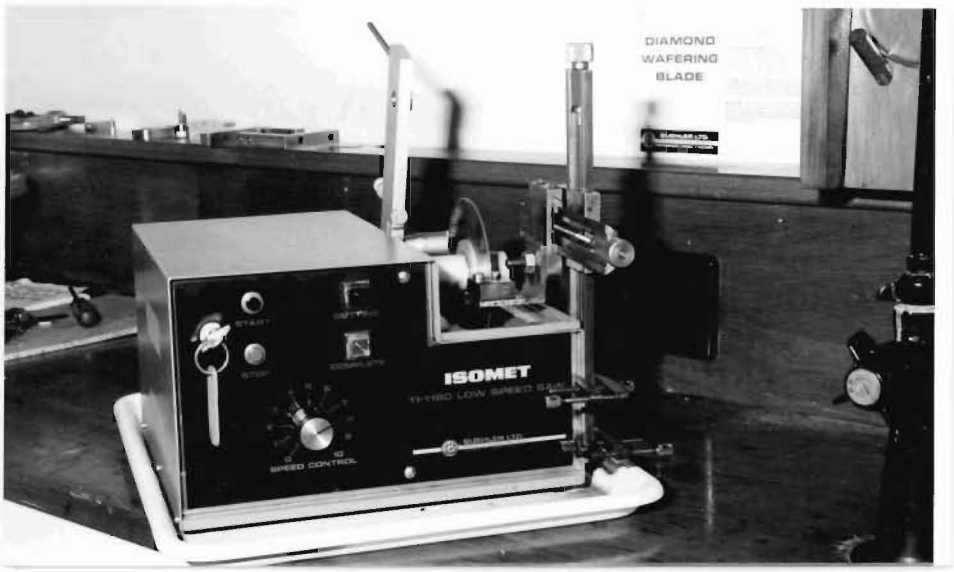

Fig. 55: General view of the slotting assembly

It was noted in the slotting process that the beam of "X-Y beam/column" has to travel from bottom to top during the operation. This is due to the following :- 1) A feed against the diamond wafering blade rotating direction, it prevents the diamond blade from breaking. 2) To produce a straight-through slot in the CT specimen.

The slot lengths produced by the slotting machine were measured optically on both faces of the specimen, with the aid of scribe marks on the specimen at 0.4 mm intervals (Fig. 57). The slot lengths quoted are the average of these two readings.

As pointed out earlier, according to ASTM E399[8], the fatigue crack shall emerge from the Chevron on the both surfaces of the CT specimen, neither surface crack length shall differ from the average crack length by more than 10%,and the difference between these two surfaces measurements shall not exceed 10% of the average crack length. Based on the above considerations, it is thought that a straight-through slot in the CT specimen would minimize the differences, and ensure a successful slot length calibration experiment (see Table 13).

The strain was measured by a single strain gauge located in the centre of the back-face of the specimen (Fig. 58), parallel to the loading direction. The foil gauge was of 120 Ω resistance with a 5 mm gauge length. In the calibration tests a quarter bridge arrangement was used.

Table 13 : Slot lengths [measured by vernier calliper].
* $\bar{a} = (a_L + a_R)/2$; [$\bar{a}$: mean slot length]

Mean slot length $\bar{a}$	Left side face				
	a_L	$\Delta a_1 = \lvert \bar{a} - a_L \rvert$	$\Delta a_1/\bar{a}$	$\Delta a_L = \lvert a_L - a_R \rvert$	$\Delta a_L/\bar{a}$
(mm)	(mm)	(mm)	(%)	(mm)	(%)
10.25	10.2	0.05	0.5	0.1	1
11.55	11.3	0.25	2.2	0.5	4.3
12.45	12.3	0.15	1.2	0.3	2.4
14.35	14.4	0.05	0.3	0.1	0.7
Remarks :			$\ll 10\%$		$\ll 10\%$

Mean slot length $\bar{a}$	Right side face				
	a_R	$\Delta a_2 = \lvert \bar{a} - a_R \rvert$	$\Delta a_2/\bar{a}$	$\Delta a_R = \lvert a_R - a_L \rvert$	$\Delta a_R/\bar{a}$
(mm)	(mm)	(mm)	(%)	(mm)	(%)
10.25	10.3	0.05	0.5	0.1	1
11.55	11.8	0.25	2.2	0.5	4.3
12.45	12.6	0.15	1.2	0.3	2.4
14.35	14.3	0.05	0.3	0.1	0.7
Remarks :			$\ll 10\%$		$\ll 10\%$

As we can see in Table 13, the values of $\Delta a_1/\bar{a}$, $\Delta a_2/\bar{a}$, $\Delta a_L/\bar{a}$, and $\Delta a_R/\bar{a}$ are much smaller than 10%, therefore, the slot length measurements are valid.

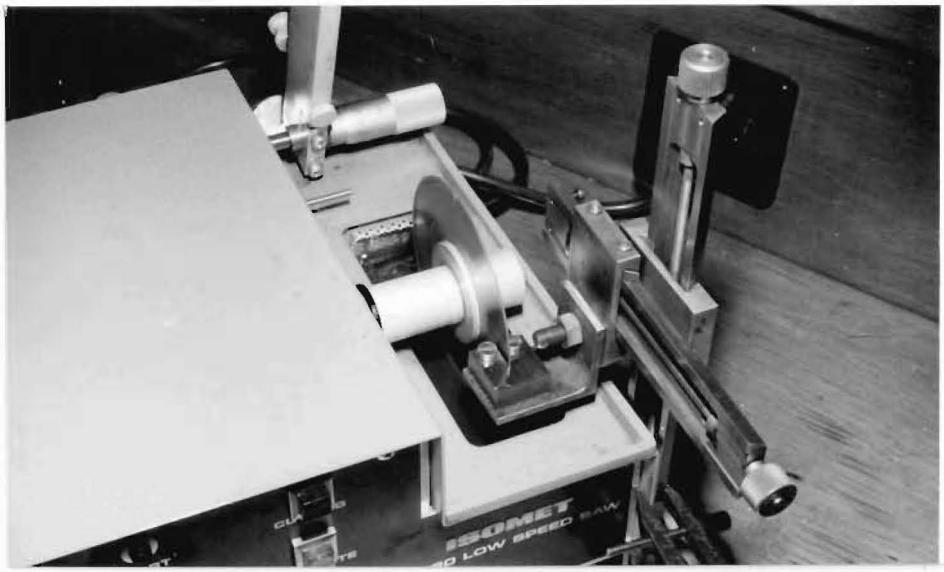

Fig. 56: View of a portion of the coordinating "X-Y beam/column" with 0.3 mm thick diamond wafering blade.

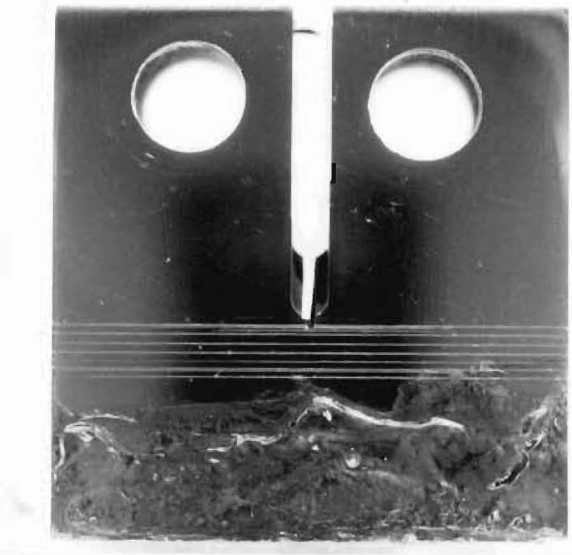

Fig. 57: Scribe marks on the calibration specimen with the scribe marks at 0.4 mm intervals.

The calibration experiment was conducted using the stress corrosion testing rig No. 1 shown in Fig. 38 (section 2.1.2). The CT specimen was coated with silicon lubricant to prevent the corrodent (i.e., 3.5% NaCl solution) attacking the strain gauge-bonding cement. It is important to note that if the aqueous NaCl solution attacked the strain gauge bonding cement, it may effect the gauge resistance and insulation. It follows, therefore, that corrodent attack could affect the compressive back face strain measurements. Silicon lubricant was chosen as the coating medium because of its excellent resistance to the aqueous NaCl solution at ambient temperature.

All of the slot length calibration experiments were conducted at 18° C in 3.5% aqueous NaCl solution. Compressive back face strain measurements were taken after each load increment. For all slot lengths, the strain is linear with the applied load within experimental accuracy, except for very deep slot (or saw cut) in the CT specimen.

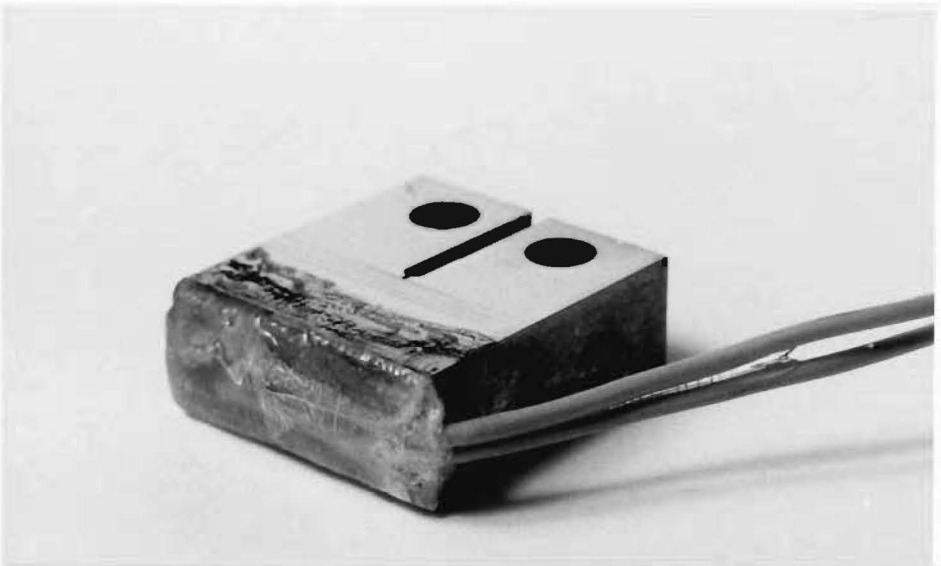

Fig. 58: Calibration-specimen with a strain gauge at the back-face. Heavy consistency silicon lubricant was for use as sealer against the corrodent attack on the strain gauge-bonding cement.

The excitation voltage of the strain indicator was ∿10 Volts d.c. and the out-of-balance voltage was amplified and displayed on a conventional voltmeter attached to the strain indicator. In the experimental work a saw cut was extended from a/W = 0.5125 (a slot length of 10.25 mm) to a/W = 0.7175 (a slot length of 14.35 mm).

3. EXPERIMENTAL RESULTS

3.1 Tests In 3.5% NaCl Solution

The susceptibility curves for the specimens pre-cracked in air with the different dynamic loads are shown in Figs 59 to 64, the results of the specimens with subcritical stress corrosion cracks at the interface are illustrated in Fig. 63 and the results of the specimens fatigue pre-cracked in 3.5% NaCl solution are presented in Fig. 64.

In Table 14 the K_{Iscc} values determined from these different specimens are listed. The value of K_{Iscc} is the value at which no crack growth could be detected after 500 hours.

For the crack length calibration experiments, the relationship between slot length, back face strain and load for the specimen is shown in Figs 65 to 67.

3.1.1 The Results Of The Slot Length Calibration Experiments

Fig. 65 shows the variation in compressive BFS at various constant load conditions with a/W for 10 mm thick CT specimens. It is observed that the strain for all the constant load conditions increases linearly with slot length up to a/W = 0.6. The non-linearity is significant for a/W > 0.6.

The departure from linearity in the 10 mm thick CT speci-

men for a/W > 0.6 was probably due to a departure from linear elastic fracture mechanics (LEFM) validity. It is believed that the thin remaining area in the CT specimen has a high stress concentration at the tip of the saw cut (or slot). This high stress concentration creates a large zone of plastic deformation at the saw cut tip. It causes the calibration experiment to depart from the plane strain condition. The results of similar investigation, also using back face strain gauging, have been reported by Richards and Deans.[80] From the above results, it can be said that all subsequent relationships in this calibration experiment are based on the straight line in Fig. 65.

Since it has been assumed that the straight line relationship between the BFS and a/W for the tested CT specimen for a/W up to 0.6 is not fortuitous, perhaps in future similar studies, it would be preferable to present the results in a form independent of specimen size and Young's Modulus of the material. This suggestion of the previous workers[80] was made to improve the accuracy of the curve by using the extrapolated straight line from Fig. 65, and it was based on a normalising parameter described in reference[80].

Fig. 66 indicates the variation in compressive BFS with load for several values of a/W for a 10 mm thick CT specimen. The strain is linear with load except at very low loads. BFS increases linearly with load over the whole range studied (up to a/W = 0.7175) unlike the curve in Fig. 65.

The variation in compressive BFS with the constant stress intensity (K_I) and a/W for the same specimen is shown in Fig. 67. A linear relationship is also shown in this figure, BFS increases linearly with a/W over the whole range measured (up to a/W = 0.7175).

Table 14 : Influence of pre-crack on K_{Iscc} for ULTIMO 200 steel tested in 3.5% NaCl solution

Test Series No.	Pre-crack Environment	Load Condition for Pre-cracking Process	Final ΔK or K_I ($MN/m^{3/2}$)	% Intergranular at Crack Tip	K_{Iscc} ($MN/m^{3/2}$) Based on 500 Hours
I	air	dynamic	33	90	9.5
II	air	dynamic	20	5	10.8
III	air	dynamic	12	1	9.5
IV	air	dynamic	4	0	8.0
V	3.5% NaCl	static	7	100	9.5
VI	3.5% NaCl	dynamic	20	95	9.5

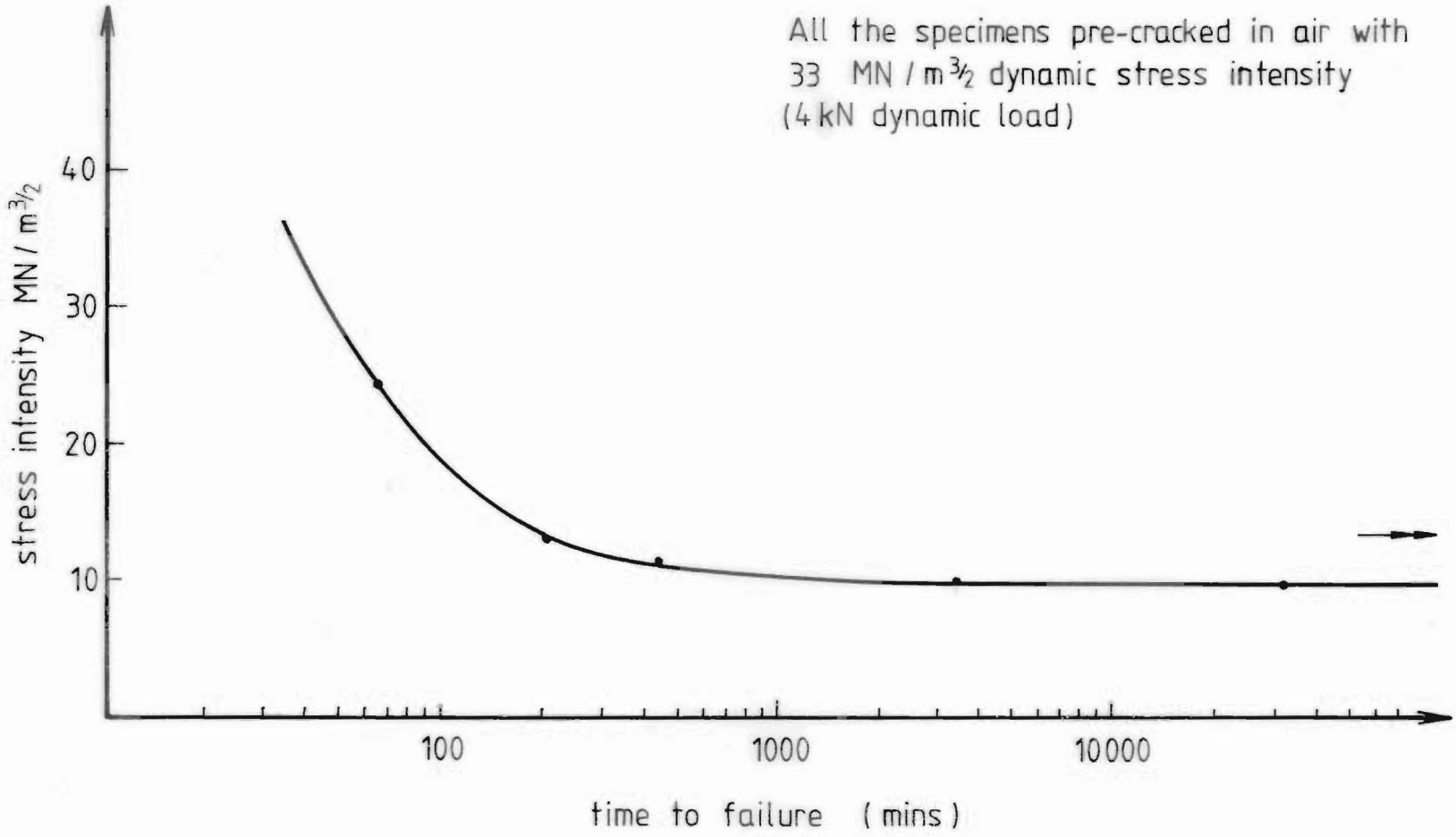

FIG 59 TIME TO FAILURE AS A FUNCTION OF STRESS INTENSITY FOR THE COMPACT TENSION SPECIMEN IN ULTIMO-200-STEEL TESTED IN 3·5% NaCl SOLUTION

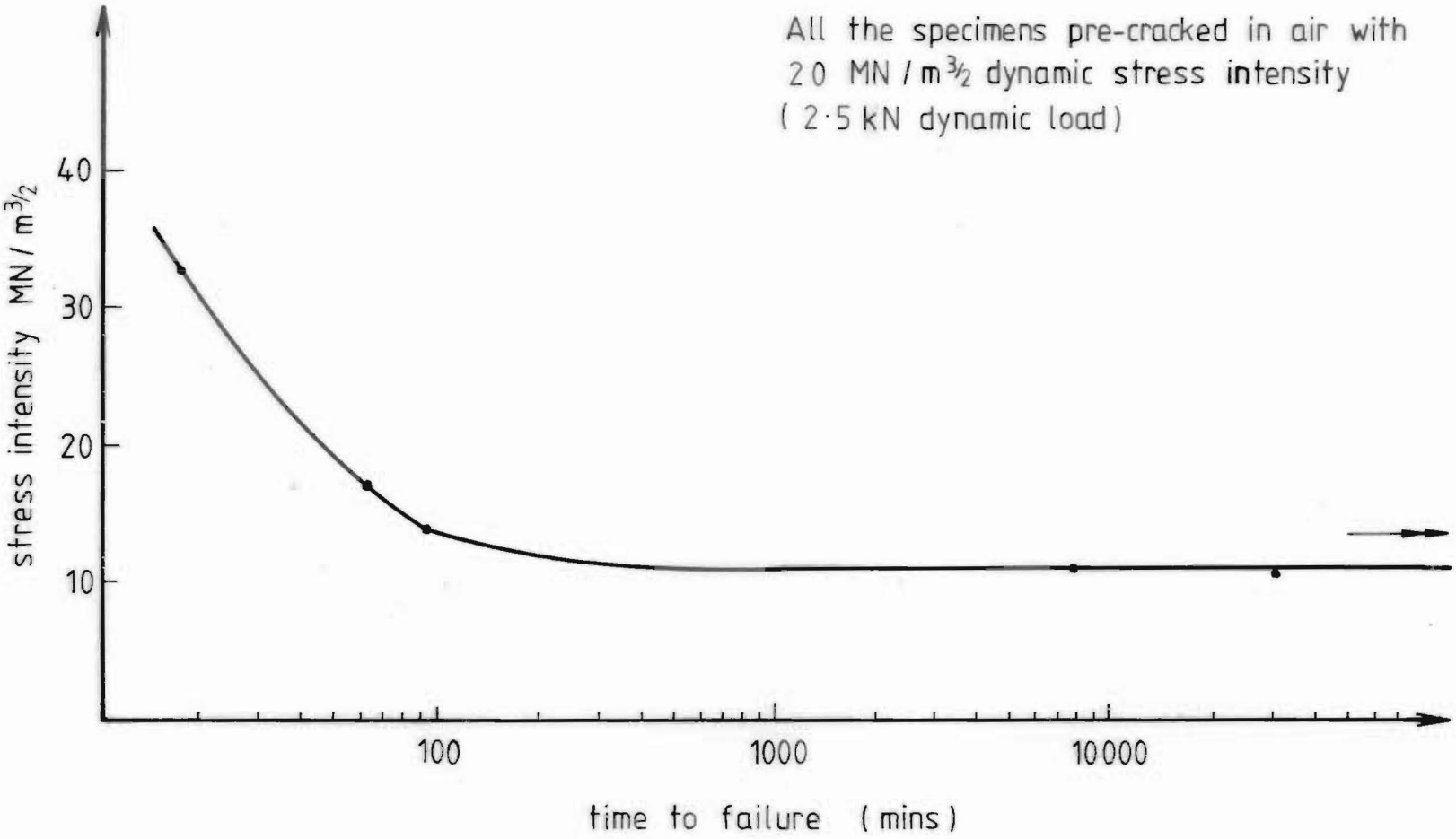

FIG 60 TIME TO FAILURE AS A FUNCTION OF STRESS INTENSITY FOR THE COMPACT TENSION SPECIMEN IN ULTIMO-200-STEEL TESTED IN 3·5% NaCl SOLUTION

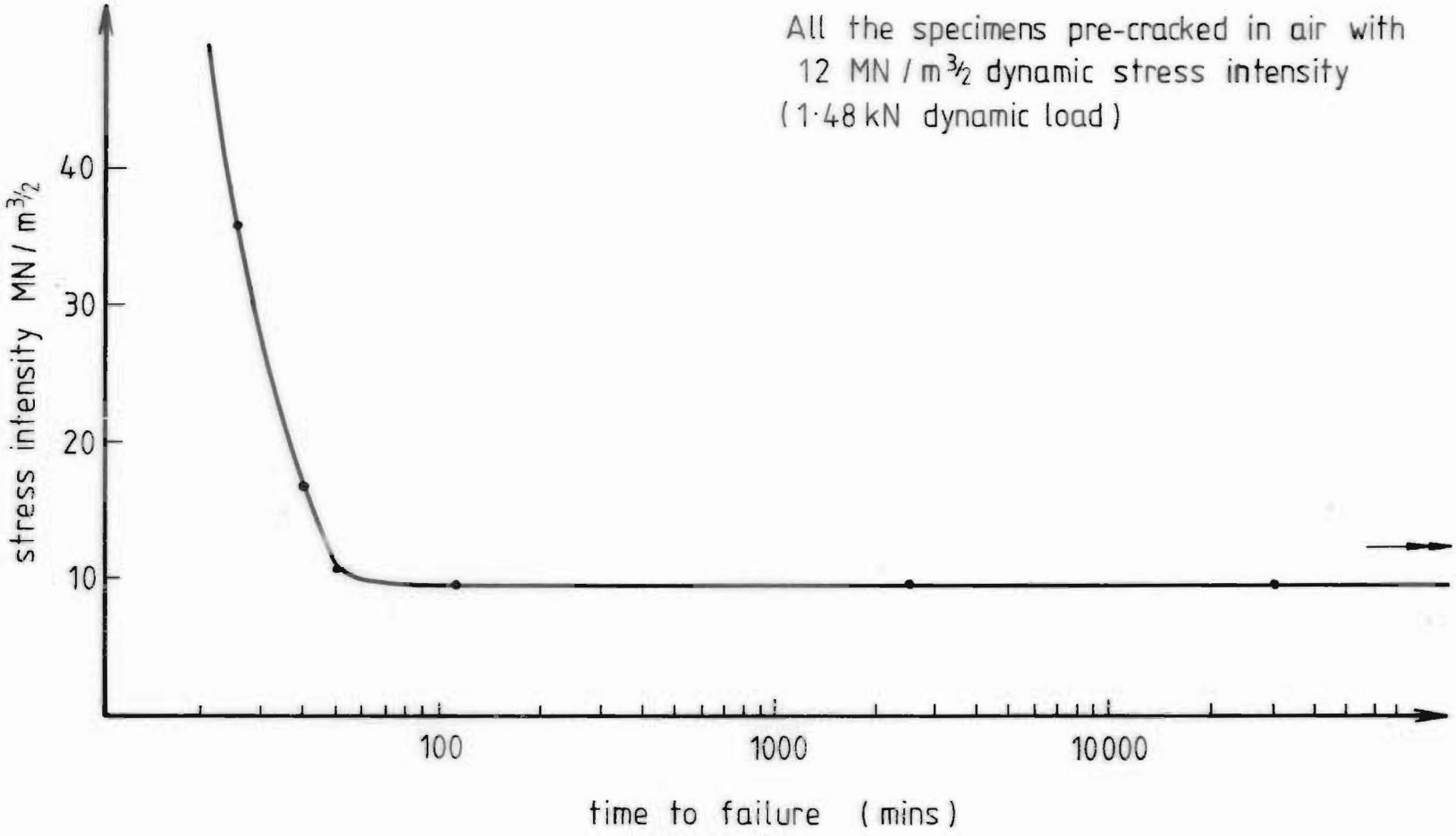

FIG 6.1 TIME TO FAILURE AS A FUNCTION OF STRESS INTENSITY FOR THE COMPACT TENSION SPECIMEN IN ULTIMO-200-STEEL TESTED IN 3·5% NaCl SOLUTION

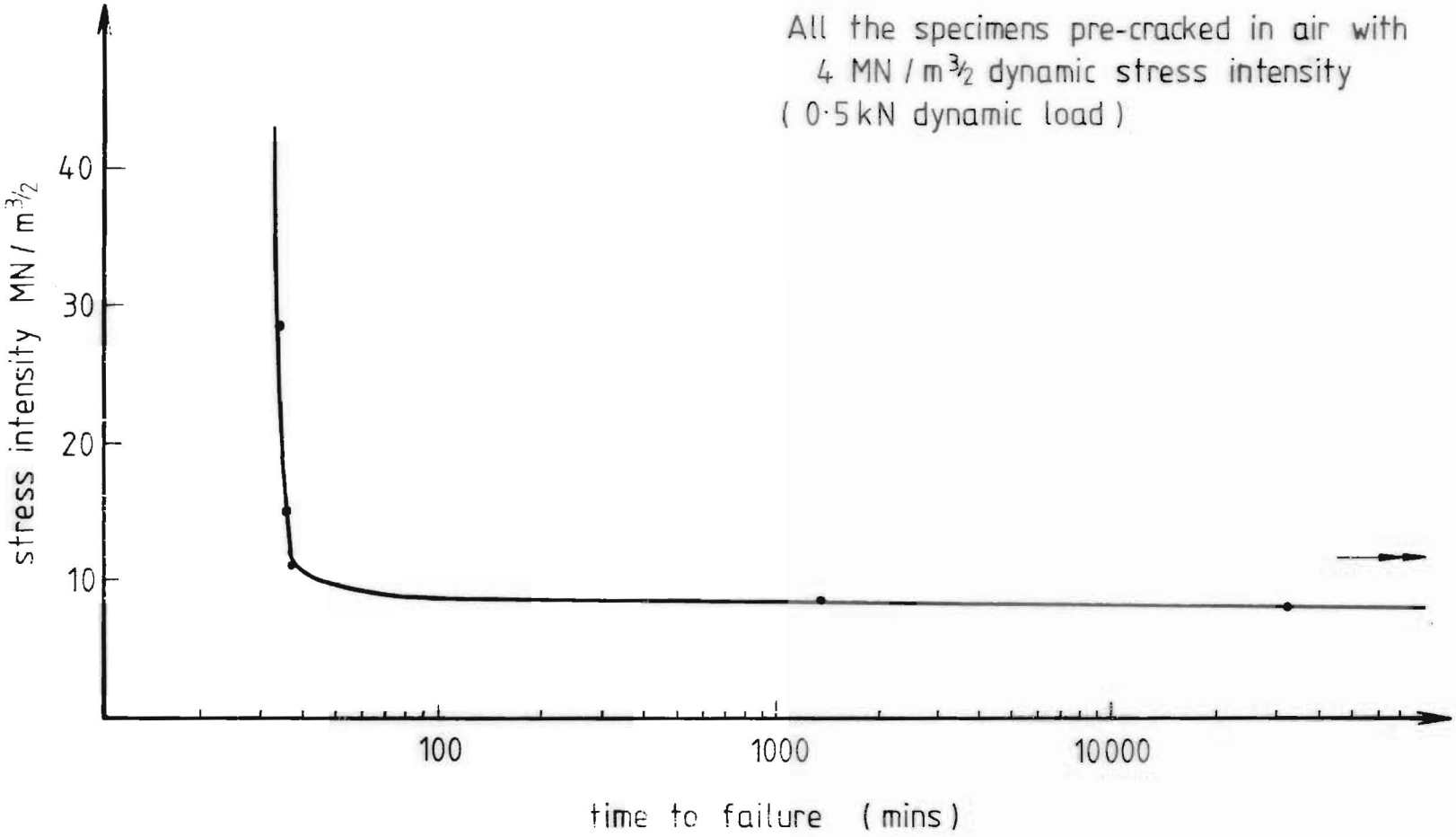

FIG 62 TIME TO FAILURE AS A FUNCTION OF STRESS INTENSITY FOR THE COMPACT TENSION SPECIMEN IN ULTIMO-200-STEEL TESTED IN 3·5% NaCl SOLUTION

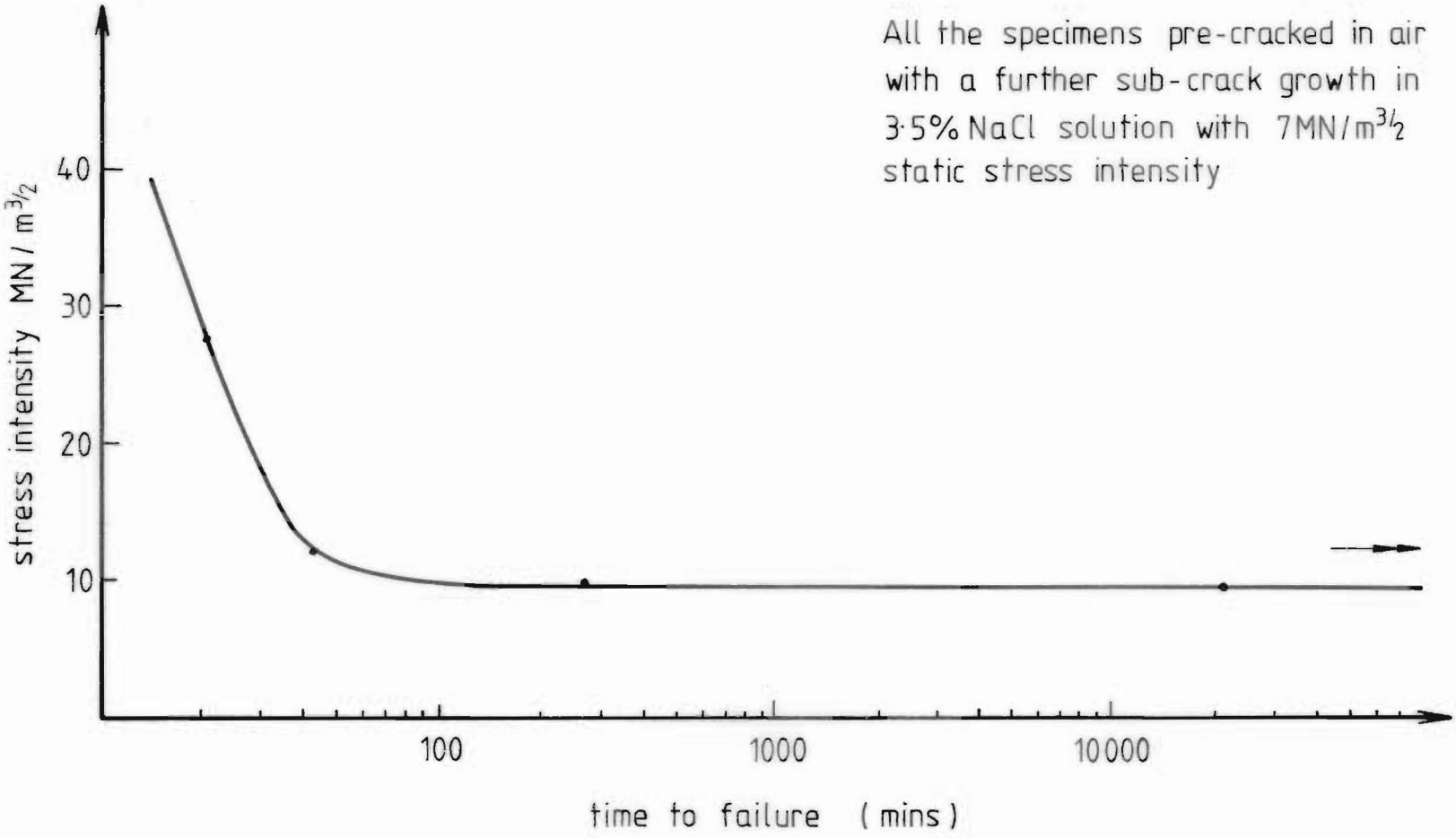

FIG 63 TIME TO FAILURE AS A FUNCTION OF STRESS INTENSITY FOR THE COMPACT TENSION SPECIMEN IN ULTIMO-200-STEEL TESTED IN 3·5% NaCl SOLUTION

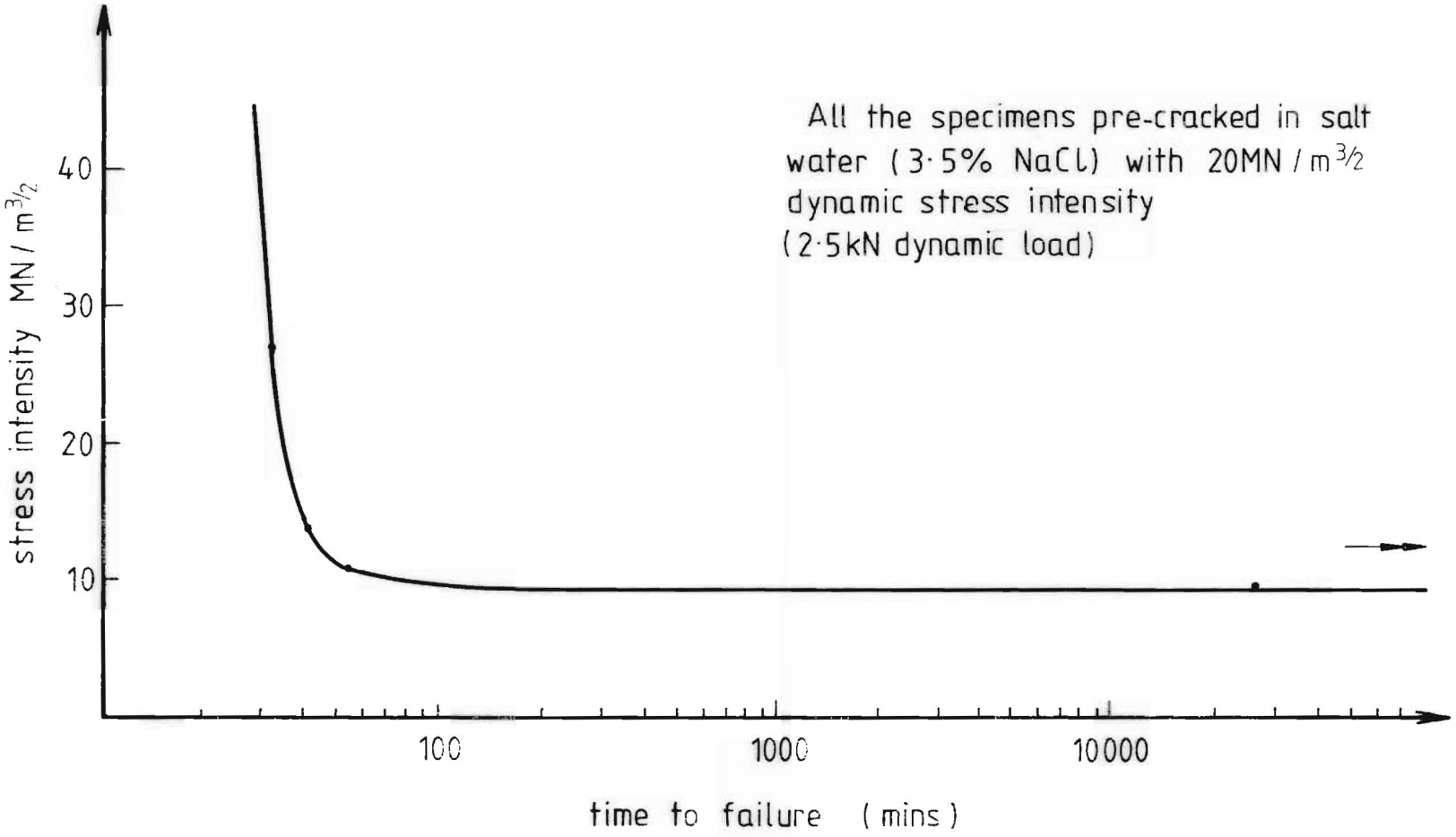

FIG 64 TIME TO FAILURE AS A FUNCTION OF STRESS INTENSITY FOR THE COMPACT TENSION SPECIMEN IN ULTIMO-200-STEEL TESTED IN 3·5% NaCl SOLUTION

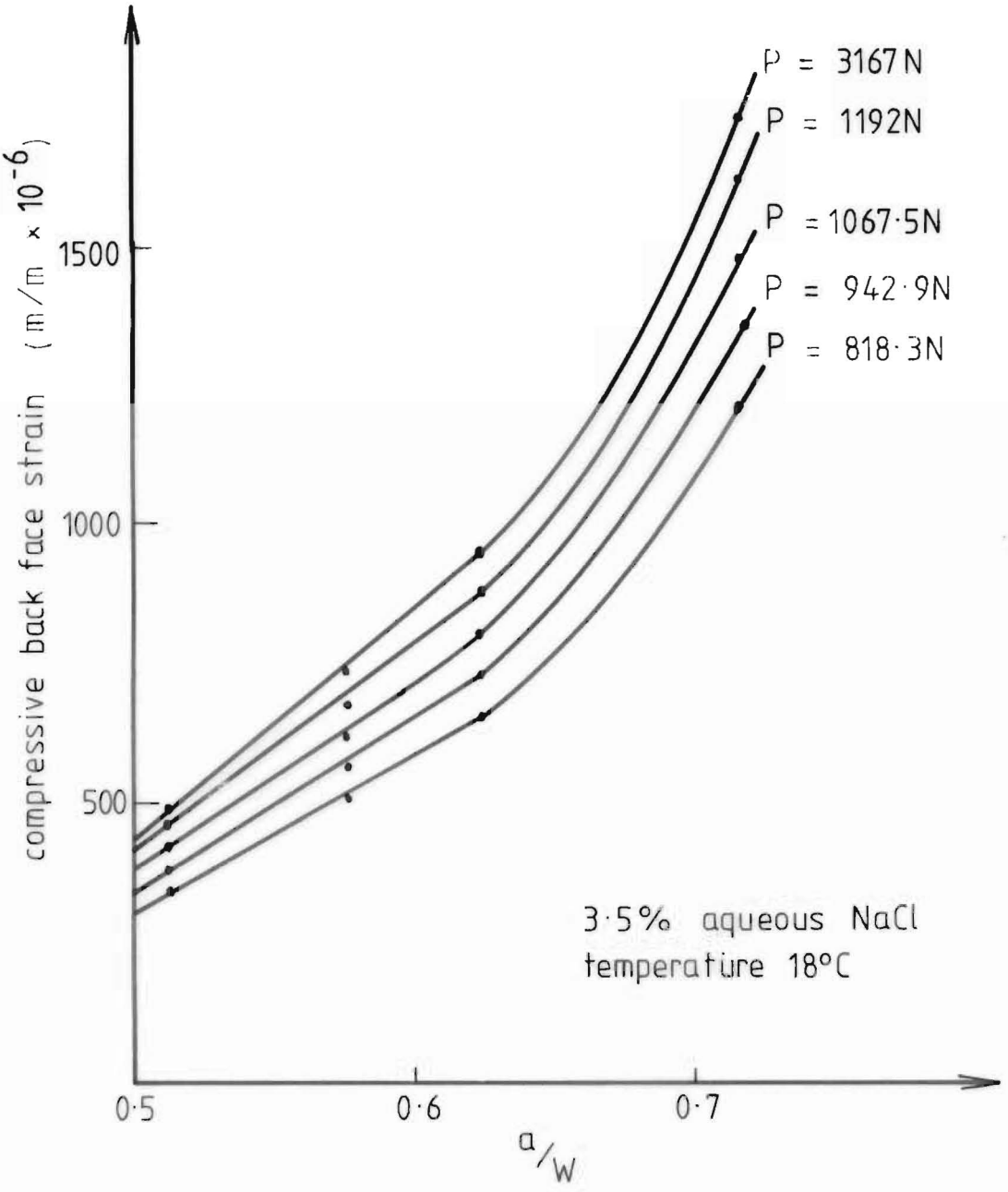

FIG 65 VARIATION IN COMPRESSIVE BACK FACE STRAIN AT DIFFERENT CONSTANT LOAD WITH a/W FOR 10mm CT SPECIMEN

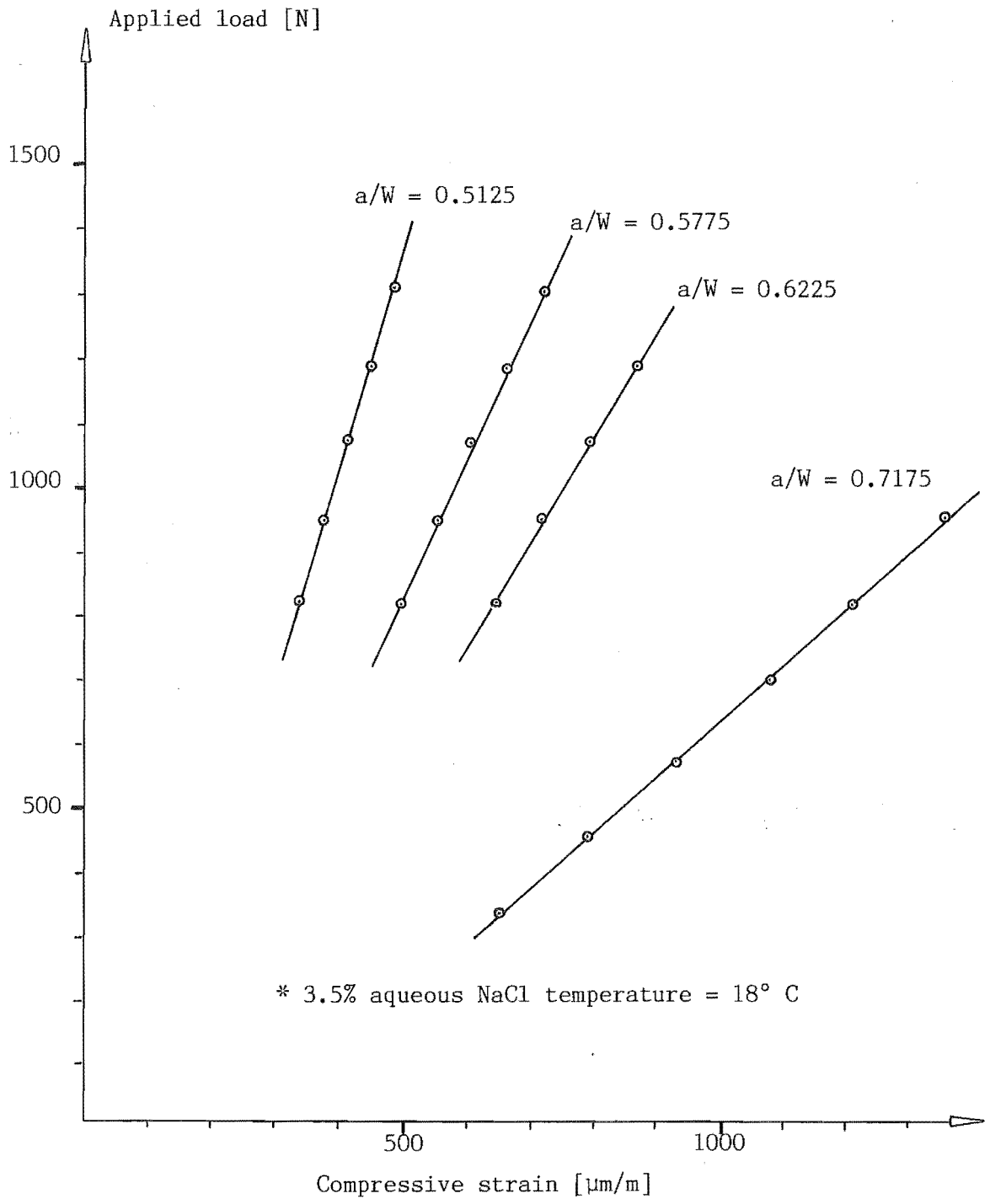

Fig. 66: Compressive Strain on the back face of a 10 mm CT-specimen as a function of load for four different slot lengths. (Chemical environment: 3.5% NaCl solution)

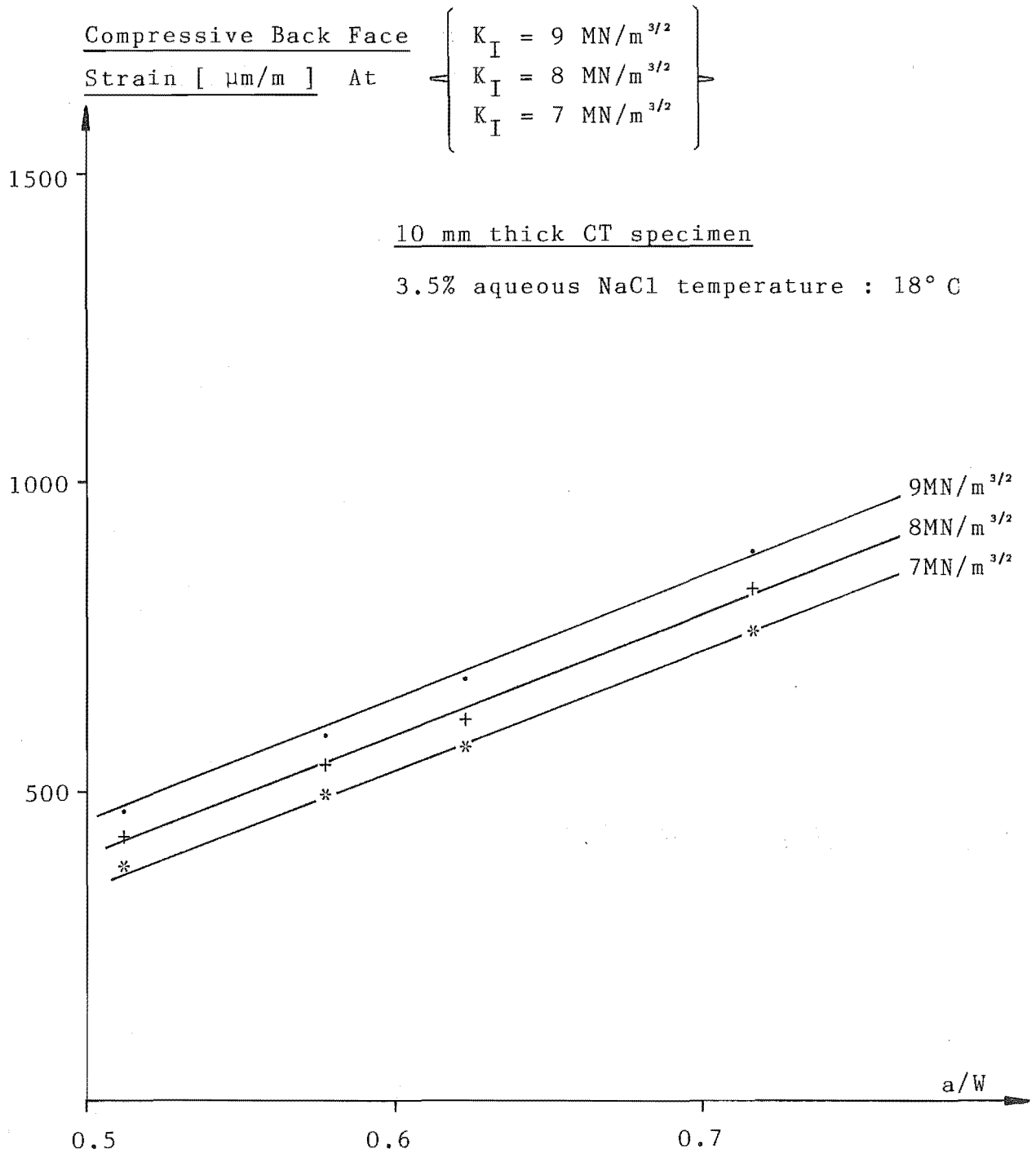

Fig.67: Variation in compressive back face strain with K_I and a/W for 10 mm thick CT specimen.

Table 15: Measurement of slot length, load and strain.

Saw Cut Depth a[mm]	Applied Stress Intensity K_I[MN/m$^{3/2}$]	Strain [m/m•10^{-6}]	Applied Load P_{act} [N]
10.25 mm	9.35	492	1316.7
Y = 10.043	9.1225	484.5	
a/W = 0.5125	8.895	477	
	8.6675	469.5	
	8.44	462	1192
	8.225	453	
	8.01	444	
	7.795	435	
	7.58	426	1067.5
	7.3575	414.5	
	7.135	403	
	6.9125	391.5	
	6.69	380	942.9
	6.47	370	
	6.25	360	
	6.03	350	
	5.81	340	818.3
11.55 mm	11.67	735	1316.7
Y = 12.534	11.3925	720.5	
a/W = 0.5775	11.115	706	
	10.8375	691.5	
	10.56	677	1192
	10.285	662.75	
	10.01	648.5	
	9.735	634.25	
	9.46	620	1067.5
	9.185	605.75	
	8.91	591.5	
	8.635	577.25	
	8.36	563	942.9
	8.0825	548.5	
	7.805	534	
	7.5275	519.5	
	7.25	505	818.3

Table 15: (Contd)

Saw Cut Depth a[mm]	Applied Stress Intensity K_I[MN/m$^{3/2}$]	Strain [m/m•10^{-6}]	Applied Load P_{act}[N]
12.45 mm Y = 14.956 a/W = 0.6225	13.92 13.59 13.26 12.93 12.60	950 932 914 896 878	1316.7 1192
	12.2725 11.945 11.6175 11.29	859.25 840.5 821.75 803	 1067.5
	10.96 10.63 10.30 9.97	784.75 766.5 748.25 730	 942.9
	9.64 9.31 8.98 8.65	711.25 692.5 673.75 655	 818.3
12.45 mm Y = 14.956 a/W = 0.6225	8.65 8.3225 7.995 7.6675 7.34	655 636.25 617.5 598.75 580	818.3 693.74
	7.01 6.68 6.35 6.02	561.5 543 524.5 506	 569.15
	5.69 5.36 5.03 4.70	486.5 467 447.5 428	 444.65

Table 15: (Contd)

Saw Cut Depth a[mm]	Applied Stress Intensity K_I[MN/m$^{3/2}$]	Strain [m/m•10^{-6}]	Applied Load P_{act} [N]
14.35 mm Y = 23.727 a/W = 0.7175	20	1629	1192
	19.475	1594.5	
	18.95	1560	
	18.425	1525.5	
	17.9	1491	1067.5
	17.38	1455.75	
	16.86	1420.5	
	16.34	1385.25	
	15.82	1350	942.9
	15.2975	1315.5	
	14.775	1281	
	14.2525	1246.5	
	13.73	1212	818.3
	13.2075	1177	
	12.685	1142	
	12.1625	1107	
	11.64	1072	693.74
	11.1175	1037	
	10.595	1002	
	10.0725	967	
	9.55	932	569.15
	9.0275	897.5	
	8.505	863	
	7.9825	828.5	
	7.46	794	444.55
	6.9375	760	
	6.415	726	
	5.8925	692	
	5.37	658	319.96
	22.09	1742	1316.7

As we can see in the Table 15, in some of the slot length calibration tests, the K_I value was well above K_{Iscc}. Note that, the notch root radius of the chevron notch in the CT specimen was equal to or greater than 0.3 mm. It is important to recognize that a chevron notch of large root radius (e.g., ρ = 0.3 mm) would blunt the notch. Accordingly, it would minimize the opportunity for plastic instability to develop. Therefore, the existing notch of large root radius would reduce the possibility that the slot could have been extended by SCC occurring whilst the worker was doing calibration.

Moreover, it should be emphasized that, for the slot length calibration tests at a high level of stress intensity (K_I), the tests were usually completed in less than 10 minutes. Hence, it is believed that, in such a short period , the occurrence of SCC during the tests was not realistic (see Figs 59 to 64).

4. DISCUSSION OF RESULTS

4.1 Metallography And Fractography

Optical and electron microscopy were used to study the microstructure and crack paths in fractured specimens for features which could be attributed to the use of the different pre-crack environments and load conditions for the pre-cracking.

4.1.1 Fracture Surfaces

The fracture surfaces of all specimens had similar characteristics (Figs 68 & 69).

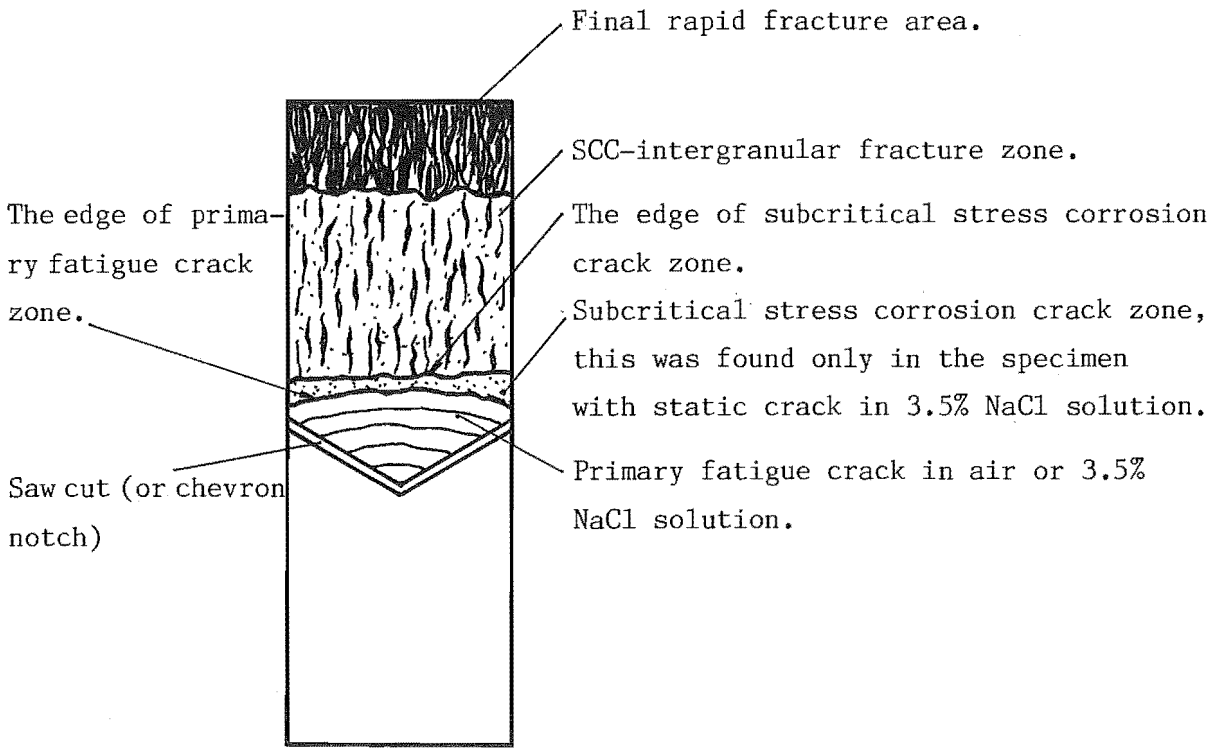

Fig. 68: Schematic representation of typical fracture surface

Fig. 69: SEM fractograph, 18x fracture caused by a portion of an old stress corrosion crack (the thin broken white line prior to SCC - intergranular fracture zone) that initiated in 3.5% NaCl solution with 444 N static load for 1054 hours.

As shown in Figs 68 and 69, three distinct zones were evident, namely, (i) the primary fatigue crack or subcritical corrosion crack, (ii) SCC - intergranular fracture zone, and (iii) the final rapid fracture zone.

The limits of the primary crack were usually readily discernible for the specimens pre-cracked in air or for the specimens pre-cracked in air with subcritical stress corrosion crack growth in 3.5% NaCl solution.

The subcritical stress corrosion cracks originated at the edge of the primary fatigue crack zone (see Figs 68 and 69). Critical examination of the fracture surfaces, particularly at the edge of the subcritical stress corrosion crack zone, showed that the re-initiation of the stress corrosion cracks from the old stress corrosion cracks followed clearly on intergranular paths (See Figs 78 and 79).

The secondary failure zone, produced by ultimate rapid fracture of the specimen, was partly fibrous and partly shear, the area of this latter region increasing with increasing applied stress intensity due to the smaller loading cross area. Localized yielding was evident at the specimen surface. The ductile nature of fibrous area is similar to those specimen fractured by tension overload (Fig. 51) in air.

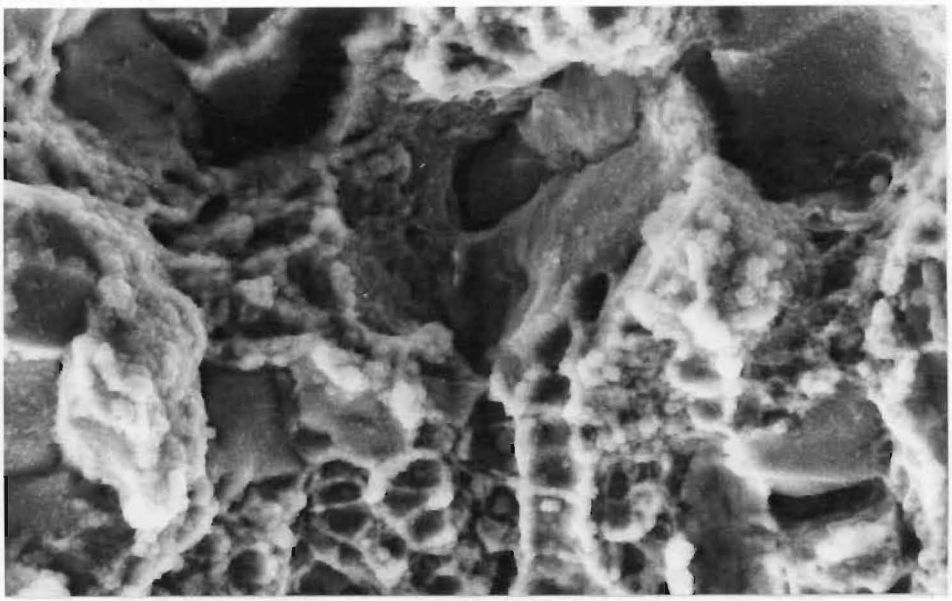

Fig. 70: SEM fractograph of secondary failure area, showing ductile dimples, at 4000x.

4.1.1.1 Comments On Subcritical Stress Corrosion Cracks

It is important to note that the value K for the formation of subcritical stress corrosion curves is (section 2.7.2) roughly equal to the values of K_{Iscc} (section 3.1, test series IV). The significance of this is discussed below.

(i) The specimens used for test series No. I were statically pre-stressed in saline at values of stress intensity close to K_{Iscc} and showed very slow crack growth. For example: Specimen 24 (section 2.7.2) was statically pre-stressed in saline solution with a load of 942.9 N, it produced a crack

growth of 0.25 mm in 289 hours. Due to limited time, the specimens of this nature were used for test series V.

(ii) Since the pre-crack was identical in appearance to the stress corrosion crack which propagated from it, it was very difficult to measure the exact length of the crack. It would appear more appropriate to use the BFS technique (Sect. 2.10.1) to enable the initial stress intensity to be accurately determined.

4.1.2 Fractographic Observations

The fracture surfaces of the different specimens which had failed in 3.5% NaCl solution are shown in Figs 71 to 81. All the SCC-cracks were wholly intergranular, following the grain boundaries, and there were no significant differences associated with the operating load conditions.

Specimen pre-cracked in air with $\Delta K = 33\ MN/m^{3/2}$

Specimen I.D: No. 29

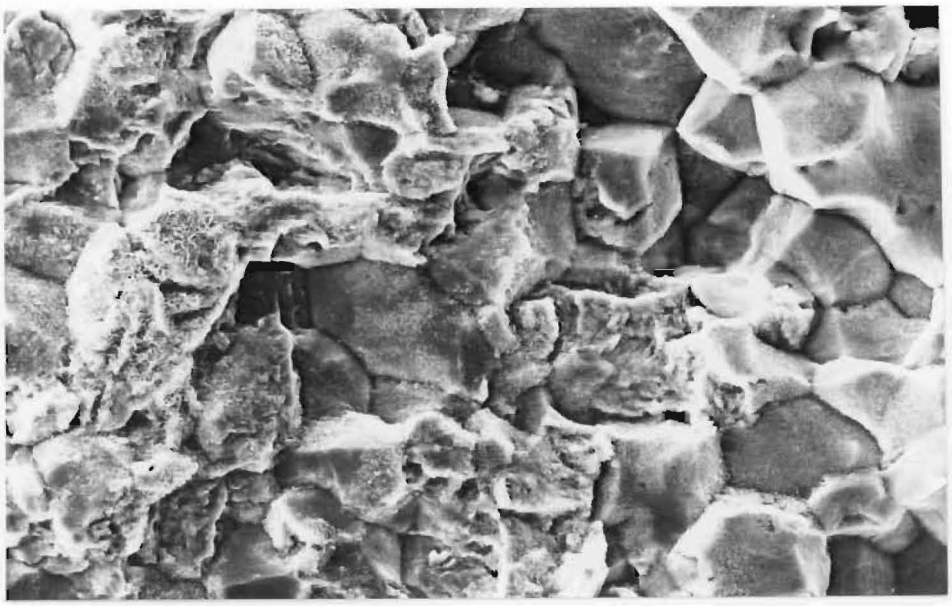

Fig. 71 : A SEM fractograph, at 800 x, of a section close to fracture interface (fatigue crack at left) in a specimen pre-cracked in air with 4 KN dynamic load, and fractured by a stress intensity of 10.3 $MN/m^{3/2}$, showing about 70% of intergranular crack at transition.

With assistance from local hydrogen pressure, the microvoids or small holes tend to link together (as indicated by arrows) to form the intergranular cracks (IG_{HE}) along the grain boundaries.

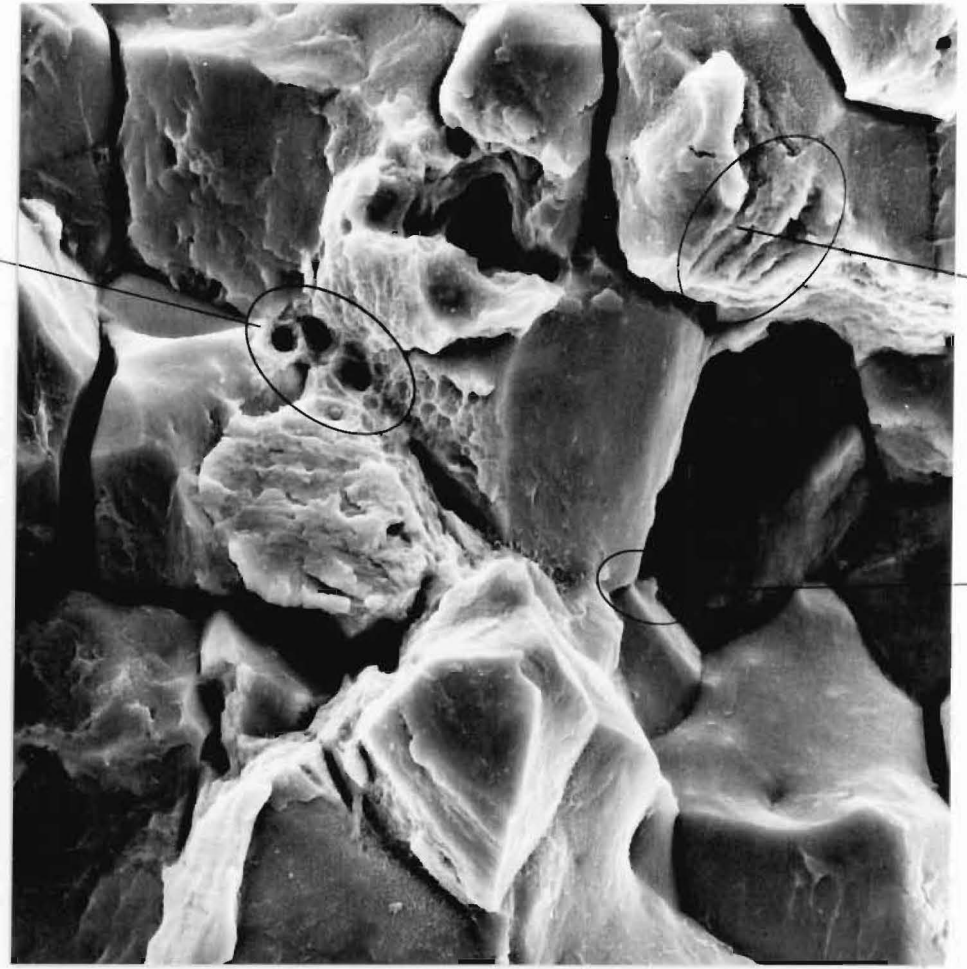

Microcracks (or subcracks) along the lath boundaries.

Tear ridges (or tongue like pattern).

Fig. 72 : The appearance of the fracture surface at the stress corrosion region as seen in Fig. 71, at 2000 x.

Fig. 73 : The appearance of the fracture surface at the fatigue region as seen in Fig. 71, at 2000 x.

Specimen pre-cracked in air with $\Delta K = 20\ MN/m^{3/2}$

Specimen I.D: No. 3

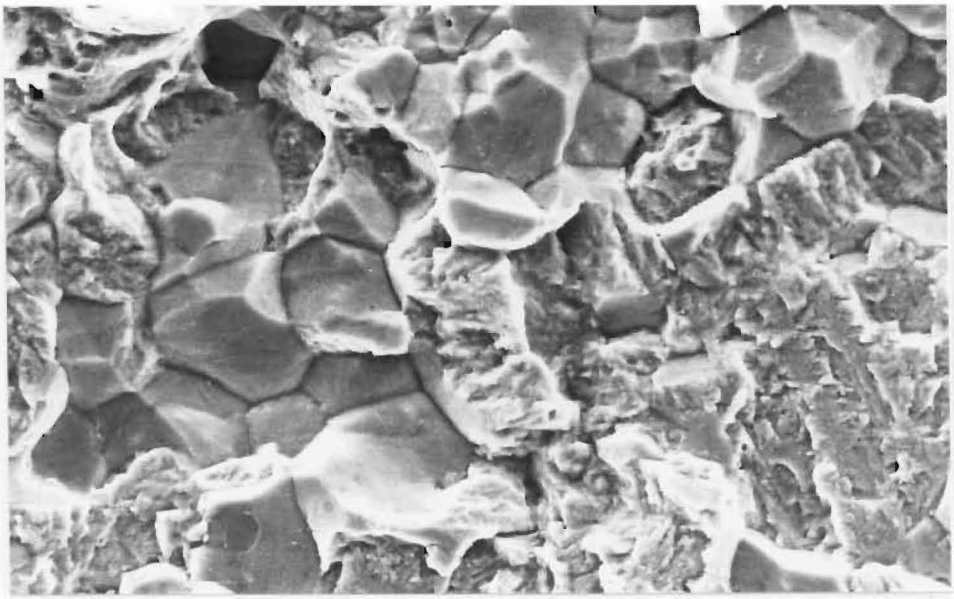

Fig. 74 : Fatigue crack to stress corrosion crack transition in a specimen with 2.5 KN dynamic pre-crack load, showing about 5% intergranular fatigue crack (at the right corner) at transition, 800x.

Specimen pre-cracked in air with $\Delta K = 12\ MN/m^{3/2}$

Specimen I.D. : No. 8

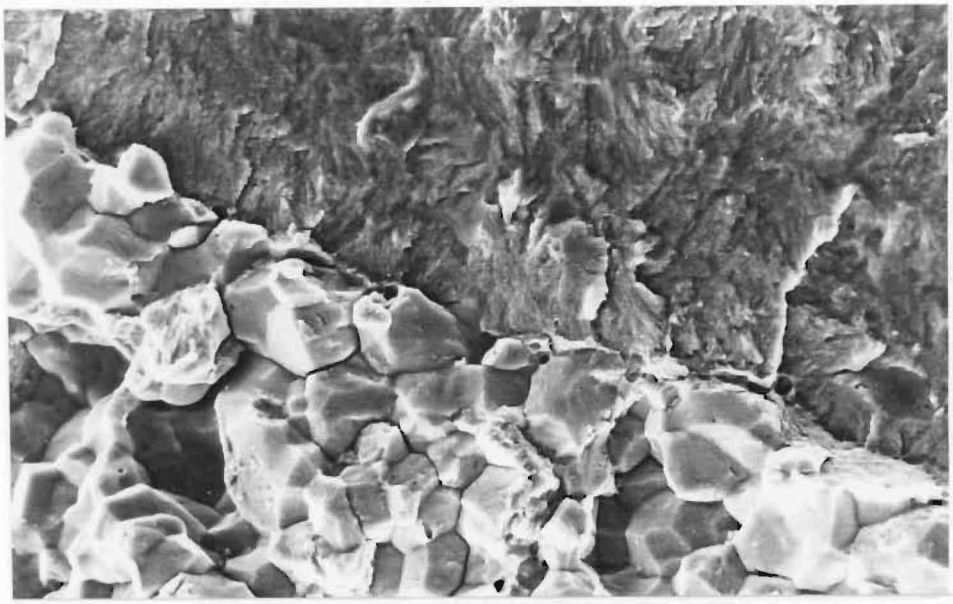

Fig. 75 : Fatigue stress corrosion interface in a specimen of ULTIMO 200 steel pre-cracked in air with 1.48 KN dynamic load, and fractured by stress corrosion in 3.5% NaCl solution,showing about 1% of inter-granular crack at transition, 800 x.

Specimen pre-cracked in air with $\Delta K = 4\ MN/m^{3/2}$

Specimen I.D. : No.19

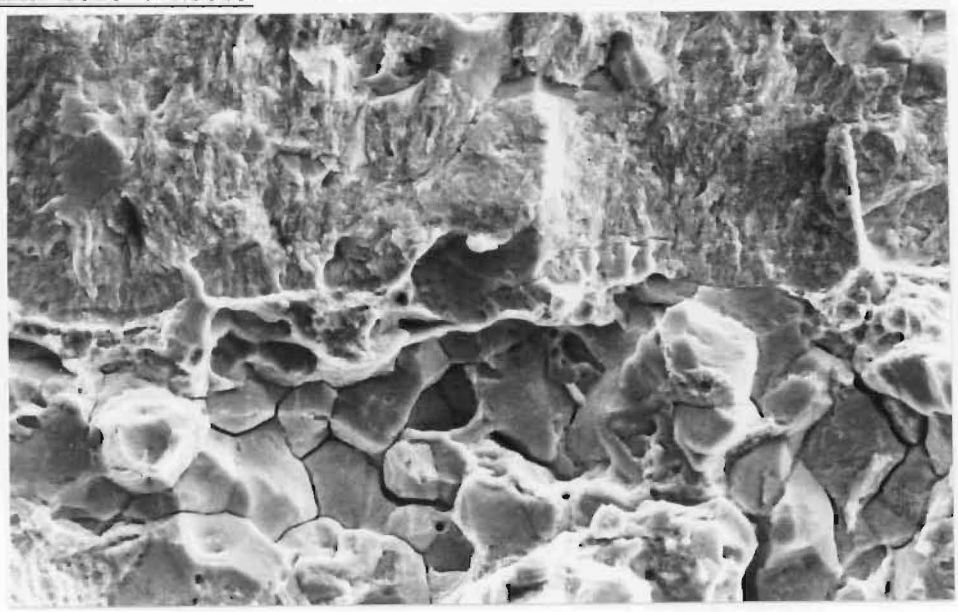

Fig. 76 : Fatigue stress corrosion interface in a specimen pre-cracked in air with 0.5 KN dynamic load, and fractured by a load of 3559.4 N, showing clear transgranular (~100%) crack at fatigue region, at 800 x.

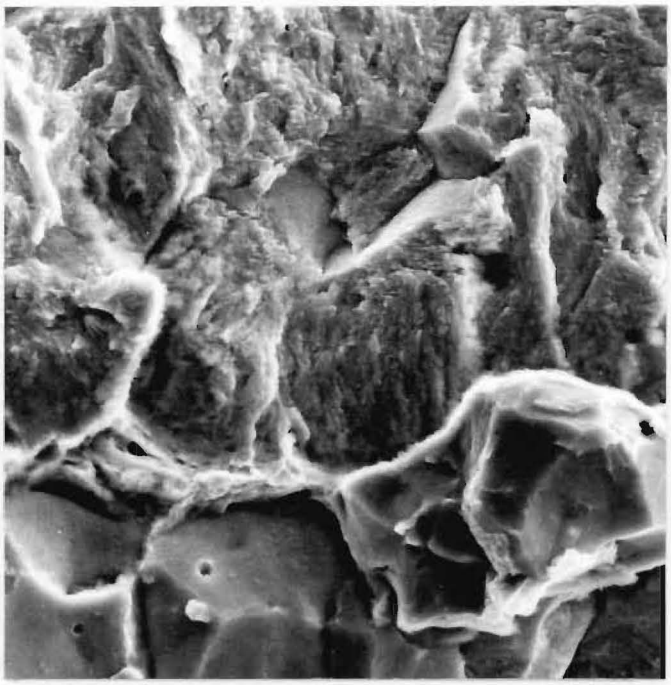

Fig. 77 : The appearance of the fracture interface as seen in Fig. 76, at 2000 x.

Specimen with sub-crack growth in 3.5% NaCl solution

Specimen I.D: No. 6

Fig. 78 : A SEM fractograph, at 800 x, of a section close to fracture interface (subcritical corrosion crack at top) in a specimen of ULTIMO 200 steel fractured in 3.5% NaCl solution, showing a branching stress corrosion crack with ∿100% intergranular fracture at trasition.

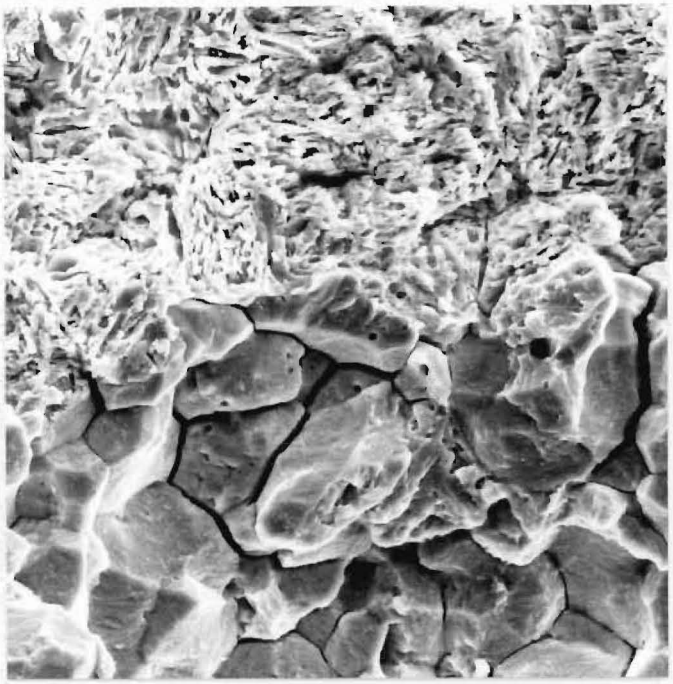

Fig. 79 : The appearance of the fracture interface as seen in Fig. 78, at 1600 x (N.B., crack growth direction is from top to bottom, the micrograph of hydrogen induced cracking is illustrated at the bottom section).

Specimen pre-cracked in 3.5% NaCl solution with $\Delta K = 20\ MN/m^{3/2}$

Specimen I.D: No. 36

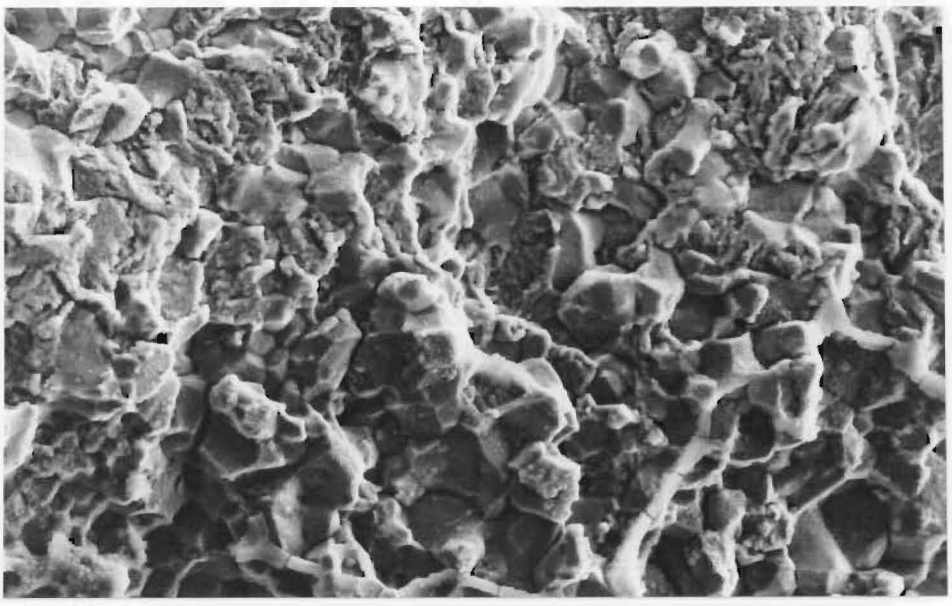

Fig. 80 : Fatigue stress corrosion interface in a specimen of ULTIMO 200 steel pre-cracked in 3.5% NaCl solution with 2.5 KN dynamic load, and fractured by stress corrosion in 3.5% NaCl solution, showing about 95% intergranular crack at transition, at 470 x.

Fig. 81: The appearance of a similar fracture interface to that seen in Fig. 80, at 800 x.

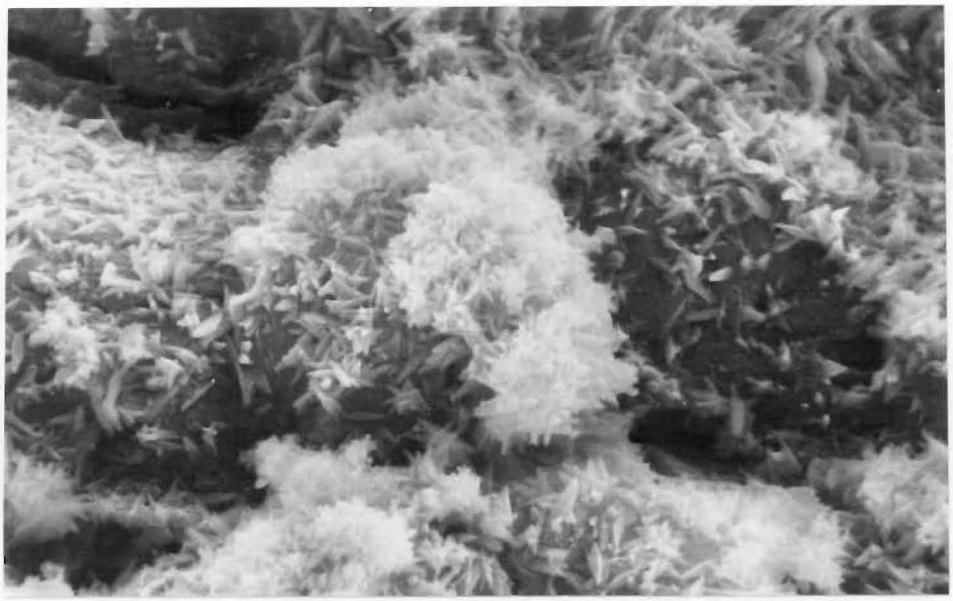

Fig. 82: Micrograph, at 3300 x, the final fracture surface shows the corrosion products on it. The layer of corrosion products sometimes makes it difficult to determine the mechanics of fracture.

4.1.3 Metallographic Observations

The MnS inclusions could be distinguished easily from the optical micrograph by their large size, and are shown in Figs 83 & 84.

Fig. 83: Optical micrograph of ULTIMO 200 tempered at 350° C, showing fine tempered martensitic structure and elongated sulphide inclusions on the etched surface (3% Nital), at 600 x.

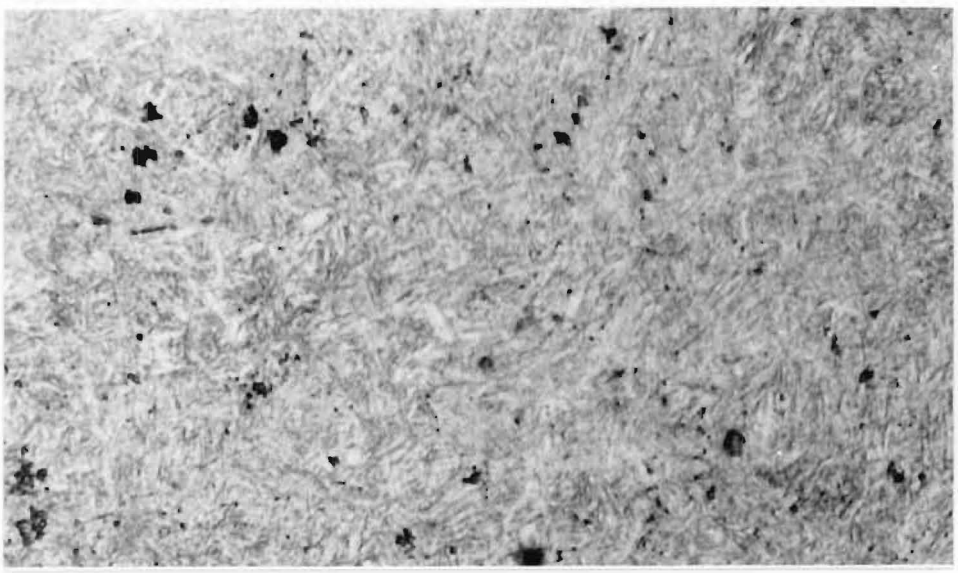

Fig. 84: Metallograph, at 600 x, of a nital etched section in a 10 mm thick specimen, showing the MnS inclusions on the etched surface (3% nital).

4.2 DISCUSSION

The observations shown in Table 14, Figs 59 to 64, and Figs 71 to 82, immediately established four significant points:-

(A) For the specimens with principally transgranular cracking at the tip of the pre-crack

(i) As the dynamic stress intensity used for pre-cracking in air is decreased the amount of intergranular fracture decreases. For a final ΔK of 33 $MN/m^{3/2}$, 90% of intergranular facets at the crack tip were observed.

(ii) For propagation from pre-cracks which were principally transgranular in nature, the threshold stress intensity decreases as the dynamic stress intensity used for pre-cracking decreases. The value of K_{Iscc} was found to be reduced from 10.8 $MN/m^{3/2}$ to 8 $MN/m^{3/2}$ as the value of ΔK was reduced from 20 $MN/m^{3/2}$ to 4 $MN/m^{3/2}$. These results are probably dependent on the plastic zone-size at the crack tip. According to linear elastic fracture mechanics, the radius of the plastic zone is directly proportional to ΔK^2, if the yield strength of the specimen is constant. This trend means that blunting at the fatigue crack tip is increased by increasing the dynamic stress intensity for the pre-crack.

(B) For the specimens with principally intergranular cracking at the tip of the pre-crack

(i) Comparing the amount of intergranular fracture at the tip of the pre-crack in the test series No's I, V and VI with those of the test series No's II, III and IV, the results suggested that:

(a) The greater the proportion of intergranular cracking at the final portion of the tip of the pre-crack the easier is the initiation of an intergranular stress corrosion crack. However, the lowest K_{Iscc} was obtained with the lowest ΔK (=4 $MN/m^{3/2}$) & entirely transgranular pre-crack.

(b) The specimens pre-cracked in air/saline solution using the same final ΔK (Test series No.'s II and VI, ΔK = 20 $MN/m^{3/2}$) gave different threshold stress intensities. The results suggested that the specimens pre-cracked in saline solution with principally intergranular cracking at the tip of the pre-crack have a lower threshold value than those pre-cracked in air with principally transgranular cracking at the tip of the pre-crack.

(c) The saline solution at the crack tip during the pre-cracking process might cause a higher dynamic stress intensity (because salt water is incompressible and air is compressible) at the tip of the pre-crack. The effect of the plastic deformation caused by the higher stress intensity on the value of K_{Iscc} would be insignificant for specimens with principally intergranular cracking at the tip of the pre-crack. Indeed, the molecular hydrogen gas pressure within the voids in the plastic zone just ahead of a crack tip is considered to have a more significant effect than that of saline solution at the crack tip.

(ii) The fractographic evidence presented in Figs 78 - 81 shows that the amount of intergranular fracture at the tips of the pre-cracks for both pre-crack load conditions (Test series No's V and VI) are almost the same with 3.5% NaCl solution as the pre-crack environment.

(C) For all the specimens

The most significant finding in this research is that the intergranular stress corrosion cracks would propagate more easily from an existing crack of similar nature (i.e., principally intergranular), rather than from a principally transgranular crack. A previous well-documented observation [17] suggested that intergranular stress corrosion cracks propagating from a transgranular fatigue crack would cause crack arrest due to microbranching which exhibited crack blunting and a reduction in effective crack tip stress intensity. However, in the present research the intergranular hydrogen embrittlement cracks would propagate most easily from an existing crack of entirely transgranular (produced by the lowest ΔK with a minimum plastic blunting at the fatigue tip) and the crack arrest due to microbranching would appear not to be so significant.

(D) Embrittlement of grain boundaries

The fractographic results presented in section 4.1.2 are associated with cracking of ULTIMO 200 steel in 3.5% NaCl solution from the primary crack zones to the SCC-intergranular fracture zone. The stress corrosion cracks illustrated in the Figures 71, 72, 74, 75, 76, 78, 79, 80 and 81 are accompanied by a significant amount of microbranching.

Critical examination of the fracture surfaces has shown that the stress corrosion cracks followed clearly along prior-austenite grain boundaries. The crack path is almost entirely intergranular with small amount of transgranular quasi-cleavage within the prior-austenite grains.

Since the occurrence of intergranular separation along

prior-austenite grain boundaries and transgranular quasi-cleavage within the prior-austenite grain boundaries are essentially the same as the fracture surface morphology of AISI 4340 steel specimens tested in hydrogen gas and in hydrogen sulphide gas (H_2S)[9, 33, 67], it follows, therefore, stress corrosion cracking of high strength steel is likely due to hydrogen embrittlement.

5. CONCLUSIONS

The susceptibility to hydrogen-assisted cracking in high strength steel, as characterized by K_{Iscc}, is related directly to the fracture mode of the crack tip. The results suggested that:-

(1) For the crack propagation of SCC from a fatigue pre-crack which is principally transgranular, K_{Iscc} decreases as the final ΔK for pre-cracking is decreased.

(2) For the crack propagation from a pre-crack with significant intergranular fracture, K_{Iscc} is higher than for an entirely transgranular pre-crack, correspondingly the final ΔK for pre-cracking is higher.

(3) The blunting at the fatigue tip dominates the value of K_{Iscc}, when the amount of transgranular fracture at the tips of pre-crack is significant. The value of K_{Iscc} is increased, when the fracture mode is from a principally transgranular pre-crack to an intergranular stress corrosion crack. The value of K_{Iscc} is decreased again, when the fracture mode is from a principally intergranular pre-crack to an intergranular stress corrosion crack.

(4) Stress corrosion cracking of ULTIMO 200 steel in 3.5% NaCl solution is likely due to hydrogen embrittlement. The crack path follows predominantly along prior-austenite grain boundaries, with a small amount of quasi-cleavage, at low corrodent temperature.

5.1 Suggestions For Further Work

There are many factors which may affect the crack propagation rate of stress corrosion mechanism. Starchak and Kosukhina[81] have investigated recently the role of hydrogen in stress corrosion cracking of steel due to hydrogen sulphide in inhibited and uninhibited solutions of hydrochloric acid saturated with hydrogen sulphide; Bandyopadhyay[33] has studied the effects of composition, yield strength, and H_2 pressure in hydrogen-induced cracking in 4340-type steel. All these studies were undertaken to gain more understanding of hydrogen embrittlement of steel. The results of this project suggested the intergranular hydrogen embrittlement cracks can propagate more easily from an existing crack of similar nature (i.e., principally intergranular), rather than from a principally transgranular crack. But the lowest K_{Iscc} was obtained with the lowest ΔK & entirely transgranular pre-crack. Comparing with available references [9, 33, 67, 68, 74, 78] on sustained loading tests under stress corrosion conditions, it would appear that the relationship between crack initiation and propagation depends largely on the relevant experimental conditions. Hence, recommendations for further studies resulting from this report include:

1) Bandyopadhyay and co-workers[33] stated that Mn and Si would promote the segregation of P and S to the prior austenite grain boundaries and reduce K_{Iscc} values in AISI 4340 type high strength steel. Their measurements of the threshold stress intensity for hydrogen-induced cracking were made in gaseous hydrogen. The gas pressure was varied from 0.03 to 0.22 MPa at 23° C.

K_{Iscc} is not a universal constant, and it is dependent on the initial K (i.e., pre-crack load conditions) and on the material/environment condition. Therefore, it would be interesting to test the fatigue pre-cracked specimens of ULTIMO 200 steel in saline solution with varied combinations of Mn and Si-contents. It is believed that the further study might

enable more understanding to be gained of the compositional effects on stress corrosion cracking of high strength alloy steels.

2) To test ULTIMO 200 steel in other corrosive environments:

The concept of solution specificity for stress corrosion cracking remains in the sense that not all corrodents towards a particular metal promote stress corrosion failure. Indeed, there is circumstantial evidence suggesting the selection of a particular alloy for use in different environments could result in unexpected service failure. Therefore, it is suggested:-

I) To test ULTIMO 200 steel in 46% NaOH at a temperature of the order of 140° C.

Parkins[82] has illustrated the effects of alloying elements in ferritic steels by experimental data. It is reported that, for the stress corrosion tests in a sodium carbonate (Na_2CO_3) and sodium bicarbonate ($NaHCO_3$) solution of steels containing chromium, nickel or molybdenum additions, each alloy addition is beneficial in comparison with the unalloyed carbon steel, particularly the molybdenum addition. From the results of equivalent tests in a sodium hydroxide (NaOH) solution, it is clear that the chromium and nickel additions continue to show benefits. However, the molybdenum containing steel is appreciably more susceptible to cracking in sodium hydroxide solution than the unalloyed steel. Clearly, a molybdenum addition is seen to be beneficial in one environment but deleterious in other.

Based on the above considerations, therefore, it would be worthwhile comparing Parkins's results with the caustic embrittlement of high strength steel. It is noted that the 46% NaOH solution is chosen because this hot caustic solution could be conducted at the atmospheric boiling point, where

simple equipment (as compared with stress corrosion tests in pressurized system) can be used. Indeed, previous work of Boating and co-workers[26] have shown that caustic stress corrosion cracking of 304 stainless steel in 46% NaOH solution at 140° C had led to a smooth test.

Finally, it is important to note that the caustic solution of 46% NaOH refers to 46% of the pure sodium hydroxide and not to its hydrate NaOH solution.

II) To test ULTIMO 200 steel in 3.5% NaCl solution with 0.02 M K_2CrO_4 (Potassium chromate)-inhibitor.

Starchak and Kosukhina[83] have postulated that in the absence of inhibitor the hydrogen embrittlement reaction is due primary to a recombination mechanism, but in the presence of inhibitor creates an additional energy barrier to the approach of H^+ ions to the electrode surface. This reduces the activity of adsorbed hydrogen, reduces hydrogen absorption, and slows down the embrittlement reaction.

Jaberi[84] has studied the effects of anodic inhibitors on stress corrosion cracking of a 817M40-type (similar to AISI 4340) high strength steel in various aqueous environments. He concluded that the anodic adsorption inhibitors, such as potassium chromate, or sodium benzoate ($C_6H_5 \cdot COONa$), may lower the rate of stress corrosion crack growth and increase the value of K_{Iscc} for high strength steels in aqueous environments. However, Jaberi interprets them as supporting the view that SCC of high strength steels is by anodic dissolution mechanism, and not by hydrogen embrittlement.

Since Starchak and Jaberi have failed to provide any fractography evidence for their studies. Therefore, it is suggested to carry out fractography from stress corrosion tests in 3.5% NaCl solution with 0.02 M K_2CrO_4 inhibitor. The 0.02 M potassium chromate concentration is chosen because it is reported that a 0.003 M potassium chromate is indeed sufficient to provide complete inhibition of corrosion in steels in aqueous environments, and the concentration of 0.02 M is to avoid taking any risk in the test.

III) To test ULTIMO 200 steel in liquid metal (For example: Tin, Zinc, or Mercury).

Lynch[78] indicated that there is a remarkable similarity in appearance of fracture surfaces in a low-alloy steel (D6ac) after stress corrosion cracking in mercury and gaseous hydrogen environment. Lynch suggested that adsorption of liquid metal atoms is responsible for liquid-metal embrittlement, gaseous hydrogen embrittlement is predominantly due to effects of adsorption of hydrogen atoms at crack tips.

In view of this recent proposal concerning embrittlement of low alloy steel (D6ac), it would be worthwhile comparing Lynch's results with the liquid mercury embrittlement of high strength alloy steels. It is believed that a general conclusion could be made for martensitic steels, if the suggested further study is successful.

3) Uhlig and Sava[38] have postulated that proper tempering of steels may improve resistance to stress corrosion cracking. Recently, Lynch[78] has also provided some evidence that the mechanisms of hydrogen embrittlement may vary with the temperatures and time of heat treatment, but a clear understanding of the effects of heat treatments is still lacking.

Yoshino and Ikegaya[45] have studied the stress corrosion cracking in martensitic stainless steels for two different tempering conditions. It is reported that, for the single temper condition, the grain boundary appeared as a sharp edge region, thus providing a susceptible path for SCC. Connecting with the greater hydrogen solubility of retained austenite at the grain boundary, therefore, the single tempered steels are sensitive to intergranular fracture due to hydrogen embrittlement.

On the other hand, grain boundaries in the double temper condition were not as sharp as in the single temper condition. Indeed, a fine lamellar structure was observed inside the grain. This can account for the greater resistance of the double tempered steels in a corrosive environment. Moreover, the double temper treatment reduces hardness of the martensitic stainless steels, this may also improve the resistance of the steels to corrodent attack. It is also noted that the double temper treatment generally increases the volume of retained austenite in the martensitic steels. Clearly, hydrogen induced-cracking might be favourably facilitated by the greater hydrogen solubility of the retained austenite. However, in the light of laboratory investigation, Yoshino and Ikegaya[45] have pointed out that the sharp edge grain boundary of single temper condition play a more important role in the embrittlement reaction than those retained austenite particles.

Based on the above observations, it is suggested that a further investigation into the effects on the tempered martensitic steel with various tempering temperatures and times of heat treatment. The further investigation can be performed on ULTIMO 200 steel in 3.5% NaCl solution so that a general guidance document can be drafted that touches upon evaluation of temper conditions connected with environmental factors for martensitic steels. Moreover, the further study would enable more understanding to be gained of the active-path mechanism.

Indeed, the active-path mechanism was reviewed in section 1.3.2. In short, the mechanism has been applied primarily to intergranular cracking of alloys in aqueous environments, and relates the crack propagation process to the preferential dissolution of chemically active regions in the grain boundaries. The activity is associated with segregation of alloying elements or retained austenite particles to the grain boundaries. The role of mechanical stress is to keep the crack open and allow the corrodent free access to the crack tip.

4) Further refinement of the experimental apparatus and the test techniques.
For example:-

I) Use of BFS to build a SCC-monitor to detect initiation and propagation of cracks. This would enable measurements to be made of pre-crack length more accurately and to reliably determine the value of K_{Iscc}.

Richards and Deans[80] reported that there are two major advantages to monitoring initiation and propagation of stress corrosion cracks by use of BFS technique:-

a) BFS technique can be used in environmental chambers to monitor the stress corrosion cracks where optical measurement (section 2.7.2) is not possible.

b) It is known that for constant BFS there is a decrease in stress intensity with increasing crack length (see Fig. 67). The characteristics could be applied to determine the threshold stress intensity (K_{Iscc}) for the stress corrosion tests.

It is believed that K_{Iscc} value could be determined by reducing the stress intensity with varied loads on the CT specimen until no crack growth was detected by the SCC monitor.

Finally, another purpose of the further refinement of the experimental apparatus by use of BFS technique is to enable investigator to examine the kinetics of crack growth in an effort to determine whether or not the stress corrosion crack propagation is discontinuous.

c) Since in the present investigation the values of K_{Iscc} were based on 500 hours tests, therefore, it would be worthwhile extending the stress corrosion tests to 1000 hours. It is believed that the values of K_{Iscc} would be more accurate in the 1000 hours tests.

With regard to reliably determining the values of K_{Iscc},

it is necessary to fracture the CT specimen in liquid air and examine the fracture interface for any stress corrosion crack growth during tests.

II) To design a suitable vacuum chamber for fatigue pre-cracking in vacuum. Since Erasmus[85] has postulated that fatigue is influenced by the chemical environment, an indication of the influence of the fatigue pre-cracking on the subsequent stress corrosion tests could be obtained by pre-cracking in a vacuum and comparing the results with those obtained from pre-cracking in air.

It is known that a vacuum pre-crack environment would eliminate corrosion fatigue; corrosion fatigue occurs often in air pre-cracked specimens. A corrosion free pre-cracked specimen might take more time to complete the pre-cracking process. However, it would enable more understanding to be gained of the role of the moist air in the pre-cracked specimens.

5) To test ULTIMO 200 steel in hot air at a temperature of the order of 400° C.
Recommended test method: corrosion fatigue

Many recent discussions of the SCC mechanism[82, 86, 87] have pointed out that enhanced fatigue crack growth rate behaviour can be encountered at stress intensity levels well below the threshold stress intensity (K_{Iscc}) under static load conditions in the same environment.

In the light of the laboratory investigation, Shih and Clark[87] have shown that corrosion fatigue crack growth rate testing may provide the basis for a convenient, short time, accelerated corrosion test which ultimately could replaced the need for very long time stress corrosion tests in determining the values of K_{Iscc}. It is noted that the fatigue crack growth rate data were developed for an AISI 4340 steel heat treated to four yield strength levels (634 to 1289 MPa) and tested in a 446 KPa

hydrogen sulfide gas (H_2S).

Recently, Jones[88] has indicated that the oxidation fatigue in gases at high temperature has many of the same characteristics of corrosion fatigue at lower temperatures in corrosive environments. However, it is realized that Jones has failed to provide any conclusive evidence (e.g., examination of microstructure, crack paths and fractographs) of differences in mechanisms of failure in the hot gases and in the corrosive media at low temperature.

From the above reasons, therefore, it is suggested to carry out the study of corrosion fatigue crack growth of ULTIMO 200 steel in hot air (e.g., at 400° C). It is meaningful, if the fatigue crack growth rates (or fracture appearance) determined on the ULTIMO 200 steel in the hot air environment can be compared with those presented by Shih and Clark.[87] However, it is noted that, for the corrosion fatigue tests in air at 400° C, the corrosion fatigue behaviour should be markedly dependent on the waveshape or cyclic frequency, and the choice of the laboratory waveform is not, therefore, an arbitrary matter. For example, the corrosion crack may not propagate under low frequency condition because of the very slow strain rates associated with creep. On the other hand, in the cyclic loading tests at higher stressing rates it appears likely that crack growth was facilitated by conventional fatigue instead of corrosion fatigue.

Finally, apart from the cyclic loading problems, a suitable environment chamber should be designed for the fatigue crack growth rate tests in the hot air at 400° C .

REFERENCES

1. A. A. GRIFFITH: The Phenomena of Rupture and Flow in Solid, Philosophical Transactions of the Royal Society, Series A Vol.221, 1921.

2. A. H. COTTRELL: Mechanical Properties of Matter, Wiley (1964) 345.

3. G. R. IRWIN: Fracture dynamics, Fracture of Metal, ASM, 1948.

4. E. OROWAN: Fracture and Strength of Solid, Reports on Progress in Physics, Vol.12, The Physical Society, 1948-1949.

5. L. A. ERASMUS: Failure of Metals, Engineering Metallurgy, 1980.

6. G. R. IRWIN: Analysis of Stresses and Strains near the end of a Crack Transvering a Plate, J. Appl. Mech., 24, September 1957.

7. G. R. IRWIN: Fracture, Handbuch der Physik, Vol.6, Springer Verlag, 1958.

8. Annual Book of ASTM Standards, E399-81, 1984.

9. J. M. COWLING: Factors Influencing Stress Corrosion Cracking in High Strength Steels, Part II, Thesis, University of Oxford, June 1974.

10. R. ROBERTS: Fracture Mechanics, ASTM, June 1980, p.269.

11. F. H. KEATING: Symposium on Internal Stresses in Metals and Alloys, Institute of Metals, London, 1948, p.325.

12. P. GREENFIELD: Stress Corrosion Failure, 1971.

13. E. A. STEIGERWALD, F. W. SCHALLER and A. R. TROIANO: Transaction of the Metallurgical Society of AIME, Vol.215, December 1956, p.1048

14. H. H. JOHNSON, J. G. MORLET and A. R. TROIANO: Transaction of the Metallurgical Society of AIME, August 1958, p.528.

15. W. M. PARDUE, F. W. BECK, and M. G. FONTANA: Am. soc. Metals Trans. Quart., 54: p.539-548 (1961).

16. D. K. PRIEST, F. H. BECK, and M. G. FONTANA: Trans. Am. soc. Metals, 47: p473-492 (1955).

17. I. M. AUSTEN, R. BROOK and J. M. WEST: Int. Journ. of Fract., 1976, Vol.12, p.253-263.

18. W. D. ROBERTSON: Stress Corrosion Cracking and Embrittlement, 1956.

19. S. F. CLUGSTON, J. R. WEERTMAN and P. G. SHEWMON: Metallurgical Transactions A, Vol.14A, April 1983, p.695-699,

20. S. FLOREEN and J. L. NELSON: Metallurgical Transaction 14A, 1983, p.133.

21. P. G. SHEWMON: Materials Science and Technology, Vol.1, January 1985, p.2.

22. M. L. WAYMAN: Hydrogen Damage, ASM, 1979, p.214.

23. MARKUS O. SPEIDEL: Hydrogen Damage, ASM, 1979, p.329.

24 A. S. TETELMAN: Hydrogen Damage, ASM, 1979, p.178.

25. D. N. WILLIAMS: Hydrogen Damage, ASM, 1979, p.185.

26. A. BOATING: Metallurgical Transaction 14A, 1983, p.67.

27. P. C. HUGHES, I. R. LAMBORN and B. B. LIEBERT: Journal of the Iron and Steel Institute, Vol.203, May 1963, p.154.

28. M. R. LOUTHAN, Jr., G. R. CASKEY, Jr., J. A. DONOVAN and D. E. RAWL: Materials Science and Engineering, ASM, 10(1972), p.357.

29. A. PARTHASARATHI and N. W. POLAN: Metallurgical Transaction 13A, 1982, p.2027.

30. D. HULL, M. KUMOSA and J. N. PRICE: Material Science and Technology, Vol.1, March 1985, p.177.

31. H. L. LOGAN: The Stress Corrosion of Metals, 1966.

32. H. H. UHLIG: Hydrogen Damage, ASM, 1979, p.123.

33. N. BANDYOPADHYAY, J. KAMEDA and C. J. McMAHON: Metallurgical Transactions A, Vol.14A, May 1983, p.881.

34. L. A. ERASMUS: Fracture Modes in Metals, NEW ZEALAND ENGINEERING 15.8.1974, p.219-226.

35. MARS G. FONTANA and NORBERT D. GREENE: Corrosion Engineering, McGRAW-HILL Series, 1984.

36. P. W. BOYD: Stress Corrosion, 1979.

37. H. H. UHLIG: Physical Metallurgy and Stress Corrosion Fracture, AIME, June 1959, p.1-17.

38. H. H. UHLIG and J. SAVA: Transactions of American Society for Metals, Vol.56. September 1963, p.361.

39. M. B. HINTZ, L. J. NETTLETON and L. A. HELDT: SCC of Alpha-Beta Brass in Distilled Water and Sodium Sulphate Solutions, Metal. Trans. A, Vol.16A, 1985, p.971-978.

40. S. P. LYNCH: A comparative Study of Stress-Corrosion Cracking, Hydrogen-Assisted Cracking, and Liquid-Metal Embrittlement in Al, Ni, Ti and Fe-Based Alloys, Hydrogen effects in Metals, The Metall. Soc. of AIME, 1980, p.863-871.

41. D. D. MACDONALD and H. H. CHUNG, National Association of Corrosion Engineers, Vol.41, No.3, March, 1985.

42. P. C. HUGHES, I. R. LAMBORN and B. B. LIEBERT: Journal of The Iron and Steel Institute, Vol.203, July 1965, p.728.

43. D. A. MEYN: Hydrogen Damage, ASM, 1979, p.319.

44. R. N. PARKINS: Corrosion Process, 1982.

45. Y. YOSHINO and A. IKEGAYA: Pitting and Stress Cracking of 12 Cr-Ni-Mo Martensitic Stainless Steels in Chloride and Sulfide Environments; National Association of Corrosion Engineers, Vol.41, No.2, Feb. 1985.

46. ULICK R. EVANS: An Introduction to Metallic Corrosion, 1981.

47. H. D. KESSLER, R. G. SHERMAN and J. F. SULLIVAN: Hydrogen Damage, ASM, 1979, p.118.

48. KOMAI, S. KITA and K. ENDO: Bulletin of JSME, Vol.27, No.27, May 1984.

49. M. NAKAMURA and E. I. FURUBAYASHI: Metallurgical Transaction A, Vol.14A, April 1983, p.717.

50. G. SANDOZ: Metallurgical Transaction, Vol.3, 1972, p.1169.

51. L. A. ERASMUS: Hydrogen Attack on Metals (Lecture notes presented at University of Canterbury), 1973.

52. RALPH H. PETRUCCI: General Chemistry, MacMILLAN Publishing Co., Inc, New York, 1982, p.43-159 and p.497-507.

53. A. R. TROIANO: Trans. A.S.M. 52, 54 (1960).

54. B. F. BROWN, C. T. FUJII, and E. P. DAHLBERG: J. ELECTROCHEM. Soc., 1969, Vol.116, p.218-219.

55. B. F. BROWN: Cont. Belg. Etude Corros., Rapp. Tech., 1970 Vol.112 p.RT170-71.

56. J. A. SMITH, M. H. PETERSON, and B. F. BROWN: Corrosion, 1970, Vol.26, p.539.

57. R. H. JONES and W. G. WOLFER: Modelling Crack Growth Processes in Fusion Reactor Materials, J. Nucl. Mater., 122, 379-390 May 1984.

58. G. W. HONG and J. Y. LEE: The Interaction of Hydrogen with Dislocation in Iron, Acta Metall. Vol.32, No.10, p.1581-1589, 1984.

59. C. F. MUSOLFF and J. S. SMAIL: Failure of Metals, Engineering Metallurgy, 1980.

60. L. A. ERASMUS: Advanced Ferrous Metallurgy, University of Canterbury, p.171-229.

61. S. H. MARON and J. B. LANDO: Fundamentals of Physical Chemistry, MacMILLIAN Publishing Co. Inc., 1974, Chap.4. (p.146-181).

62. R. B. McLELLAN and C. G. HARKINS: Hydrogen Interactions with Metals, Materials Science and Engineering, 18 (1975), p.5-p.35.

63. H. K. BIRNBAUM: Hydrogen-Related Second-Phase Embrittlement of Solids, American Society for Metals, 1984.

64. B. J. SHAW and E. W. JOHNSON: An Evaluation of Hydrogen Embrittlement, Hydrogen Effects in Metals, The Metall. Soc. of AIME, 1980, p.691-701.

65. R. P. WEI: Rate Controlling Processes and Crack Growth Response, Hydrogen Effects in Metals, The Metall. Soc. of AIME, 1980, p.677-689.

66. G. SUNDARARAJAN and P. G. SHEWMON: The Hydrogen Attack of HSLA Steels, Metall. Trans. A, Vol.11A, 1980 p.509-516.

67. M. GAO, M. LU and R. P. WEI: Crack Paths and Hydrogen-Assisted Crack Growth Response in AISI 4340 Steel, Metall. Trans. A, Vol.15A, April 1984, p.735-746.

68. Y. HIROSE and T. MURA: Growth Mechanism of Stress Corrosion Cracking in High Strength Steel, Eng. Frac. Mechanics Vol.19, No.6, 1984.

69. S. F. CLUGSTON, J. R. WEERTMAN and P. G. SHEWMON: The Enhancement of Hydrogen Attack in Steel by prior Deformation, Met. Trans. A, Vol.14A, April 1983, p.695-699.

70. J. E. RYALL, J. F. BARRETT and L. P. DYER: The Effects of Hydrogen in Rolled Steel Products, Metal Forum, Vol.2, No.3-1979.

71. G. G. HANCOCK and H. H. JOHNSON: Trans. Met. Soc. AIME, 236, 513 (1966).

72. A. W. THOMPSON and I. M. BERNSTEIN: Microstructure and Hydrogen Embrittlement: Hydrogen Effects in Metals, The Metall. Soc. of AIME, 1980. p.291-p.308.

73 O. A. ONYEWUENYI and J. P. HIRTH: Effects of Hydrogen on Notch Ductility and Fracture in Spheroidized AISI 1090 Steel, Metallurgical Transactions A, Vol.14A, Feb. 1983. p.259-269.

74. Y. KIKUTA and ARAKI: Microscophic Redistribution Behaviour of Hydrogen and Fracture Morphology of Hydrogen-Assisted Cracking in High Strength Steel, Hydrogen Effects in Metals, The Metall. Soc. of AIME, 1980. p.309-p.317.

75. T. INOUE, K. YAMAMOTO and M. NAGUMO: Hydrogen Embrittlement of Steels with Intergranular Fracture Mode, Hydrogen Effects in Metals, The Metallurgical Society of AIME, 1980, p.777-p.784.

76. W. B. LISAGOR: Influence of Precracked Specimen Configuration and Starting Stress Intensity on The Stress Corrosion Cracking of 4340 Steel, ASTM STP821, 1984, p.80-97.

77. C. D. BEACHEM: Metallurgical Transaction, Vol.3, 1972, p.437.

78. S. P. LYNCH: Acta Metall. Vol.32, No.1, 1984, p.79-90.

79. J. K. TIEN ET AL: Metallurgical Transactions, Vol.7A, 1976, p.821.

80. C. J. BEEVERS: The Measurement of Crack Length and Shape During Fracture and Fatigue, p.28-68, 1980.

81. V. G. STARCHAK and L. D. KOSUKHINA: Cracking of Steel Due to Hydrogen Sulphide in Inhibited Media, Plenum Publishing Corporation, 1984, p.225.

82. R. N. PARKINS: A Critical Evaluation of Current Environment-Sensitive Fracture Test Methods, ASTM STP821, p.5-31, 1984.

83. V. G. STARCHAK and L. D. KOSUKHINA: Cracking of Steel Due to Hydrogen Sulfide in Inhibited Media (Translated from Zashchita Metallov, Vol.20, No.2, p.271-273, April 1984, Plenum Publishing Corporation.).

84. J. JABERI: Effects of Anodic Inhibitors on Stress Corrosion Cracking of a High Strength Steel in Aqueous Environments, Br. Corros. J., 1985, Vol.20, No.3, p.133-139.

85. L. A. ERASMUS: The Effects of Strain Ageing in Fatigue Damage in Low carbon Steel, Phd. Thesis, University of Cape Town, 1972.

86. F. P. FORD: Current Understanding of the Mechanism of Stress Corrosion and Corrosion Fatigue, ASTM STP821, p.32-49, 1984.

87. T. T. SHIH and W. G. CLARK Jr.: An Evaluation of Environment-Enhanced Fatigue Crack Growth Rate Testing as An Accelerated Static Load Corrosion Test, ASTM STP821, p.325-p.340, 1984.

88. D. A. JONES: A Unified Mechanism of Stress Corrosion and Corrosion Fatigue Cracking, Metall. Trans. A, Vol.16A, June 1985, p.1133-1141.

APPENDIX

ASTM

K_{Ic} DATA SHEET
(SAMPLE)

MATERIAL/FORM: ULTIMO 200 steel CT Specimen

HEAT TREAT: Austenitized 850°C, Oil quenched, Temp. 350°C

SPECIMEN I.D.: No. 1

SPECIMEN TYPE: CT Specimen pre-cracked in air, and tested with Instron Uni. Testing Machine. (Model: TT-K)

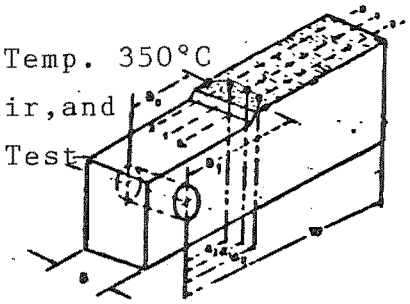

DATE: 12/2/85

DATE REPORT

Time: 1 40 pm.

PARTICULARS	DATA	REF. PARAGRAPH
● Crack Plane Orientation	Mode I	Sect. 1.2.2
● Material 0.2% Offset Yield Strength, σ_{ys}, per E8	1518N/mm^2	Sect.2.9
● Thickness, B	10 mm	Sect. 2.9.2
● Depth (Width), W	———	
for - SE(B)		
for - C(T)	20 mm	Sect.2.9.2
for - DC(T)		
○ *Arc Shaped Specimen* -		
— Width, W		
— Loading Hole Offset, X		
— Outer and Inner Radii, r_1 & r_2		

FRACTURE TEST	DATA	REF. PARAGRAPH
● *Crack Lengths* -		
— At Center of Crack Front (a_1)	11.5 mm	Sect.2.8
— At Right of Center (a_2)	11.6 "	
— At Left of Center (a_3)	11.4 "	
— At Right of Surface (a_4)	11.7 "	
— At Left Surface (a_5)	11.5 "	
— Crack Plane Symmetry $\bar{a}$	11.43 mm	Sect. 2.8
— Loading Rate	0.55 to 2.75 (MPa•m$^{\frac{1}{2}}$)/Sec.	
— Test Temperature	24°C	
— Relative Humidity		
— Load-Displacement Record		
- Spec.value of a/W	0.572	Sect. 2.9.2
- Value of f(a/W)	12.420	"

FATIGUE PRECRACKING	DATA	REF. PARAGRAPH
● $\frac{K_{max}}{E}$ <0.002in$^{\frac{1}{2}}$ (0.00032m$^{\frac{1}{2}}$)	0.0001	Sect. 2.7.1
● K_{max} <0.6 K_Q (MN/m$^{3/2}$)	22 < 34.8 (MN/m$^{3/2}$)	
● $K_{max} \leq 0.8\ K_{Ic}$		
○ *at Temperature*		
— $K_{max_{T1}} \left\{\frac{\sigma_{ys(T1)}}{\sigma_{ys(T2)}}\right\} 6\ K_Q$ (T2)		
○ *Crack Length - Starter Slot plus Fatigue*		
— a = 0.5W		
— K_{max}. ΔK	22MN/m$^{3/2}$	
— Cycles for last 2.5% of "a"		

CALCULATION OF K & R_{sx}	DATA	REF. PARAGRAPH
● P_{max}/P_Q < 1.1	1.015	
— K_Q SE(B)		
— K_Q C(T)	58 MN/m$^{3/2}$	
— K_Q A(T)		
— K_Q DC(T)		
● Valid K_{Ic}	58 MN/m$^{3/2}$	
— R_{sx}		
- a, B $\overset{?}{>}$ $2.5 \cdot (\frac{K_{IC}}{\sigma_{YS}})^2$	a=11.43 mm and B=10 mm $\gg$1.2mm.	

ASTM

K_{Ic} DATA SHEET (SAMPLE)

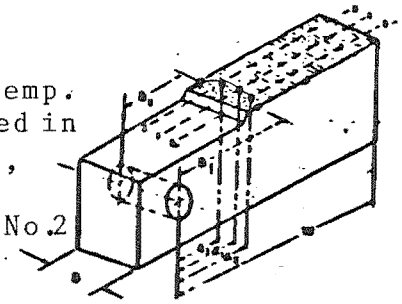

MATERIAL/FORM ULTIMO 200 steel CT Specimen

SPECIMEN I.D. No.13

HEAT TREAT Austenitized 850°C, Oil quenched, Temp. 350°C.

SPECIMEN TYPE CT Specimen pre-cracked in air with 0.5 KN dynamic load, and tested with the stress corrosion experimental rig No.2

DATE 19/5/85

DATE REPORT

Time to failure: 1338 mins(=22.3 hrs).

PARTICULARS	DATA	REF. PARAGRAPH
● Crack Plane Orientation	Mode I	Sect. 1.2.2
● Material 0.2% Offset Yield Strength, σ_{ys}, per E8	1518 N/mm^2	Sect. 2.9
● Thickness, B	10 mm	Sect. 2.9.2
● Depth (Width), W	———	
for - SE(B)		
for - C(T)	20 mm	Sect. 2.9.2
for - DC(T)		
○ *Arc Shaped Specimen* -		
— Width, W		
— Loading Hole Offset, X		
— Outer and Inner Radii, r_1 & r_2		

FRACTURE TEST	DATA	REF. PARAGRAPH
● *Crack Lengths* -		
— At Center of Crack Front (a_1)	10.80 mm	Sect. 2.8
— At Right of Center (a_2)	10.90 mm	"
— At Left of Center (a_3)	10.80 mm	"
— At Right of Surface (a_4)	11.15 mm	"
— At Left Surface (a_5)	11.16 mm	"
— Crack Plane Symmetry $\bar{a}$	10.83 mm	Sect. 2.8
— Load (P_{act})	1067.5 N	
— Test Temperature	24°C	
— Relative Humidity		
— Load-Displacement Record		
- Spec.value of a/W	0.5415	Sect. 2.9.2
- Value of Y[=f(a/W)]	10.88	Sect. 2.9.2

FATIGUE PRECRACKING	DATA	REF. PARAGRAPH
● $\frac{K_{max}}{E}$ <0.002in$^{1/2}$ (0.00032m$^{1/2}$)	0.00002	Sect. 2.7.1
● K_{max} <0.6 K_Q		
● K_{max} ≤0.8 K_{Ic}		
○ *at Temperature* — $K_{max_{T1}}\left[\frac{\sigma_{ys(T1)}}{\sigma_{ys(T2)}}\right]$ ≤6 K_Q (T2)		
○ *Crack Length - Starter Slot plus Fatigue*		
— a = 0.5W		
— K_{max}, ΔK	4 MN/m$^{3/2}$	Sect. 2.7.1
— Cycles for last 2.5% of "a"		

CALCULATION OF K & R_{sx}	DATA	REF. PARAGRAPH
● P_{max}/P_Q < 1.1		
— K_Q SE(B)		
— K_Q C(T)		
— K_Q A(T)		
— K_Q DC(T)		
● Valid K_{Iscc}	8.3 MN/m$^{3/2}$	Sect.2.9.2
— R_{sx}		